Searching for Ultra-high Energy Neutrinos with Data from a Prototype Station of the Askaryan Radio Array

DISSERTATION

Presented in Partial Fulfillment of the Requirements for
the Degree Doctor of Philosophy in the
Graduate School of The Ohio State University

By

Eugene S. Hong,
Graduate Program in Physics
The Ohio State University

2014

Dissertation Committee:

Prof. Amy L. Connolly, Adviser
Prof. John F. Beacom
Prof. Christopher S. Hill
Prof. Brian Winer

Abstract

The observed GZK cutoff in the cosmic ray spectrum has led to a strongly motivated expectation of an ultra-high energy (UHE) neutrino flux arising from the interactions between the highest energy cosmic rays and cosmic microwave background photons. Aside from these diffuse neutrinos, UHE neutrinos are also expected to be produced in the same astrophysics sources producing the UHE cosmic rays such as Gamma-Ray Bursts (GRB) and AGNs. Here, we discuss two UHE neutrino searches using data from the Askaryan Radio Array (ARA) prototype Testbed station: one search for a diffuse neutrino flux and another for neutrinos from GRBs. Testbed data from 2011 to 2012 are used for the searches in the thesis. We discuss how we define the analysis cuts, optimize the analysis cut parameters for maximum sensitivity to UHE neutrinos, estimate the number of background and neutrino events, and set neutrino flux constraints in the UHE region ($> 10^{17}$ eV). We use an optimistic flux model from Kotera *et. al.* 2010 as our baseline model and optimize our analysis cuts for this model. The GRB neutrino search follows the same analysis technique as the diffuse neutrino flux search with some modifications. A timing constraint for each GRB reduces the estimated background dramatically and therefore we can loosen some of our analysis cuts for the GRB neutrino search. We also present detailed descriptions about tools that are used for the searches such as AraSim, a Monte-Carlo simulation that we developed, and RaySolver, a code to carry out ray tracing in ice with a depth-dependent index of refraction model. We present constraints on the neutrino flux from the ARA Testbed for diffuse neutrinos and GRB neutrinos separately. These neutrino flux constraints and analysis techniques from the Testbed will provide a benchmark for the future deep ARA stations' analyses which are expected to improve neutrino flux constraints by a factor of three or more due to differences in the design of the stations.

To my parents

ACKNOWLEDGMENTS

I would like to thank my advisor Amy Connolly for helping and supporting me for all the work I have done during my Ph.D. It would be impossible for me to finish all the projects and researches without her support. It was my pleasure and honor to work as her research group and also as a part of Askaryan Radio Array (ARA) experiment.

I appreciate other group members: Carl Pfendner, Patrick Allison who gave me a wonderful experience to work with, especially for Carl Pfendner who helped me a lot in both research and personal life manners. His thoughtful and patience conversations helped and supported my difficult times.

I thank my committee members: John Beacom, James Beatty, Christopher Hill and Brian Winer. Their sincere advices helped me what I have to think about and decide for my future plans.

I also want to thank my friends Paul Shellin, Kenji Oman and Ranjan Laha who shared many hours with me and gave me an enjoyable life in OSU.

Many thanks to ARA collaborators: David Seckel, David Besson, Ming-Yuan Lu and all others.

Finally I would like to thank my family, my parents and my brother. Without their encouragements and supports, I would not be able to finish my Ph.D.

And also the one whom made my life changed forever...

VITA

2006 . . . . .B.Sc., Korea University, S. Korea

2009 . . . . .M.S., Korea University, S. Korea

PUBLICATIONS

Improved Performance of the Preamplifier-Shaper Design for a High-Density Sensor Readout System, Eugene S. Hong, Eunil Won and Jaehyeok Yoo, Journal of the Korean Physical Society, 54, 760 (2009) [1]

First Constraints on the Ultra-High Energy Neutrino Flux from a Prototype Station of the Askaryan Radio Array, Patrick Allison, *et. al.* [arXiv:1404.5285] [2]

FIELDS OF STUDY

Major Field: Physics

Studies in Experimental Astroparticle Physics: Ultra-High Energy Neutrinos

Contents

Page

Chapters:

List of Tables

Table **Page**

List of Figures

Figure **Page**

Chapter 1

Introduction

Neutrinos are exceptional messenger particles due to their unique properties such as their neutral charge and low cross sections. The first property, the neutral charge, makes it possible for neutrinos, once produced at the source, to travel directly towards the Earth without any influence from magnetic fields. Once we reconstruct the direction of the neutrino, we can learn about the distribution of the source which corresponds to the direction of the neutrino. Neutrinos are one of the few particles that can provide direct information about astrophysical phenomena. The second property, the low cross section, comes from the fact that neutrinos can only interact through the weak force. In other words, they don't interact with other particles with high probability and therefore neutrinos can travel cosmological distances without being attenuated. The cross section of neutrinos in matter is approximately 10^{-32} cm^2 at 10^9 GeV [15]. It is also possible for neutrinos to be produced inside of the source and penetrate out of the source (at 10^9 GeV, the neutrino mean free path in water is $\sim 10^6$ m, [5]) and thus provide us the information about the interior of the source. This direct measurement of the inner activities of a source is only possible through neutrinos.

These unique properties of neutrinos have made them a fascinating topic of research in particle astrophysics. Searching for the source of ultra-high energy (UHE,

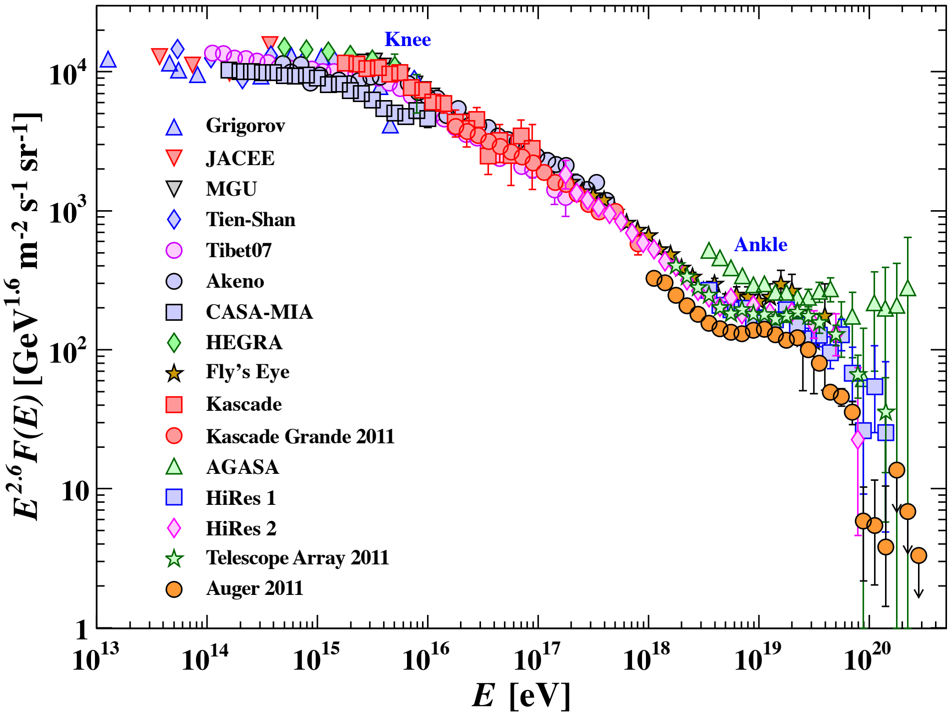

Figure 1.1: Cosmic ray flux in broad energy range. AGASA [4] didn't measured the cutoff at GZK threshold energy. Image from [5].

$> 10^{18}$ eV) cosmic rays (CRs) is one of the most interesting research topics which can be achieved by neutrino experiment. Cosmic rays in the UHE region have been observed by multiple experiments, shown in Fig. 1.1, [16], [17], [18]. However, the source of these exceptionally high energy particles is unknown. UHE neutrinos are expected to be produced along with ultra high energy cosmic rays (UHECRs) at the source and therefore we expect to learn about the geometrical location and the internal physics of the sources by detecting UHE neutrinos. Another reason which motivates us to study this UHE region is that, the center of mass of a neutrino interaction in our detectors is higher than that of the most energetic human-made particle collisions

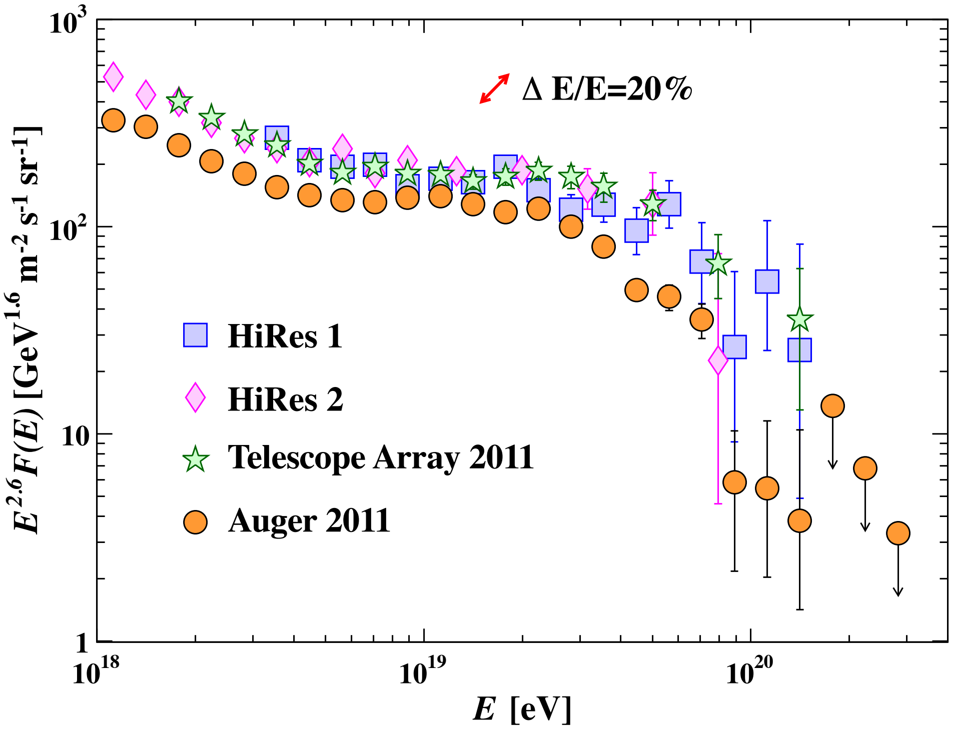

Figure 1.2: Cosmic ray flux in the UHE region. Auger and HiRes data which detected the cosmic ray flux cutoff above $10^{19.5}$ eV are shown. Image from [5].

(Large Hadron Collider, ~ 10 TeV) and therefore this study can extend the scope of particle physics to higher energies [19,20].

1.1 Ultra-High Energy Neutrino Source Candidates

There are many UHE neutrino source candidates such as GZK interactions [21, 22], Gamma-Ray Bursts (GRBs) and Active Galactic nuclei (AGNs). In the 1960's, Greisen, Zatsepin and Kuzmin predicted UHECRs, with energies above a threshold of 5×10^{19} eV, would undergo π photo-production through their interactions with cosmic microwave background photons (CMB) and this is known as GZK effect [21–23]. Fly's Eye [16], HiRes [17] and Auger [18], have confirmed the phenomenon of a break in the cosmic ray flux above the GZK threshold energy consistent with the GZK process (Fig. 1.1). Fig. 1.2 shows the measured UHECR flux from the Auger, and HiRes experiments. However, it is still possible that cosmic ray sources themselves have injected UHECRs with a cutoff at the GZK threshold energy [24]. Detection of UHE neutrinos can confirm that the GZK effect is the cause of the cutoff in the UHECR flux above 10^{19} eV. Further details about the GZK effect will be discussed in the next section.

GRBs are one of the point source candidates that are expected to produce neutrinos up to 10^{19} eV. GRBs were first discovered in late 1960s by the Vela satellite network. When a GRB explodes, it is the brightest γ-ray source in the sky. Though the mechanism of GRBs is not well known, measured properties of GRBs such as energetic ($> 10^{50}$ ergs) in a short period of time (typically < 1 min) are extreme enough to consider GRBs as a candidate of UHE neutrinos. Currently, the most generally accepted model for GRBs is the fireball shock model [25,26]. In the fireball model, protons are expected to be accelerated by shock accelerations in internal shocks. This prompt emission process can produce neutrinos by $p\gamma$ interactions. There is also afterglow emission which caused by the interaction between the expanded shock and external matter such as interstellar medium. The afterglow emission is expected to produce neutrinos from $p\gamma$ interactions. More explanations about GRBs are presented in Section 2.2.

AGNs are another strong candidate of UHE neutrino source. AGNs consist of an accretion disk and relativistic jets in the standard model. When there is a super massive black hole (10^6 to 10^{10} times the mass of the Sun) at the centre of the galaxy, surrounding materials dissipate toward the black hole and forms a disk like shape which is called accretion disk. Some accretion disks produces jets which are narrowly collimating toward the opposite directions from close to the disk. Similar to the jets in GRBs, shocks in the jet are expected to produce UHECRs, UHE neutrinos and high energy γ-rays via the shock accelerations.

The searches on two types of neutrino source, diffuse neutrinos (GZK neutrinos) and point source neutrinos (GRB neutrinos), will be presented separately in different chapters in this paper.

1.2 Detecting Techniques and Experiments

There are two major detection techniques for UHE neutrinos, optical and radio electromagnetic Cherenkov radiation techniques. Cherenkov radiation is produced when charged particles move faster than the speed of light in the medium. In order to detect Cherenkov radiation, the medium should be a dielectric which is transparent to electromagnetic waves. The optical Cherenkov technique uses optical light that is radiated from individual charged particles in the cascade. On the other hand, the Radio Cherenkov technique (also called the Askaryan effect) uses the coherent radio signal from the charge asymmetry of entire cascade. Therefore we can say that the visible Cherenkov signal is a microscopic aspect of the cascade, while radio Cherenkov signal is a macroscopic aspect of the cascade. Super Kamiokande [27], Astronomy with a Neutrino Telescope and Abyss environmental RESearch (ANTARES) [28], and IceCube [29] are the experiments which use optical Cherenkov technique. On the other hand, Antarctic Impulse Transient Antenna (ANITA) [8], Antarctic Ross Iceshelf Antenna Neutrino Array (ARIANNA) [30], and Askaryan Radio Array (ARA) [31] use radio Cherenkov technique. More detailed descriptions about the detection techniques are shown in Section 3.1.

UHE neutrino experiments are mostly located at extreme places such as Antarctica in order to overcome some difficulties of detecting the particles. Along with their low interaction cross section in matter ($\sim 10^{-32}$ cm^2 at 10^9 GeV, [15]), their low flux on Earth ($<\sim$ 10 km^{-2}yr^{-1}) make it difficult to for us to detect them in ordinary laboratory environments. We need a place which can provide us a detection material with a volume of the order of 100 km^3 and relatively background free environment. The large volume of nearly pure ice in Antarctica is an ideal detector for UHE neutrinos because of the long attenuation length of the medium. Attenuation length for radio waves in Antarctic ice is approximately 500 m [32] while the optical light is approximately 50 m [33]. It is difficult to build a human-made detector with such a large volume. It is also possible to trace anthropogenic background sources in Antarctica as they come from relatively few isolated locations. In present models for UHE neutrinos, even with 100 km^3 volume of instrumented ice, we can detect approximately 10 events in a year [31]. So, new experiments aim for detector to reach the exposure on the order of 100 km$^3 \cdot$ yr in order to detect UHE neutrinos robustly.

The ARA is a next-generation radio Cherenkov neutrino detector deployed in the ice at the South Pole. The ARA aims to deploy 37 stations of antennas at 200 m depth spanning 100 km^2 of ice. To date, one prototype Testbed station and three full stations have been deployed. In 2010-2011 drilling season, the Testbed station was deployed at a depth of $\sim$ 30 m. Full stations A1 at 100 m depth, and A2 and A3 at 200 m depth are deployed in 2011-2012 and 2012-2013 season, respectively. More information about the ARA is shown in Chapter 4.

This dissertation presents the first neutrino flux constraint from the ARA Testbed. The techniques that are used to optimize the sensitivity of ARA Testbed will be used as a basis for analyses of the future ARA deep stations or other radio array experiments in Antarctica.

This paper is organized as follows. In Chapter 2, we discuss different sources of UHE neutrinos. In Chapter 3, past and present experiments designed to detect UHE neutrinos will be discussed. Then in Chapter 4, we introduce the Askaryan Radio Array (ARA) and its prototype Testbed station, the instrument which we used to carry out our UHE neutrino searches. In Chapter 5, we describe the simulation tools we developed for the neutrino searches. In Chapter 6 and 7, a diffuse and GRB neutrino searches are presented, respectively. In Chapter 8, we discuss our conclusions.

Chapter 2

Motivations for Ultra High Energy Neutrinos

UHE neutrinos can originate from the GZK interactions or astrophysical sources such as Gamma-Ray Bursts (GRBs) and Active Galactic Nuclei (AGNs). In this chapter, we discuss the different candidates for sources of UHE neutrinos. The GZK effect, which is expected to be a dominant source of UHE neutrinos, is discussed first with a detailed explanation about the interaction between proton and CMB photon. The GRB as a UHE neutrino source is then discussed. Lastly, other candidate models for UHE neutrinos are shown.

2.1 GZK effect

We discuss the GZK process and associated decay chains. When a UHE proton is injected above the threshold energy of 5×10^{19} eV for the GZK effect, the following processes are possible.

$$\begin{aligned} p + \gamma_{\text{CMB}} \rightarrow \quad & \pi^+ \quad + n \\ & \qquad\quad n \rightarrow p + e^- + \bar{\nu}_e \\ & \pi^+ \quad \rightarrow \mu^+ + \nu_\mu \\ & \qquad\quad \mu^+ \rightarrow e^+ + \nu_e + \bar{\nu}_\mu \end{aligned} \tag{2.1}$$

$$\begin{aligned} p + \gamma_{\mathrm{CMB}} \rightarrow \quad & \pi^0 \quad +p \\ & \pi^0 \quad \rightarrow \gamma + \gamma \end{aligned} \tag{2.2}$$

In the first process (Eq. 2.1), we can assume that daughters of the π^+ (e^+, ν_μ, $\bar{\nu}_\mu$, and ν_e) get approximately 1/4 of π^+ energy.

The threshold energy for π photo-production can be calculated from the Mandelstam variable s:

$$s \;=\; (P_p + P_{\mathrm{CMB}})^2_{\mathrm{lab}} = (P_{\pi^+} + P_n)^2_{\mathrm{CM}} \tag{2.3}$$

$$\;=\; m_p^2 + 2\cdot E_p E_{\mathrm{CMB}}(1 - cos\theta) = (m_\pi + m_n)^2 \sim (1.1\mathrm{GeV})^2 \tag{2.4}$$

$$\therefore\; E_{p,\mathrm{thres}}^{\mathrm{GZK}} \sim \frac{m_\pi^2 + 2\cdot m_\pi m_p}{4\cdot E_{\mathrm{CMB}}} \sim 5 \times 10^{19}\,\mathrm{eV} \tag{2.5}$$

where P_x is a four momentum of particle x, and $E_{\mathrm{CMB}} \sim 3\cdot k_B \cdot T \sim 3\times10^{-4}\,\mathrm{eV/K}\cdot 3\,\mathrm{K} \sim 10^{-3}\,\mathrm{eV}$. It is assumed that initial proton is relativistic and hence $E_p \sim P_p$ is used. The threshold energy is calculated when the initial proton and the CMB photon in the lab frame are colliding with opposite momenta ($\theta = -\pi$) and the final state particles (π^+ and n) are at rest in the center of momentum frame (CM). As both processes (Eq. 2.1 and Eq. 2.2) have approximately the same invariant mass, their threshold energies are same. Also the total energy of the final state particles in the center of momentum frame is $\sqrt{s} \sim 1.1$ GeV (Eq. 2.4) which is approximately the rest mass of the Δ^+ particle. Therefore the Δ^+ resonance is a dominant channel and boosts the cross section of the interaction near the threshold energies (see the Fig. 2.1).

For the second π photo-production process (Eq. 2.2), when a π^0 is created, it will decay to two photons. These photons will each carry approximately half of the π^0 energy. However, these UHE photons are attenuated due to two dominant energy loss processes while they travel to Earth. These energy loss processes are pair production

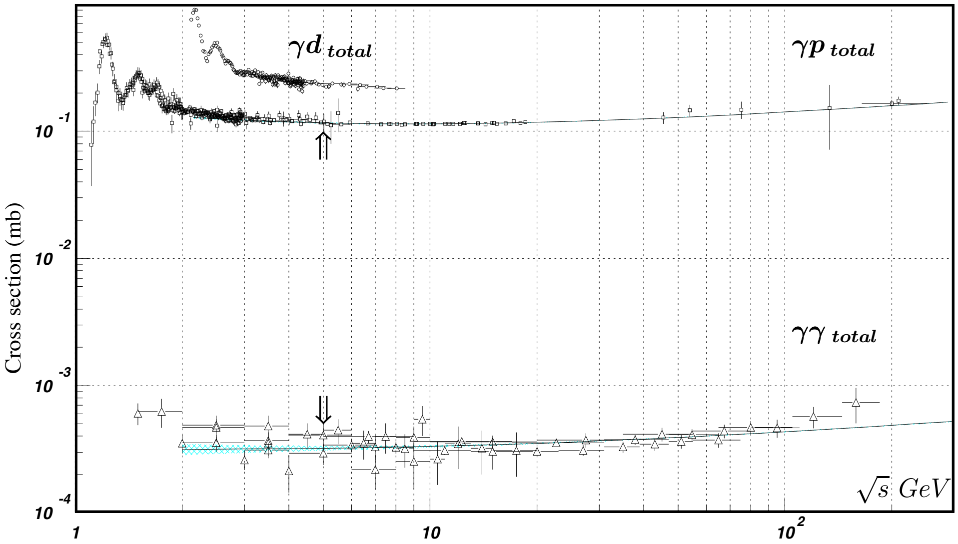

Figure 2.1: Total hadronic cross sections for γd, γp, and $\gamma\gamma$ interaction. The cross section for the GZK interaction is the γp cross section in the plot, which has the peak at $\sqrt{s} \sim 1.1$ GeV due to the Δ^+ resonance. Image from [5].

with the CMB and pair production with optical light background ($\gamma + \gamma_{\rm bgr} \to e^+ + e^-$) followed by inverse Compton scattering ($e^\pm + \gamma_{\rm bgr} \to \gamma + e^\pm$). The threshold energy for pair production with the CMB is

$$\begin{aligned} s &= (P_\gamma + P_{\rm CMB})^2_{\rm lab} = (P_{e^+} + P_{e^-})^2_{\rm CM} \qquad (2.6)\\ &= 2\cdot E_\gamma E_{\rm CMB}(1 - cos\theta) = (2\cdot m_e)^2 \\ \therefore\ & E^{\rm CMB}_{\gamma,\rm thres} \sim \frac{m_e^2}{E_{\rm CMB}} \sim 3\times 10^{14}\,{\rm eV} \qquad (2.7)\end{aligned}$$

and, with optical light, it is

$$\begin{aligned} s &= (P_\gamma + P_{\rm opt})^2_{\rm lab} = (P_{e^+} + P_{e^-})^2_{\rm CM} \qquad (2.8) \\ &= 2\cdot E_\gamma E_{\rm opt}(1 - cos\theta) = (2\cdot m_e)^2 \\ \therefore\ & E^{\rm opt}_{\gamma,\rm thres} \sim \frac{m_e^2}{E_{\rm opt}} \sim 3\times 10^{11}\,\mathrm{eV}. \qquad (2.9) \end{aligned}$$

where final state electrons and positrons are at rest in center of momentum frame. Energy of optical light background is taken to be $E_{opt} = h\nu \sim 1$ eV.

When photons have energies above the threshold $E^{\rm CMB}_{\gamma,\rm thres}$ in Eq. 2.7, pair production with the CMB is the dominant energy loss process as the number density of target CMB photons is approximately four orders of magnitude larger than the optical light background ($n_{\rm CMB} \sim 10^2$ cm^{-3}, while $n_{\rm opt} \sim 10^{-2}$ cm^{-3} [34]). Once the energy of a photon drops below $E^{\rm CMB}_{\gamma,\rm thres}$, pair production with optical light becomes its dominant energy loss process. Using the results above, we can estimate that the diffuse gamma ray background flux from the GZK effect will have a pile up just below the threshold for further pair production, $E^{\rm opt}_{\gamma,\rm thres}$. With both the cascade diffuse gamma ray background flux and UHE proton flux discussed above, we can derive a strong constraint on the expected neutrino flux [3]. This is discussed further in Section 2.1.2.

We can also calculate the distance over which π photo-production becomes important for UHECRs. The probability to interact is $P = 1 - e^{-n\sigma L}$ where n is number density of target (here, the CMB), σ is the proton-photon cross section, and L is the total travel distance of proton. From the Fig 2.1 [5], at $\sqrt{s} \sim 1.1$ GeV (at the threshold energy of the GZK interaction), the cross section $\sigma_{p\gamma}$ is approximately 6×10^{-28} cm^2, and the target number density $n_{\rm CMB}$ is approximately 4×10^2 cm^{-3}.

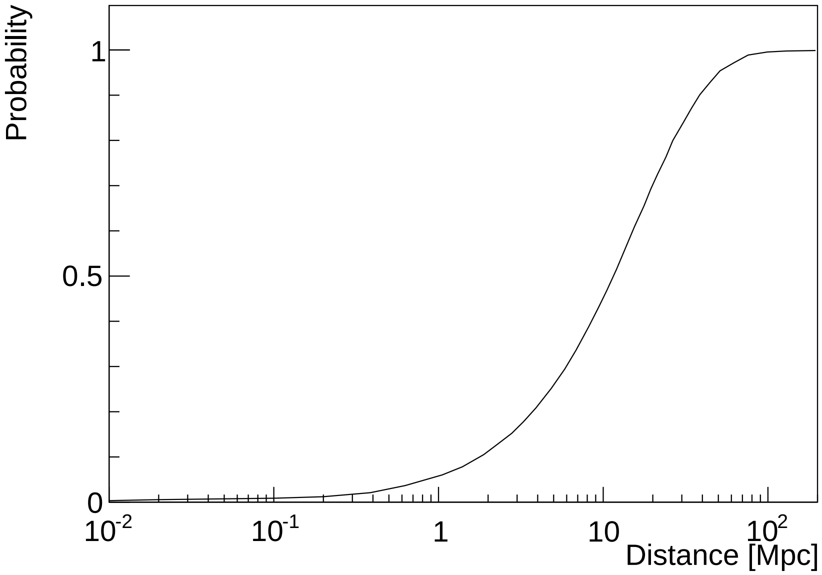

Figure 2.2: Probability for π photo-production by a CR as a function of the distance of the source at Δ^+ resonance.

Therefore,

$$\begin{aligned} P(L) &= (1 - e^{-n_{\mathrm{CMB}}\sigma_{p\gamma}L}) \\ &\sim (1 - e^{-4\times10^2\times6\times10^{-28}\times L}). \end{aligned} \tag{2.10}$$

Fig. 2.2 shows the probability as a function of distance (at resonance). Above 20 Mpc, π photo-production becomes important as the probability is bigger than 80%. So, the proton is almost guaranteed to undergo π photo-production when sources of UHE protons are beyond 20 Mpc from Earth. When the energy of the proton increases, the distance at which the π photo-production process becomes important increases since the proton-photon cross section goes off resonance [5] and the average interaction length of π photo-production process becomes $\sim$ 50 Mpc [35].

The Bethe-Heitler (BH) pair production process ($p + \gamma_{CMB} \rightarrow p + e^+ + e^-$) is another possible interaction between UHE protons and the CMB. Above the GZK threshold energy, compared with the π photo-production process, BH pair production has a smaller cross section as it does not have a resonance. BH pair production has a smaller proton threshold energy ($E^{\mathrm{BH}}_{p,\mathrm{thres}} \sim 5 \times 10^{17}$ eV) than π photo-production, and so it will be a dominant energy loss process between $E^{\mathrm{BH}}_{p,\mathrm{thres}}$ and $E^{\mathrm{GZK}}_{p,\mathrm{thres}}$.

2.1.1 Models for GZK induced neutrino

In this section, we discuss the basic prescription for estimating the flux for neutrinos from GZK interactions, and models based on UHECR and gamma ray constraints.

Using minimal assumptions and some basic concepts, we can calculate the flux of cosmic rays, or any particles from the GZK process, by the general equations [36–38],

$$J_b(E) \equiv \frac{dN_b}{dE\,dA\,dt\,d\Omega} = \int_0^\infty dE_i G_b(E, E_i) \cdot I(E_i, t), \tag{2.11}$$

where

$$G_b(E, E_i) = \frac{1}{4\pi} \int_0^\infty dr \left| \frac{\partial P_b(E; E_i, r)}{\partial E} \right| \rho_0 [1 + z(r)]^n \Theta(z - z_{min}) \cdot \Theta(z_{max} - z), \tag{2.12}$$

$$I(E_i, t) = \frac{d^2 N_p}{dE_i\,dt}. \tag{2.13}$$

In Eq. 2.12, $P_b(E; E_i, r)$ is the probability of a particle b (b can be either p, ν_e, or ν_μ) being detected on Earth with energy E when a proton was initially injected with energy E_i at a distance r away. $I(E_i, t)$ is the injection spectrum of the source, where proton-only injection is assumed. N_b is the number of b particles detected and A, t, and Ω are area, time, and solid angle respectively. The constant ρ_0 is the co-moving number density of the source of particles, z is the redshift, and n is a redshift evolution factor related to the evolution of source densities in redshift. The limits of the integral in Eq. 2.12 are z_{min} and z_{max}. Using calculated probabilities from [39], we can let $z_{min} = 0$ and $z_{max} = 2$ and calculate the distance at a given redshift with

$$dz = (1 + z)H(z)dr \tag{2.14}$$

where $H(z)$ is the Hubble parameter $H^2(z) = H_0^2[\Omega_M(1+z)^3 + \Omega_\Lambda]$. H_0 is the Hubble constant at present, 70 km/s/Mpc, and the ratio of matter and critical density of the universe (in other words, matter density for flat universe) $\Omega_M = 0.3$ and ratio of vacuum energy and critical density of universe $\Omega_\Lambda = 0.7$ [5].

Eq. 2.13 describes the injection spectrum for the source. We adopt a basic power-law injection spectrum with an upper limit on the energy, $E_{\max}$,

$$I(E_i, t) = I_0 \cdot E_i^{\alpha} \cdot \Theta(E_{\max} - E_i). \tag{2.15}$$

The authors of [40, 41] provide the values for the probabilities $P_b(E; E_i, r)$ for $b = p$, ν_e, and ν_μ at [39]. When the probability was calculated by Fodor *et al.* [40,41], some methods were used to simplify the calculation. To calculate the probabilities, first, they used the SOPHIA Monte Carlo simulation for π photo-production. They assumed that the initially injected particle from the source is a proton and sources were assumed to be isotropically distributed. They also assumed that the Bethe-Heitler pair production process ($p + \gamma_{CMB} \rightarrow p + e^+ + e^-$) is the dominant energy loss process other than π photo-production, and used a continuous energy loss approximation for the energy loss process. Also, they neglected synchrotron radiation caused by extragalactic magnetic fields, assuming these fields are smaller than 10^{-9} G. With these assumptions, they calculated the probability P_b for detecting particle b on Earth using infinitesimal steps in distance (0.1 kpc) from redshift $z = 0$ to $z = 2$.

So, using these tools, we can only calculate the flux due to sources to a redshift of $z = 2$. Redshift of $z = 2$ is approximately 3 Gpc, which can cover near the size of the entire universe ($\sim$ 10 Gpc).

There are two unknown factors in Eq. 2.12 and 2.15. ρ_0 and I_0, the co-moving source density and injection spectrum factors. If we assume that the detected UHECRs in Auger [18] are entirely protons, we can use the expected proton flux with Eq. 2.11 and estimate the product of $\rho_0 \cdot I_0$ by fitting the flux spectrum. We used a proton flux with parameters $n = 3$ and $\alpha = -2.6$, which are typical values as $n \sim 3$ accounts for typical star formation rate (SFR) up to $z = 1$ [42] and $\alpha = -2.6$ is the estimated injection spectrum for UHECRs below the GZK threshold energy [5]. Fig. 2.3 shows the fit result of the Auger UHECR data (stars) compared with a model with $n = 3$, $\alpha = -2.6$, $z_{\text{min}} = 0.012$, $E_{\text{min}} = 10^{16}$ eV, and $E_{\text{max}} = 3 \times 10^{21}$ eV. Using the fit values from Fig. 2.3, we can calculated the GZK UHE neutrino flux with different models. In Fig. 2.4, we show the estimated GZK UHE neutrino flux from different models. All three models used the same $\alpha = -2.6$, $z_{\text{min}} = 0.012$, $E_{\text{min}} = 10^{16}$ eV, and $E_{\text{max}} = 3 \times 10^{21}$ eV conditions. WB model is discussed in section 2.3.

2.1.2 Models for GZK induced neutrino with UHECR and EGRB constraints

In the previous section, Auger cosmic ray data is used to find the normalization factor to estimate the GZK induced neutrino flux. It is possible to use gamma ray data along with cosmic ray data to get more strict estimates for the neutrino flux from GZK interactions. Using Fermi-LATs' extragalactic gamma ray background (EGRB) data and HiRes' UHECR data, M. Ahlers *et al.* calculated constraints on GZK induced neutrino flux models [3]. In order to do this, they first used similar assumptions as in section 2.1.1 to model UHECRs, GZK induced neutrinos, and the

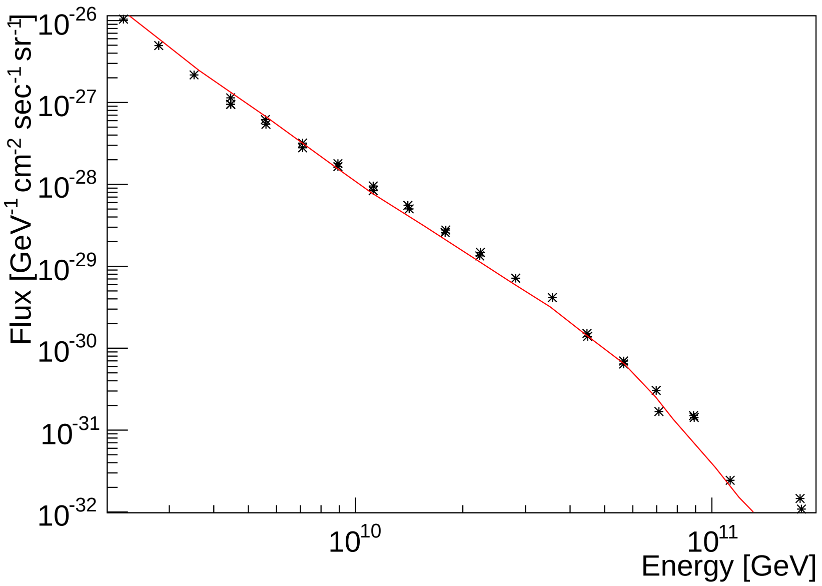

Figure 2.3: Plotting Auger UHECR data against a model for the CR flux at Earth with $n = 3$ and $\alpha = -2.6$. Auger data is shown as stars and the model is shown as red solid line.

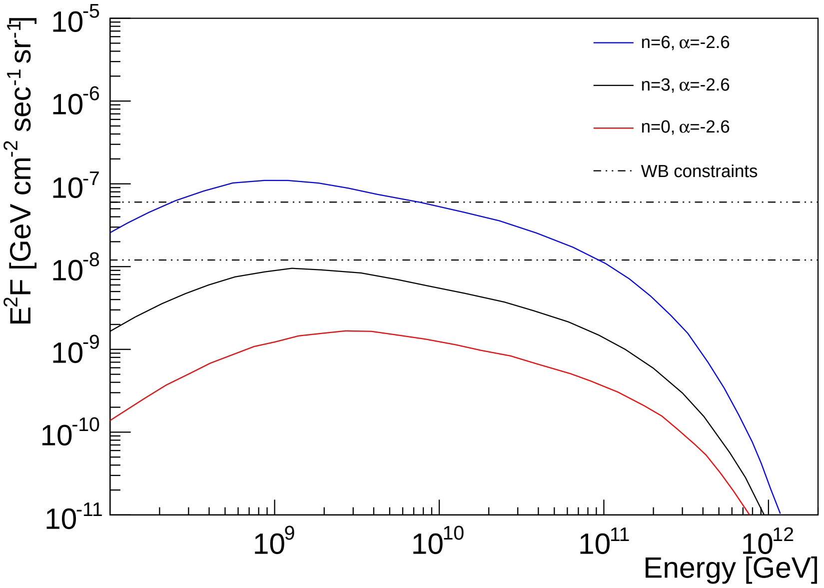

Figure 2.4: Intensity of GZK induced neutrino models based on Auger UHECR data. Waxman-Bahcall constraint is shown as dash-dotted line.

E_{min}	$10^{17.5}$ eV	10^{18} eV	$10^{18.5}$ eV	10^{19} eV
n	3.50	3.20	4.05	4.60
α	-2.49	-2.52	-2.47	-2.50

Table 2.1: Best fit parameters for HiRes UHECR data and Fermi-LAT EGRB data from [3]. The fit results are shown with the data points in Fig. 2.5.

diffuse γ-ray background. They assumed that the UHECRs are only protons. They used a continuous energy loss model for Bethe-Heitler pair production. Unlike in section 2.1.1, they included cascade processes for the diffuse gamma ray background, such as an inverse Compton scattering, $e^{\pm} + \gamma_{bgr} \rightarrow e^{\pm} + \gamma$, and pair production, $\gamma + \gamma_{bgr} \rightarrow e^{+} + e^{-}$. They fitted the simulation result with both Fermi-LAT's EGRB data and HiRes' UHECR data. In Fig. 2.5, the best fit model for the Fermi-LAT EGRB and HiRes's UHECR data from $E_{\text{min}} = 10^{17.5}$ eV is shown as an example. The maximal cascade line in Fig. 2.5 is obtained through two steps. First, they made models which meet the lower uncertainty bound on the highest energy data point of Fermi-LAT. These models are shown in Table 2.1. Second, they found the maximum value of $E^2 J$ for the given model. Fig. 2.6 shows the predicted neutrino fluxes and constraints on total diffuse neutrino flux from AMANDA [43, 44], Auger [18], Baikal [45], HiRes [46], ANITA [8], and IceCube [47, 48]. The IceCube limit is shown for 5 σ sensitivity after 1 year of observation. It is notable that, without using Fermi-LAT data, they calculated a flux limit approximately an order of magnitude weaker (thin dotted line in Fig. 2.6) than using Fermi-LAT data for fitting the EGRB flux (solid : best fit, dashed : 99% C.L. range in Fig. 2.6). This means, with Fermi-LAT data, they can get a more stringent neutrino flux limit than without by approximately an order of magnitude.

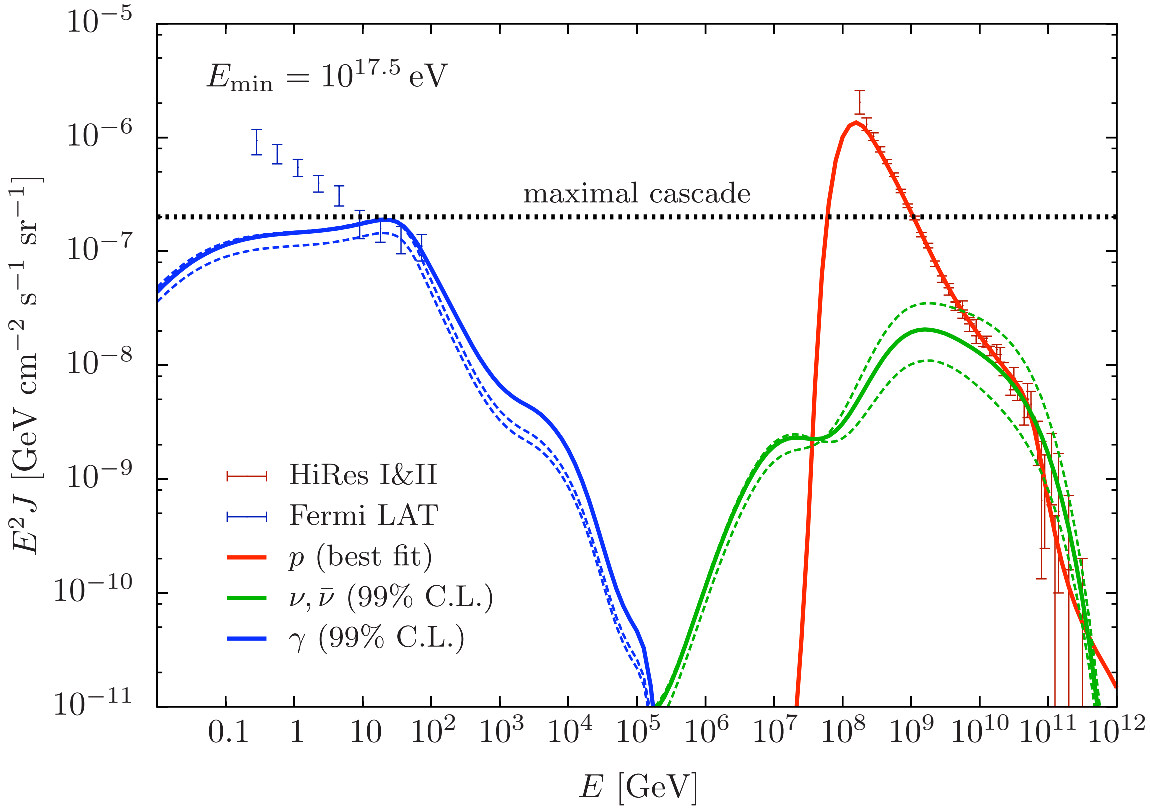

Figure 2.5: GZK induced neutrino flux (green solid line : best fit model shown in Table 2.1, green dashed line : 99% C.L. of best fit) from $E_{\min} = 10^{17.5}$ eV model shown with UHECR data from HiRes and EGRB data from Fermi-LAT. Image from [3].

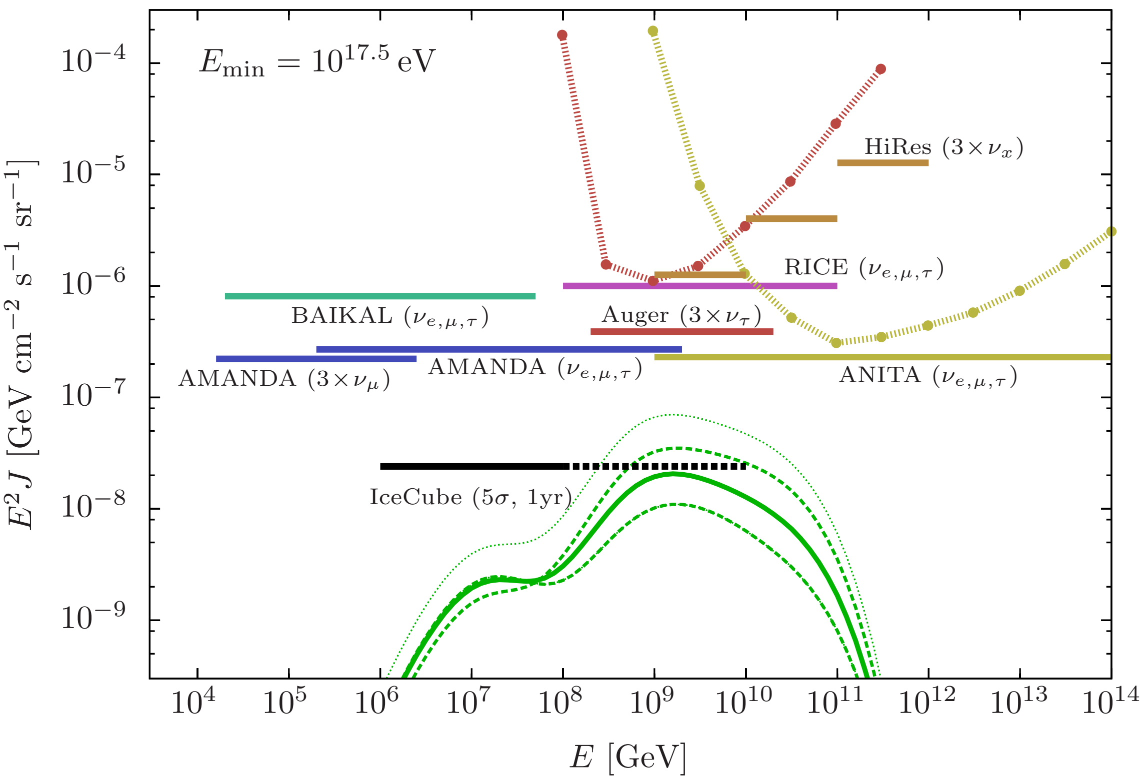

Figure 2.6: Expected GZK induced neutrino flux from $E_{\rm min} = 10^{17.5}$ eV (green solid line : best fit, green dashed line : 99% C.L., green dotted line : without Fermi-LAT EGRB data) compared with the constraints from experiments. Without Fermi-LAT EGRB data, expected neutrino flux is much larger than with EGRB data (thin dotted green line). Image from [3].

2.2 Gamma-Ray Bursts

Gamma-Ray Bursts (GRBs) were first discovered in 1967 by Vela satellite network. These military based satellites detected bright γ-ray signals coming from space which was not expected. Multiple satellites with different spectrum responses have confirmed that these strange photon signals peaked in the gamma-ray range [49, 50].

GRBs have been monitored by many satellites which are dedicated to study GRBs. Beginng in 1991, the Burst and Transient Source Experiment (BATSE) aboard the Compton Gamma Ray Observatory (CGRO) collected GRB data [25]. The GRB distribution map from BATSE shows that GRBs are isotropically distributed (Fig. 2.7). This distribution indicates that GRBs are originated from cosmological distances, in other words, they are located outside of our galaxy [51]. It was an astonishing discovery to notice that GRBs are extragalactic sources as it was difficult to imagine such an energetic astrophysical event, so energetic that we can measure the strong signal from such a far distances ($\sim$ Gpc). In 2004 NASA's Swift satellite began to search GRBs with small sky coverage ($\sim 1/3$ of BATSE's field of view) but much more precise measurement in spectrum and wavelengths than BATSE. In 2008, the Fermi Gamma-ray Space Telescope (FGST) launched and it is currently collecting GRB events while performing an all-sky survey. Based on the measurements from many GRB telescopes, the understanding about the GRB phenomenon has been expanded and more GRB models that describe the measurements are developed.

The Fireball shock model is widely accepted as a standard GRB model where relativistic plasma in a jet collides to produce high energy prompt emission. The Fireball model decouples the inner engine of the source from the mechanism of the gamma-ray emission from the source. It assumed that the unknown inner engine is a compact energy source that can initiate the ultra-relativistic outflow.

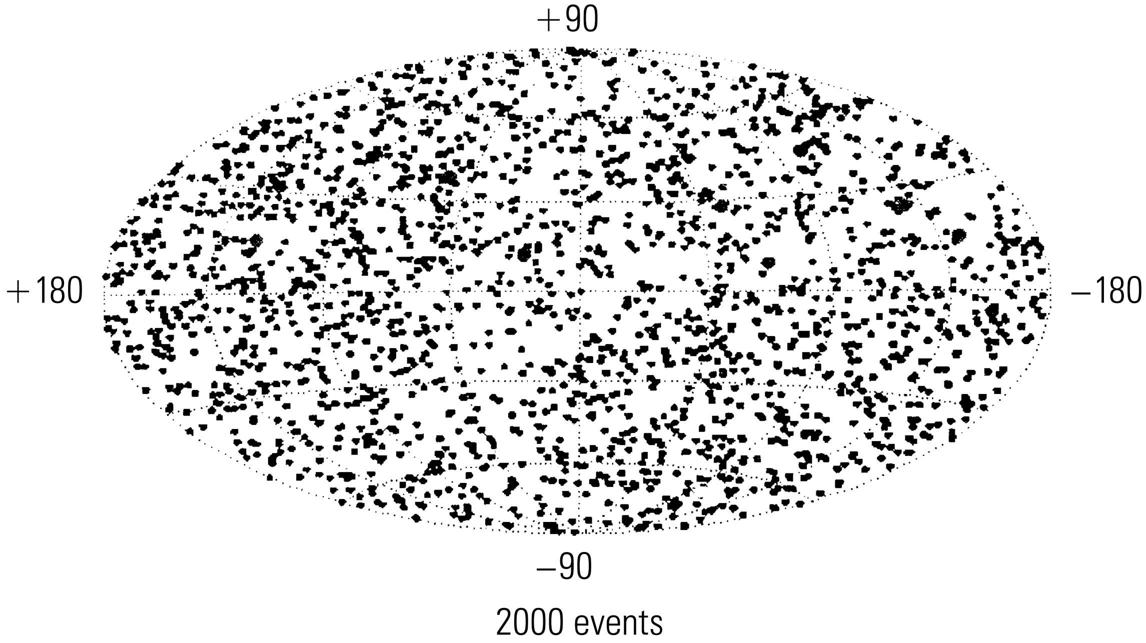

Figure 2.7: GRB distribution plot in Galactic coordinates from 2000 GRBs detected by BATSE. GRBs are isotropically distributed which indicates that GRBs are extragalactic source.

The outflow consist of multiple layers, and when the two layers of outflow collide, it generates an internal shock. The shocks will produce gamma rays by synchrotron radiation and inverse Compton scattering. Protons are also expected to be accelerated during this process by shock acceleration. When there are high energy protons and photons (gamma rays), neutrinos can be produced via $p-\gamma$ interactions (Eq. 2.1 but replacing γ_{CMB} with photons from the jet). This early stage of emission from internal shocks are called prompt emission and the measured gamma ray signals are expected predominantly from this prompt emission.

After the prompt emission, there is a second stage of emission from the Fireball model which is called afterglow. When the outflow expanded far enough ($> 10^{18}$ cm) to interact with external matter such as interstellar medium, the collision between the outflow and the external medium produces shocks. These external shocks will generate photons down to radio frequencies due to the deceleration of the outflow.

Waxman and Bahcall (WB) have created an analytic GRB neutrino production model [26] based on the Fireball model. For our GRB analysis, we chose to use a numerical calculation to obtain GRB neutrino fluences instead of the simple analytic (and outdated) WB GRB neutrino fluence model.

2.3 Other Models (other than GZK, GRB models)

There are many models which estimate the UHE neutrino flux without the GZK process or GRBs. In this section, AGNs [52,53], the Waxman-Bahcall (WB) bound [54], Topological Defects (TDs) [55,56] and Z-burst models [57,58] are introduced as examples of UHE neutrino models or constraints from sources other than the GZK process and GRBs.

The emission lines in the nuclei of galaxies were recognized in early 1900s [52]. However the theory of AGNs took decades to be considered as a serious research topic until the discovery of quasars and supermassive black holes (10^6 to 10^{10} times the mass of the Sun) in the center of galaxies. In the current standard AGN model, an AGN consists of an accretion disk and relativistic jets. An accretion disk will form when surrounding material is dissipated toward the center of a supermassive black hole. Also two highly relativistic jets are aimed toward opposite directions from close to the disk. When the jet is pointing toward the observer, this specific type of AGN is called blazar [59]. Although the analyses in this paper don't include an AGN neutrino search, AGNs are expected to be the most luminous and distant object in the universe. Once we figure out reliable AGN neutrino flux models, we can expand our UHE neutrino flux limit to AGNs in future analyses.

In 1998, Waxman and Bahcall proposed a highly intuitive model which defines the limit for the UHE neutrino flux. The Waxman-Bahcall bound assumes that the sources are optically thin to π photo-production. This means that, when high energy protons are produced inside the source, they assumed that there is only one interaction to create neutrinos. After this one interaction, protons can travel to Earth as a cosmic rays. Using these assumptions, Waxman and Bahcall could calculate the neutrino intensity ($E_\nu^2 J_\nu$) based on cosmic ray data. They set the injection spectrum of protons from the source as $dN_{CR}/dE_{CR} \propto E_{CR}^{-2}$, which is the typical spectrum for Fermi acceleration [60].

Fermi acceleration occurs when charged particles get boosted by a magnetic mirror, or shock. AGN jets, for example, have continuous impulsive magnetic shocks, and when charged particles get reflected between two shocks, they will boosted to ultra high energies. Using the energy production rate for protons between $10^{19} - 10^{21}$ eV in [60], the cosmic ray generation rate is given by

$$E_{CR}^2 \frac{d\dot{N}_{CR}}{dE_{CR}} \approx 10^{44}\,\mathrm{erg\ Mpc^{-3} yr^{-1}}. \tag{2.16}$$

Using Eq. 2.16, we can calculate the present day energy density of muon neutrinos under this model considering of a few other factors. First, we can get the total muon neutrino energy density (for ν_μ and $\bar{\nu}_\mu$ summed) by

$$E_{\nu_\mu}^2 \frac{dN_{\nu_\mu}}{dE_{\nu_\mu}}\bigg|_{max} \approx 0.25\, t_H\, E_{CR}^2 \frac{d\dot{N}_{CR}}{dE_{CR}} \tag{2.17}$$

where factor 0.25 is obtained from a factor for the probability of a proton yielding a muon neutrinos and t_H is a Hubble time factor, $t_H \approx 10^{10}$ yr [5] in order to account present-day energy density. There is a factor of 1/2 for the probability that a charged pion is produced (by $p + \gamma \rightarrow \pi^+ + n$) instead of a neutral pion (by $p + \gamma \rightarrow \pi^0 + p$). After the π^+ is produced, π^+ will eventually decay into four different leptons including muon neutrinos, $\pi^+ \rightarrow e^+ + \nu_e + \nu_\mu + \bar{\nu}_\mu$. And another factor of 1/2 for the probability of π^+ decaying into ν_μ and $\bar{\nu}_\mu$ which combination of two 1/2 factors make 0.25 factor shown in Eq. 2.17. Eq. 2.17 is the maximum total muon neutrino energy density as it assumes entire proton energy transferred to π in one π photo-production process.

With the maximum total muon neutrino energy density in Eq. 2.17, the maximum expected total neutrino flux (for all ν_e, ν_μ and $\bar{\nu}_\mu$) is

$$\begin{aligned} E_\nu^2\, \Phi_\nu\bigg|_{max} &\approx \frac{3}{2}\,\frac{c}{4\pi}\cdot E_{\nu_\mu}^2 \frac{dN_{\nu_\mu}}{dE_{\nu_\mu}}\bigg|_{max} \\ &\approx \frac{3}{2}\,\frac{c}{4\pi}\cdot 0.25\, \xi_Z\, t_H\, E_{CR}^2 \frac{d\dot{N}_{CR}}{dE_{CR}} \\ &\approx 2 \times 10^{-8} \xi_Z \text{ GeV cm}^{-2}\text{s}^{-1}\text{sr}^{-1}. \end{aligned} \tag{2.18}$$

where the factor 3/2 is the ratio between $\nu_\mu + \bar{\nu}_\mu$ and ν_e fluxes, and the quantity ξ_Z is a factor for redshift evolution. In [54], they calculated the redshift evolution factor ξ_Z for a quasi-stellar object source (which has rapid redshift evolution) and for non-redshift evolution, and came up with $\xi_Z \sim 3$ and $\xi_Z \sim 0.6$ respectively. In Fig. 2.4, calculated WB constraints are shown. The upper dash-dotted line is a constraint with rapid redshift evolution ($\xi_Z \sim 3$) and lower dash-dotted line is a constraint with non-redshift evolution ($\xi_Z \sim 0.6$).

TD models postulate that there was a very massive unknown particle produced in the early universe [55, 56] which decayed into UHECRs that we now observe. From Grand-Unified Theories (GUTs), the mass of this unknown particle is required to be $\sim 10^{24}$ eV. So, the spectrum of UHECRs decayed from this unknown massive particle should extend to the rest mass energy of the particle.

The Z-burst model predicts that the relic neutrino background, produced in the early epoch of universe, interacts with UHE neutrinos, resulting in annihilation of both through the $\nu + \bar{\nu} \rightarrow Z_0$ process [57, 58]. The Z_0 then decays into hadronic secondary particles which include UHE neutrinos. The Z-burst model, however, is ruled out by ANITA experiment (Fig. 3.5).

Chapter 3

Past and Present Experiments for UHE neutrino

In this chapter, we discuss experiments in the past and on-going that are searching for UHE neutrinos. Before going through the list of experiments, we first define two detection methods, the optical and radio Cherenkov radiation techniques, and discuss what is complementary between the two methods. The Radio Ice Cherenkov Experiment (RICE), Goldstone Lunar Ultra-high energy neutrino Experiment (GLUE), Antarctic Impulsive Transient Antenna (ANITA), Antarctic Ross Iceshelf Antenna Neutrino Array (ARIANNA) and IceCube are introduced.

3.1 Detection Methods: Optical and Radio Cherenkov Radiation

There are two main methods for detecting neutrino signals: optical and radio Cherenkov techniques (radio Cherenkov radiation is induced by what is also called the Askaryan effect [61, 62]). When a UHE neutrino passes through a high density dielectric medium such as ice, either charged current (CC) or neutral current (NC) scattering from nucleon occurs:

$$\text{CC}: \qquad \nu_l + n \rightarrow l^- + p, \qquad \bar{\nu}_l + p \rightarrow l^+ + n \tag{3.1}$$

$$\text{NC}: \qquad \nu_l + N \rightarrow N + \nu_l, \qquad \bar{\nu}_l + N \rightarrow N + \bar{\nu}_l \tag{3.2}$$

where ν_l can be either ν_e, ν_μ, or ν_τ, and the nucleons N in Eq. 3.2 can be either p or n. In Equation 3.1 and 3.2, while charged current scattering produces an electromagnetic cascade and/or hadronic cascade, neutral current scattering only produces a hadronic cascade from a target nucleon (N in Eq. 3.2). In an ν_e charged current interaction, the final state electron will produce an electromagnetic cascade (Fig. 3.1), while the target nucleon will produce a hadronic cascade. Charged current scattering from a ν_μ will produce only a hadronic cascade as the final state μ will penetrate the medium without producing any electromagnetic cascade up to energy approximately 1 TeV [5]. Above a TeV, the dominant energy loss process for μ becomes radiative loss and through radiation, there will be an electromagnetic cascade. So, in the UHE regime, μ will produce an electromagnetic cascade. A τ created through charged current scattering by a ν_τ can produce electromagnetic and/or hadronic cascades through its decay and/or subsequent interactions.

When charged particles produced in an electromagnetic or a hadronic cascade move faster than the speed of light in the medium, they can create Cherenkov radiation. Cherenkov radiation is emitted preferentially at an angle θ with respect to the direction of the charged particle, where the angle depends on the speed of the particle (Fig. 3.2) and the medium. The relation between the angle θ and the speed of the charged particle is $\cos\theta = 1/(n\,\beta)$, where β is the speed as a function of the speed of light ($\beta = v/c$), and n is the refraction coefficient of the medium.

Experiments that use the optical Cherenkov technique detect the Cherenkov radiation produced as optical light with optical light detectors such as photo-multiplier tubes (PMTs). Optical Cherenkov radiation is emitted from individual charged particles in an electromagnetic or a hadronic cascade. Detecting optical light with a PMT is a very straight forward, well-established technology. The only disadvantage of detecting optical light is that it is very costly to make an extremely large detector (larger than 1 km^3) using the optical light detecting technology currently available. Optical light can travel through the medium (e.g. ice) for only $\sim$ 10's meters due to the attenuation length of $\sim 50\ m$ [33], so a few 10's of meters is the maximum allowable distance between PMTs. Radio Cherenkov detectors overcome this disadvantage of optical Cherenkov detectors.

The radio Cherenkov technique uses the coherent radio emission from the charge asymmetry of entire cascade. Pair annihilation ($e^+ + e^- \rightarrow \gamma + \gamma$), Compton scattering ($\gamma + e^- \rightarrow e^- + \gamma$), and the photoelectric effect ($\gamma + \mathrm{A} \rightarrow \mathrm{e}^- + \mathrm{A}'$) would induce a charge asymmetry of approximately 20% during shower development. This is because positrons in the cascade will annihilate with target electrons in the medium (pair annihilation), and high energy photons will scatter off target electrons in the medium (Compton scattering) which then become part of the shower. The photoelectric effect will remove an electron from an atom in the medium. Hence, an electromagnetic cascade will be negatively charged by processes which increase the number of electrons (Compton scattering and photo electric effect), and a process which decreases the number of positrons (pair annihilation). The negatively charged electromagnetic cascade produces Cherenkov radiation which is coherent in radio frequency. As the Cherenkov radiation is a short impulse in the time domain, the signal will have a wide bandwidth in the frequency domain. The Molière radius (the radius at the maximum cascade shower) for a cascade in ice is approximately 10 cm and it sets the minimum

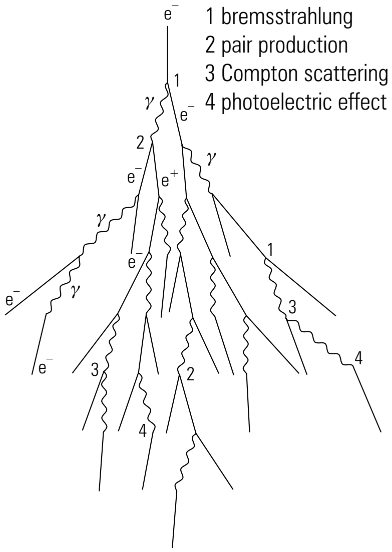

Figure 3.1: Schematic of electromagnetic cascade due to electron. Image from [6].

wavelength where coherence occurs as ~ 10 cm in the ice and the corresponding frequency is ~ 3 GHz. So, we can use frequencies up to 3 GHz as a coherent signal from the cascade due to the radio Cherenkov radiation in ice.

The coherent radio Cherenkov signal will have a stronger amplitude and longer attenuation length compare with the optical Cherenkov signal. Attenuation length for radio waves in ice is approximately 700 m [32] while the optical light is as high as approximately 10 m [33]. Along with the strong amplitude of the signal, long attenuation lengths make it possible to use the radio Cherenkov technique for extremely large detectors at relatively low cost. For the next subsection, we examine some past experiments which used the radio Cherenkov and optical Cherenkov techniques. We will first look at experiments that have used the radio Cherenkov technique.

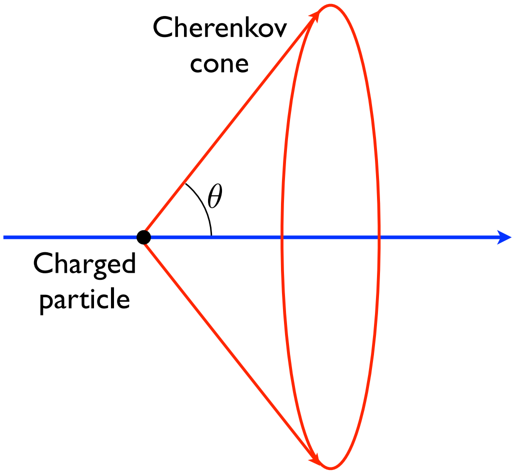

Figure 3.2: Basic schematic of Cherenkov radiation. Charged particle moves along with the blue arrow, and Cherenkov radiation is shown as a red cone.

3.2 Radio Ice Cherenkov Experiment (RICE)

RICE was an experiment which sought to detect UHE neutrinos interacting in the ice in Antarctica [63]. It used the radio Cherenkov technique to search for radio frequency signals from neutrinos, and was composed of a 16 channel array of antennas deployed along a string of the AMANDA detector, a predecessor of IceCube. With these antennas, RICE monitored over 15 km^3 of ice to search for radio emission from neutrinos. Antennas were deployed within a 200 m $\times$200 m $\times$200 m cube at 100 $-$ 300 m depth. RICE triggered when the signal in four antennas exceeded a threshold in a 1.2 μs time window, which is the time for a radio signal to cross a 200 m detector length at the speed of light. When the trigger was satisfied, signals were saved through the Data Acquisition Module (DAQ) for event reconstruction. In August 2000, RICE was operated with a livetime of $\sim$ 333.3 hrs. Although they did not detect any UHE neutrino candidates, they did set a bound on the neutrino flux (see Fig. 3.5 and 3.6), and demonstrated that the radio Cherenkov is a promising technology for detecting UHE neutrinos. The neutrino flux limit from RICE was the best limit at energies above 10^{19} eV before ANITA.

3.3 Goldstone Lunar Ultra-high energy neutrino Experiment (GLUE)

The GLUE experiment also used the radio Cherenkov technique [7]. GLUE, however, used a much larger detection medium, namely the Moon, to search for radio Cherenkov emission. They used the Deep Space Network antennas in Goldstone, CA [64]. In particular, they used the shaped-Cassegrainian 70 m antenna DSS14, and 34 m beam-waveguide antenna DSS13. The two antennas are separated by 22 km, and the DSS14 antenna can receive right and left circular polarization (RCP and LCP) waveforms, while the DSS13 antenna can operate at two different frequencies (high frequency, $\sim$ 300 MHz and low frequency, $\sim$ 150 MHz). With these two antennas, they were sensitive to radio emission from UHE neutrinos. RCP and LCP signals detected in coincidence would indicate that the waveform is highly linearly polarized, which is expected for Cherenkov radiation. Also, they selected broadband signals by requiring a coincidence between high frequency and low frequency signals. Despite this well-developed technology, however, with the small effective solid angle and the short livetime (120 hours), GLUE did not detect any UHE neutrino candidate signals and set a limit on the UHE neutrino flux above 10^{20} eV (Fig. 3.5).

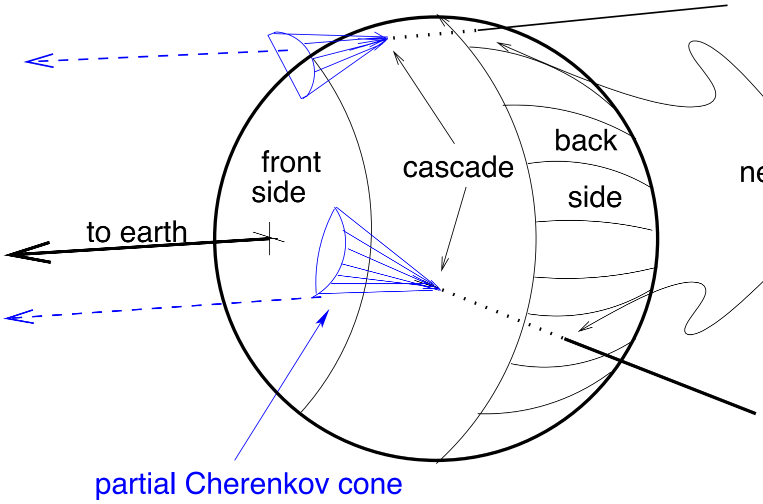

Figure 3.3: Basic schematic for detecting the Askaryan effect in the moon. Image from [7].

3.4 Antarctic Impulsive Transient Antenna (ANITA)

ANITA is a current UHE neutrino experiment using the radio Cherenkov technique. It uses a NASA long duration balloon to fly antennas in high altitude over the Antarctic ice. From approximately 37 km altitude in the sky, ANITA can scan ~ 1.6 Mkm^3 of ice. The basic schematic for detecting radio Cherenkov by ANITA is shown in Fig. 3.4.

In early 2004, a prototype experiment called ANITA-lite [8], flew with a livetime of $\sim$ 10 days. Using only two antennas, ANITA-lite placed stronger constraints than GLUE in the same energy regime and ruled out Z-burst models (Fig. 3.5). ANITA-1 flew for 35 days (livetime $\sim$ 17.3 days) looking for radio waveforms in December 2006. ANITA-1 included 32 antennas which could detect vertical and horizontal polarized

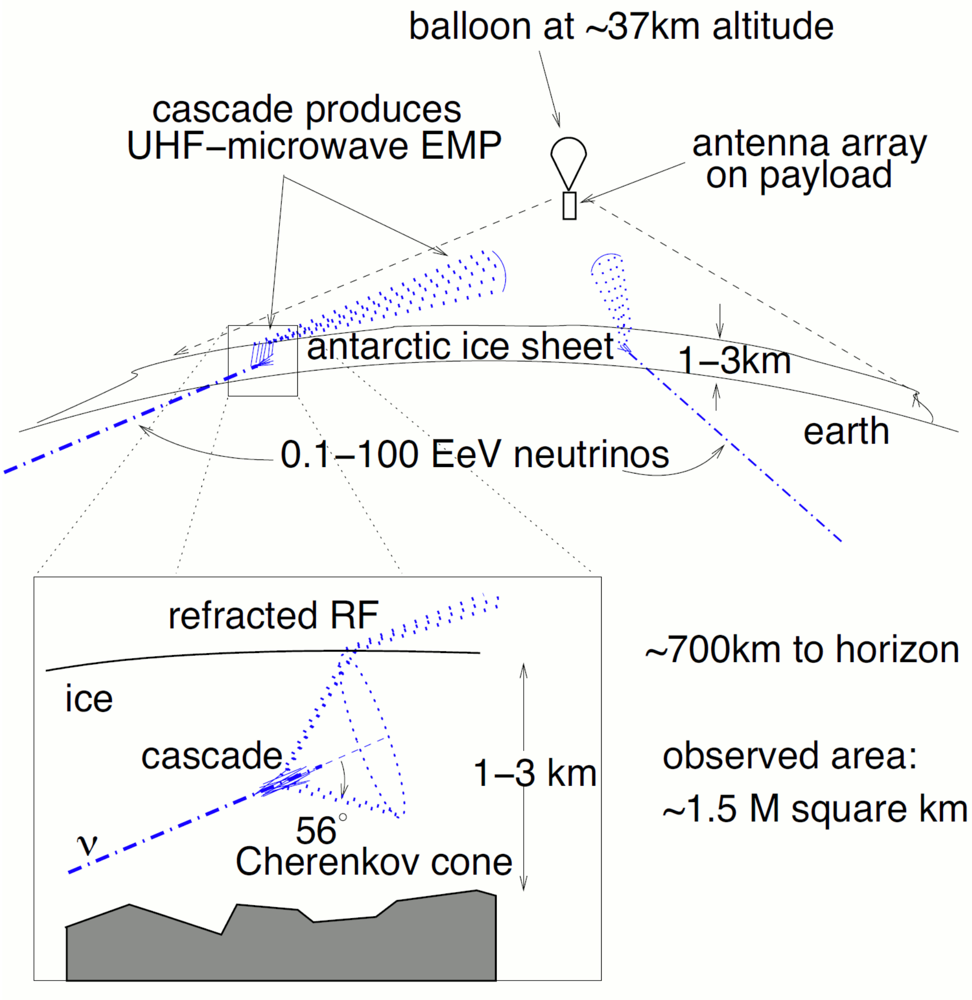

Figure 3.4: Basic schematic of detecting Askaryan effect by ANITA.

waveforms, and each antenna had a 200−1200 MHz bandwidth. In the trigger, they divided the full bandwidth into four different sub-bands, and required coincidences between the four bands to trigger candidate signals, so that triggered signals are broadband. Also as candidate signals are produced inside the ice and ANITA detects the top of the Cherenkov cone (Fig. 3.4), the candidate signals are required to be vertically polarized. However, ANITA-1 also did not detect any candidate neutrino signals during its flight, but set stricter limits on the neutrino flux (Fig. 3.6).

ANITA-II [9], which flew in January 2009 for 31 days (livetime $\sim$ 28.5 days), had an improved sensitivity to UHE neutrinos. Compared to ANITA-1, ANITA-2 reduced the front-end system noise by $\sim$ 20 %, had 8 more antennas for a better angular resolution and a lower trigger threshold. After data analysis, they detected one [9] candidate neutrino signal during the flight. In their background estimation, however they expected 0.97 ± 0.39 events due to thermal and anthropogenic background events. Thus, one candidate signal was consistent with the background estimation, which means we can not say whether the detected signal is a real neutrino signal or not. ANITA-3 is in preparation as a next flight, and it will be launched in the 2014-2015 season.

3.5 IceCube

IceCube [29] is, so far, the largest optical Cherenkov experiment for detecting UHE neutrinos. It is monitoring $\sim$ 1 km^3 of ice with photo-multiplier tubes (PMTs) deployed at a $1450-2450$ m depth in the ice (Fig. 3.7). IceCube detects optical Cherenkov radiation, instead of the radio Cherenkov. They have deployed strings in the ice with inter string spacing of about 125 m on which PMTs are attached about 17 m apart. It took approximately 7 years (from 2005 - 2011) to deploy all 86 strings. Even before deploying all 86 strings, IceCube had gathered an enormous amount of experimental data with its large size. Fig. 3.8 shows the neutrino flux limit from IceCube [11] which is currently the best limit below 10^{19} eV range. After full 86 strings have been deployed, IceCube started to detect extraterrestrial origin neutrinos. From the three years data set with livetime of 988 days, IceCube detected 37 neutrino candidate events with energies between 30 and 2000 TeV [65]. These IceCube starting neutrinos events are a milestone in astrophysics as they are the first detected extraterrestrial neutrino events other than the neutrino events from

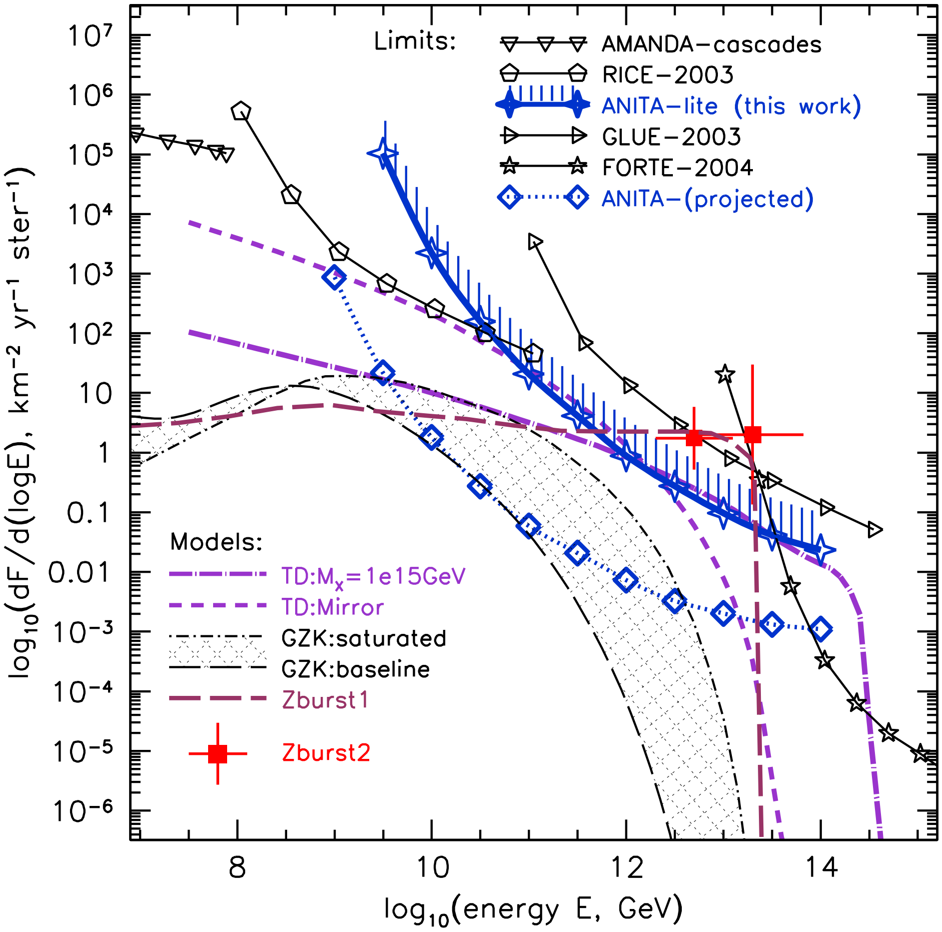

Figure 3.5: Constraints from GLUE, RICE, FORTE, AMANDA, and ANITA-lite compared with TD, GZK, and Z-bust models for UHE neutrinos. Z-burst models are ruled out by ANITA-lite. Image from [8].

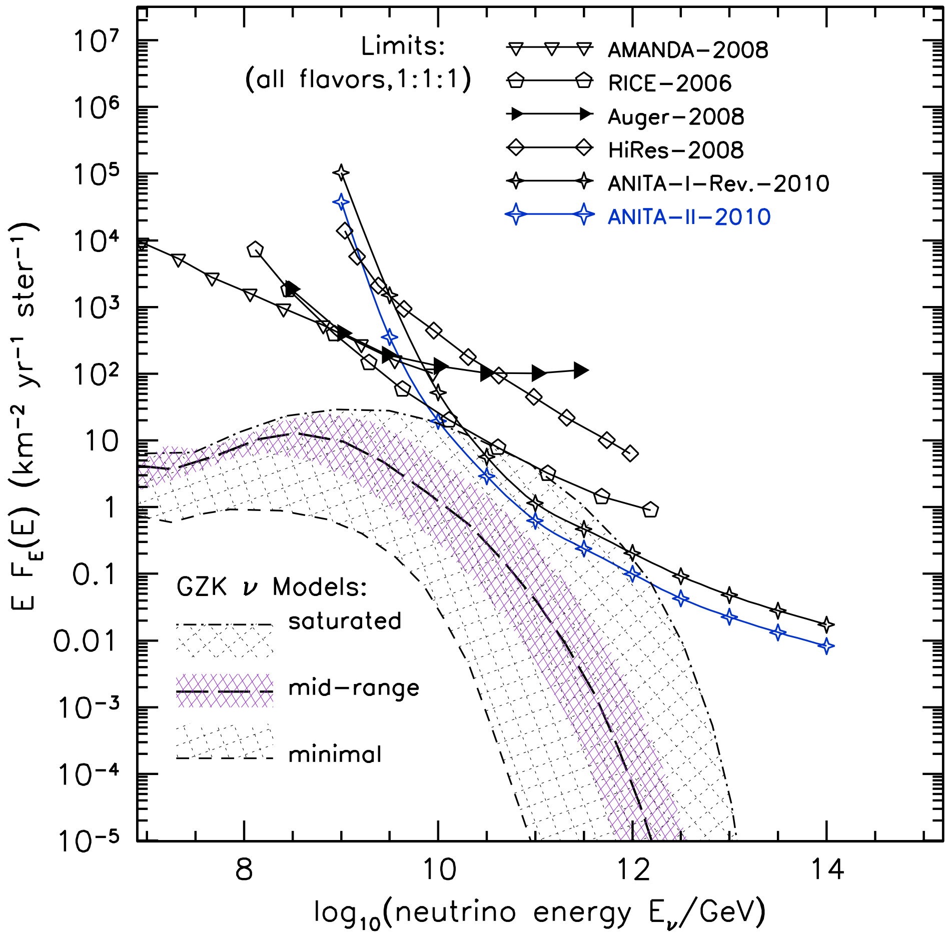

Figure 3.6: Constraints from RICE, Auger, HiRes, ANITA-I, and ANITA-II. Saturated GZK neutrino models are ruled out by ANITA-I and ANITA-II. Image from [9].

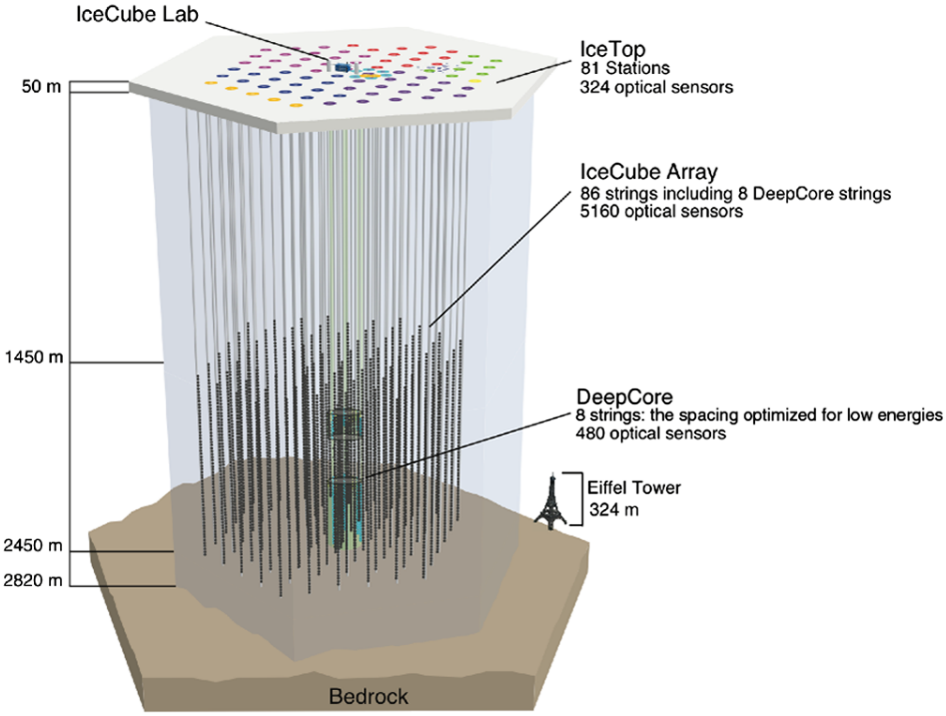

Figure 3.7: Basic schematic of IceCube. Image from [10]

SN 1987A. The energies of detected neutrino events from IceCube are approximately two orders of magnitude lower than ARA's energy threshold.

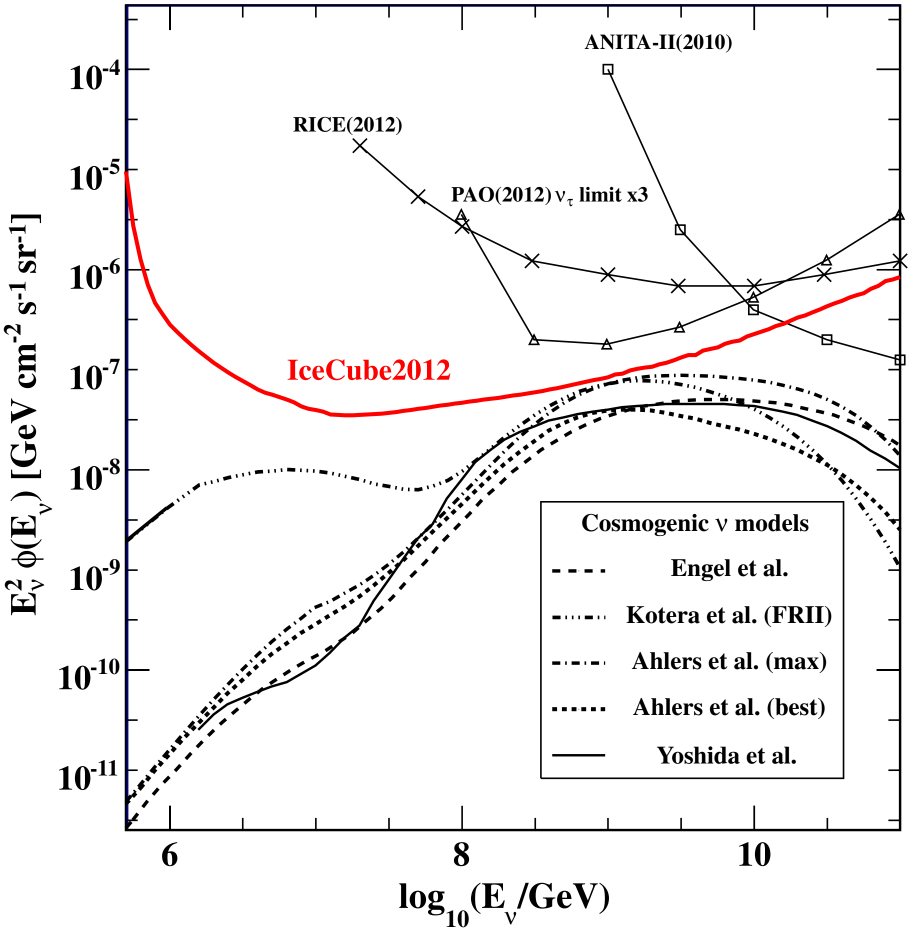

Figure 3.8: Constraints from IceCube (red curve) and other experiments with 1:1:1 neutrino flavor assumption. Currently, IceCube has the best neutrino flux limit below 10^{19} eV. Image from [11]

Chapter 4

Askaryan Radio Array

The contents of this chapter are largely taken from [2].

The first radio array in ice to search for UHE neutrinos, RICE, was deployed along the strings of the AMANDA detector, an IceCube predecessor, and placed competitive limits on the UHE neutrino flux between 10^{17} and 10^{20} eV [66]. Next-generation detectors are under construction aiming to reach the 100's of km^3 target volume of ice. The Askaryan Radio Array (ARA) [31] is one such detector being deployed in the ice at the South Pole and the first physics results from a prototype station of this detector are presented in this paper.

ARA aims to deploy 37 stations of antennas at 200 m depth spanning 100 km^2 of ice as shown in Fig. 4.1. A schematic of a design station is shown in Fig. 4.2. A design station consists of eight horizontally polarized (HPol) and eight vertically polarized (VPol) antennas at depth and four surface antennas for background rejection and cosmic ray detection via the geomagnetic emission in the atmosphere. The 200 m design depth was chosen because it is below the firn layer, where the index of refraction varies with depth due to the gradual compacting of snow into ice down to ~ 150 m depth. The trigger and data acquisition are handled by electronics at the surface of the ice at each station.

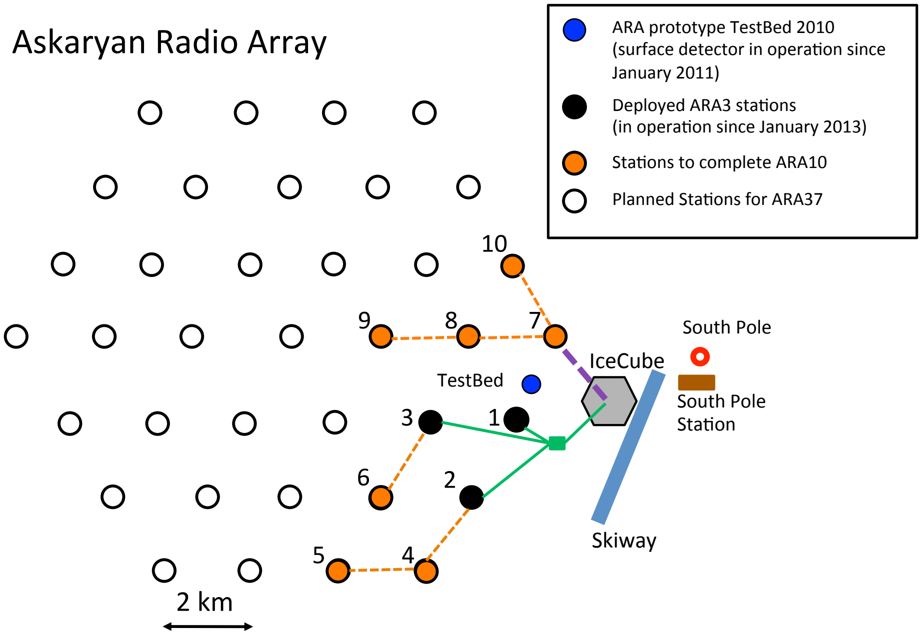

Figure 4.1: Diagram showing the layout of the proposed ARA37 array, with the location of the Testbed and the first three deployed deep stations highlighted in blue and black respectively, and proposed stations for the next stage of deployment, ARA10, highlighted in orange.

To date, one ARA prototype Testbed station and three full stations have been deployed in the ice. The Testbed station was deployed at a depth of $\sim$ 30 m in the 2010-2011 drilling season. The first full station, A1, was deployed at a depth of 100 m in the 2011-2012 drilling season. The next two stations, A2 and A3, were deployed at the 200 m design depth during the 2012-2013 season. At the time of publication, station A2 and A3 are operational.

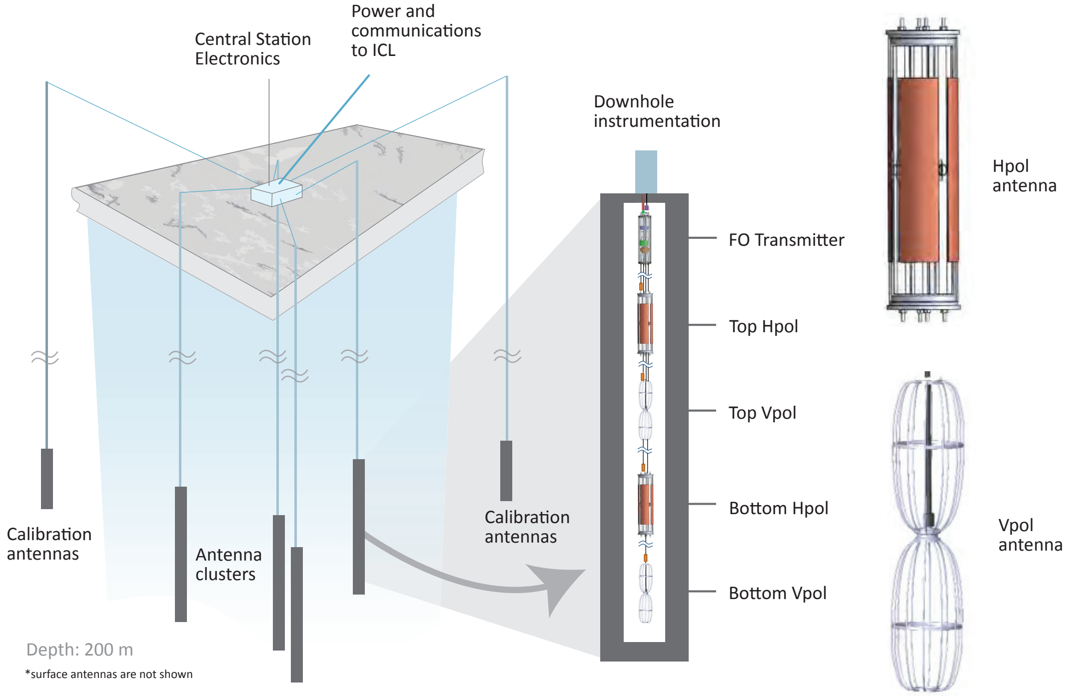

Figure 4.2: Diagram showing the layout of a design station and antennas. Each station on Fig. 4.1 (one circle on the plot) has the layout shown on this plot. There are four boreholes for receiving antenna clusters where each borehole has two Vpol antennas and two Hpol antennas. There are two additional boreholes for calibration transmitting antennas. Each calibration pulser borehole has one Vpol and Hpol transmitter antennas. There is central station electronics on the surface of the ice, which includes DAQ and power supply box.

4.1 Testbed

The ARA prototype Testbed station differs from the layout of the design stations for the full array. A more complete description of the design and operation of the Testbed station can be found in [31].

Table 4.1 summarizes the antenna types and deployed positions in the Testbed which are depicted in Fig. 4.3. Here we use the Testbed-centric coordinate system

Hole	channel number	x (m)	y (m)	Type, Pol	Depth (m)
BH 1	0	-8.42	-4.40	BSC, H	20.50
	3			Bicone, V	25.50
BH 2	5	-0.42	-11.13	BSC, H	27.51
	2			Bicone, V	22.51
BH 3	7	9.22	-6.15	BSC, H	22.73
	4			Bicone, V	27.73
BH 5	1	3.02	10.41	BSC, H	30.56
	6			Bicone, V	25.56
BH 6		-9.07	3.86	QS, H	26.41
				QS, H	30.41
S1		-2.48	-1.75	Discone, V	1.21
				Batwing, H	2.21
S2		4.39	-2.41	Batwing (H)	1.19
S3		1.58	3.80	Discone (V)	1.19
S4				Fat Dipole (H)	
Cal 1		-23.18	17.90	H	17.50
				V	22.50
Cal 2		-2.25	-29.81	H	34.23
				V	29.23
Cal 3		27.67	13.57	H	1.13
		28.69	12.35	V	1.13

Table 4.1: Types and positions of antennas as deployed in the ARA Testbed. See the text for the description of antenna types.

with the origin at the southeast corner of the DAQ box on the surface of ice, $+\hat{x}$ pointing along the direction of ice flow and the $\hat{x} - \hat{y}$ plane tangent to the earth's geoid shape at the surface.

As with the deep stations, the Testbed antennas deployed in boreholes were designed to be broadband, with a mixture of HPol and VPol, subject to the constraint that they must fit down the $\sim$ 15 cm diameter hole in the ice. For VPol, a wire-frame hollow-center biconical design was chosen with an annular-shaped feed with the string cable running through the center. These "Bicones" have a bandwidth of

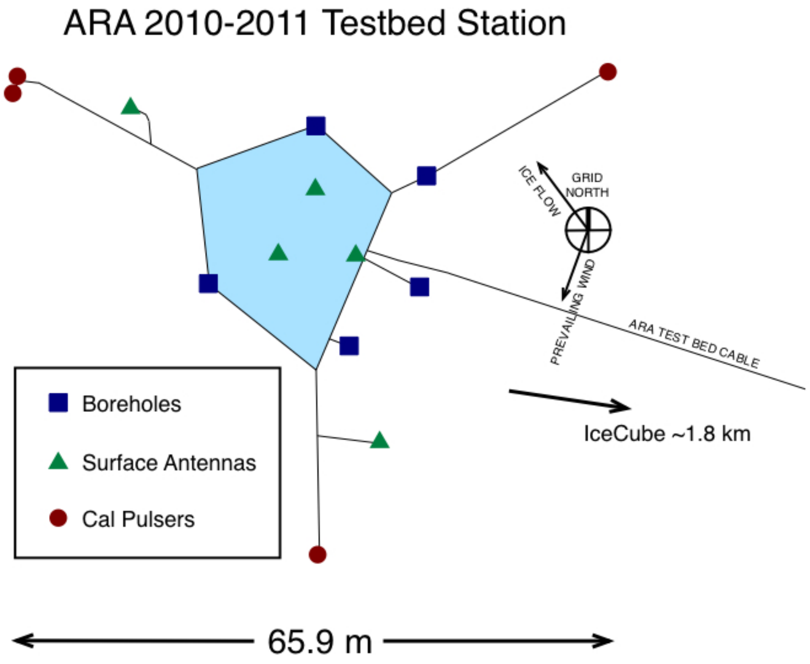

Figure 4.3: Schematic of the ARA Testbed station.

150-850 MHz, and four were deployed in boreholes and two near the surface. For HPol, two designs were used in the Testbed, the bowtie-slotted-cylinder (BSC) and the quad-slotted-cylinder (QSC). The BSCs were used in four borehole antennas and a pair of QSC's in the fifth borehole. Photos for bicone, BSC, and QSC antennas are shown in Fig. 4.4.

Larger antennas were deployed at the surface. Two discone antennas (VPol) and two Batwings (HPol) were deployed 1-2 m from the surface. Additionally, two fat dipoles with a bandwidth of 30-300 MHz were deployed within a meter of the surface to assess the feasibility of detecting geosynchotron RF emission from cosmic rays, which has a lower frequency content than the Askaryan emission expected from neutrinos.

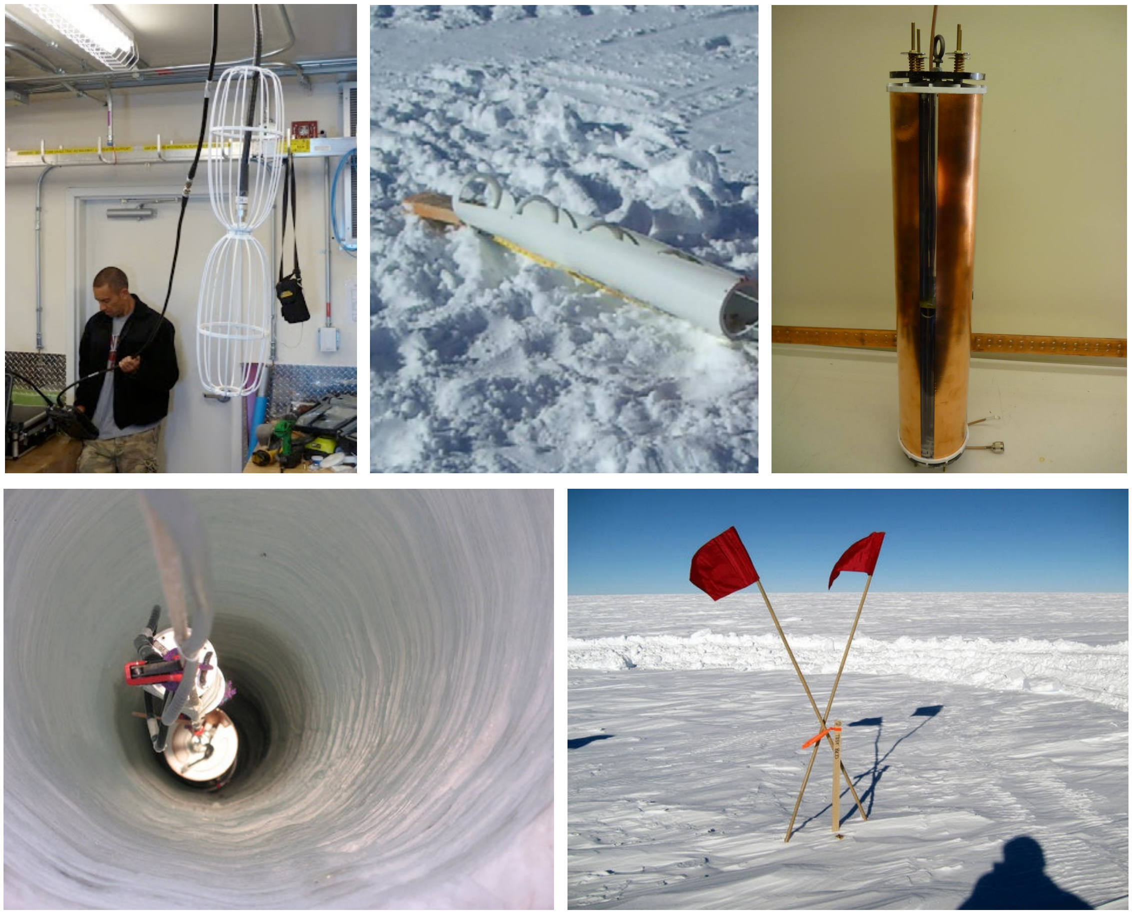

Figure 4.4: Photos taken from Testbed deployment. Top left: bicone Vpol antenna under test in South Pole station, top middle: bowtie-slotted-cylinder (BSC) Hpol antenna, top right: quad-slotted-cylinder (QSC), bottom left: string descending down a hole, bottom right: x-mark for locating the Testbed station.

Within 1 m of the antennas, a filter and low noise amplifier (LNA) prepare the signal for transmission to the electronics box at the surface. A notch filter at 450MHz removes the South Pole communications from the Land Mobile Radio handheld UHF systems. A bandpass filter sits just after each antenna and blocks power outside of our 150 MHz to 850 MHz band before amplification. The filtered signal in each antenna is then input to a low noise amplifier and transmitted to the surface. At the surface, a second stage ∼40 dB amplifier boosts the signals before they are triggered and digitized. After arriving at the electronics box at the surface, the signals are split into a path for the trigger, which determines when a signal is to be stored, and another path to the digitizer, which reads out the waveforms.

There are two different trigger modes in the Testbed, an RF trigger and a software trigger. An event passes the RF trigger when the output of a tunnel diode, a few-ns power integrator of the waveforms from each antenna reaching the trigger path, exceeds 5-6 times the mean noise power in three out of the 8 borehole antennas within a 110 ns coincidence window. Due to the differences in responses between channels, each antenna has a different power threshold and thus has different trigger rate between channels. The software trigger causes an event to be recorded every second to monitor the RF environment.

Once the station has triggered, the digitization electronics, which are descended from those developed for ANITA [67], process the waveforms and output them to storage. Here, in the digitizer path, the signal undergoes an analog-to-digital conversion using the LAB3 RF digitizer [67], and stored in a buffer (in the Testbed, the buffer was trivially one event deep). The signals from the "shallow" antennas are sampled at 1 GHz, while the signals from the eight borehole antennas were sampled twice, with an time offset of 500 ps for an effective sampling rate of 2 GHz. The digitized waveforms are ∼250 ns long and are centered within approximately 10 ns of the time the station triggered.

Three calibration pulser VPol and HPol antenna pairs were installed at a distance of ∼30 m from the center of the Testbed array to provide *in situ* timing calibration and other valuable cross checks related to simulations and analysis. An electronic pulser in the electronics box produces a ∼250 ps broadband impulsive signal at a rate of 1 Hz. This pulser is connected to one of the three calibration pulser antenna pairs and can transmit from either the VPol or HPol antenna in each pulser borehole. Having multiple calibration pulser locations provides a cross check for the timing calibrations of each channel. Also, the observation, or non-observation, of the constant pulse rate by the station provides an estimate of its livetime.

For the Testbed, an event filter selects one event from every ten events at random to be transmitted to the North by satellite and the remaining data is stored locally and hand-carried during the following summer season. For the other ARA stations, this filter is now optimized to select events that exhibit a causal trigger sequence and thus are more likely to be events of interest.

Chapter 5

Simulation: AraSim

The contents of this chapter are largely taken from [2].

The official simulation program for ARA is called AraSim, and is the one we developed and used for the analysis presented in this paper. AraSim is used for multiple other analyses at other institutions, including a neutrino search in deep stations. AraSim draws on ANITA heritage, but much of the program was custom developed for ARA. In this Chapter, we describe each step of the simulation process in AraSim in Section 5.1. In Section 5.2, in-depth description about the radio Cherenkov emission models in AraSim is given. In Section 5.3, we show how we calibrated AraSim using data from the Testbed.

5.1 Simulation Process

AraSim simulates neutrino events in multiple steps. Simulation processes include selecting neutrino interaction location in the ice, modeling neutrino absorption in the Earth, emitting the radio Cherenkov signal, determining the signal's propagation through the Antarctic ice, and modeling properties of the detector. A schematic plot of a neutrino event is shown in Fig. 5.1. Each individual simulation step is presented in following subsections.

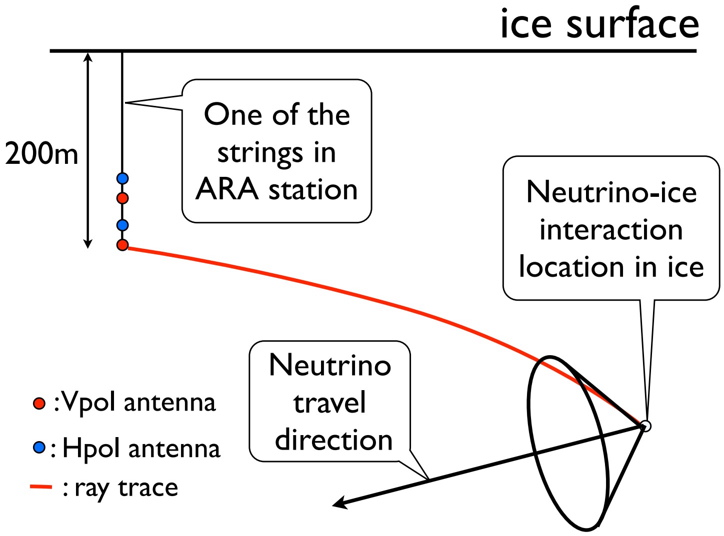

Figure 5.1: Basic schematic of a neutrino event. The cone at the neutrino-ice interaction location is the Cherenkov cone from coherent radio emission and the red curve is ray tracing between the antenna and neutrino-ice interaction location.

5.1.1 Selecting Neutrino-ice Interaction Location

AraSim generates neutrino events independent of each other, with interaction point locations chosen with a uniform density in the ice. For computational ease, neutrinos are generated within a 3-5 km radius around the center of a single station for neutrino energies from $E_\nu = 10^{17}$ eV-10^{21} eV, with the larger radii used for higher energies. For simulating multiple stations, neutrino interactions are generated up to 3-5 km beyond the outermost stations. For the diffuse neutrino search, AraSim randomly distributes the travel directions of the neutrinos over a 4π solid angle. AraSim can also set neutrinos to travel in certain directions for simulating point sources such as GRBs.

5.1.2 Earth Absorption Effect

Once the neutrino interaction location and travel direction is chosen, AraSim calculates the probability of the neutrino to reach the interaction location and not be absorbed by the Earth. The probability is calculated by

$$P = \prod_i e^{-l_i/L_i} \tag{5.1}$$

$$L_i = \frac{m_{\text{nucleon}}}{\rho_i \cdot \sigma} \tag{5.2}$$

where L_i is the interaction length at the layer of the Earth, l_i is travel distance at the layer of the Earth, m_{nucleon} is the mass of nucleon ($\sim 1.67 \times 10^{-27}$ kg), ρ_i is the mass density of the Earth layer i (~ 0.917 km/m^3 for ice), and σ is the neutrino-nucleon cross section. The parameters of each Earth layer are obtained from the Crust 2.0 Earth model and the energy-dependent cross sections are from [68]. We weight each event by this factor (P in Eq. 5.1) to account for absorption in the Earth.

5.1.3 Showers from Neutrino-ice Interaction

The primary shower comes from the initial neutrino-ice interaction. The energy for the electromagnetic and hadronic showers from the primary interaction are obtained from the inelasticity distributions from [68]. In addition to the showers from the primary interaction, AraSim considers any secondary interactions from μ or τ leptons that are generated from neutrino-ice charged current interactions. Electromagnetic and hadronic shower energies for the secondary showers are calculated from interaction probability tables obtained from the MMC particle generation code [69]. AraSim calculates the total energy of the primary showers, hadronic and electromagnetic if there is one, and the energy of the secondary showers and generates the RF signal from the interaction among them that produces the most shower energy as a first order estimation. From the energies of the electromagnetic and hadronic showers, we model the radio Cherenkov emission in AraSim. The detailed description about the radio Cherenkov emission models in AraSim is shown in Section 5.2.

5.1.4 Ray Tracing

After AraSim selects a neutrino interaction location in the ice and models the showers in ice, it obtains ray tracing solutions from the neutrino interaction location to each antenna. Ray tracing is not a trivial calculation as the Antarctic ice has a depth dependent index of refraction within ∼200 m of the surface.

There are two depth-dependent index of refraction models in AraSim. The one which we call the exponential fit model is used as the default index of refraction model if not stated. The exponential fit model is based on Besson et. al. [70, 71] measurements at the South Pole fit to an exponential function (Fig. 5.2). The alternative index of refraction model in AraSim is called the inverse exponential fit function. More detailed information and the systematic error on our result due to choice of index of refraction model is shown in Section 6.6.

Based on the depth-dependent index of refraction model, RaySolver, a in-ice ray tracing code [72], derives multiple ray-trace solutions between source and target. For depths within the firn (<150 m), this curvature effect is significant and large regions of the ice beyond ∼1 km away have no ray-trace solutions to the antennas as can be seen in Fig. 5.3.

RaySolver has a multi-step processes to optimize the computation time. For the first step, it uses an equation, which is driven from Snell's law, that is not analytically

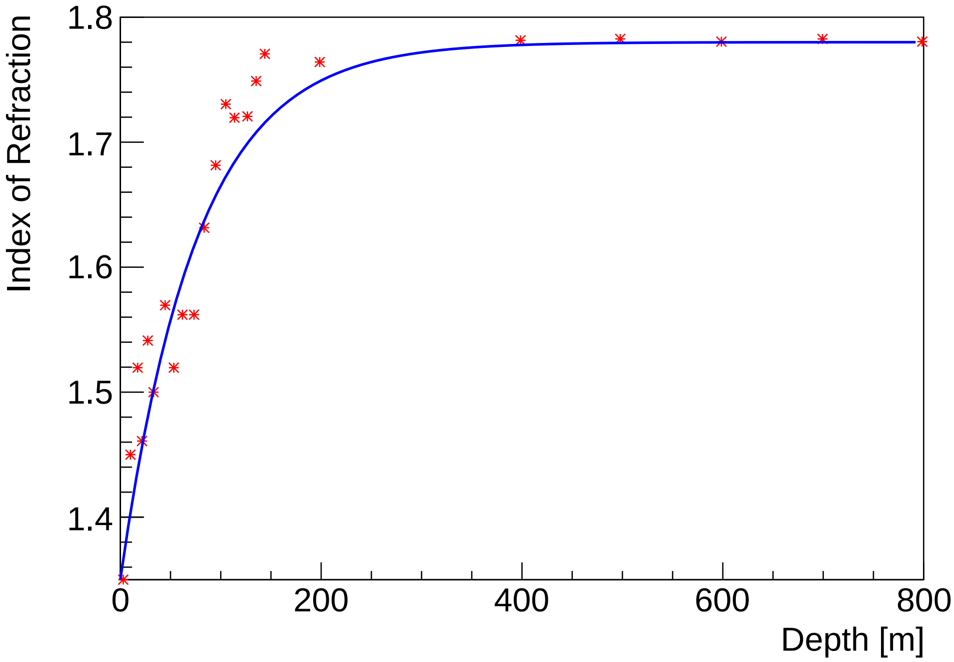

Figure 5.2: Antarctic ice index of fraction measurements (red crosses) at the South Pole and its fit result (green curve). The fit function is $n(z) = a1 + a2 \times (1.0 - \exp(b1 \cdot z))$ (exponential fit model) where $n(z)$ is the index of refraction and z is the depth. Data points are digitized from [70].

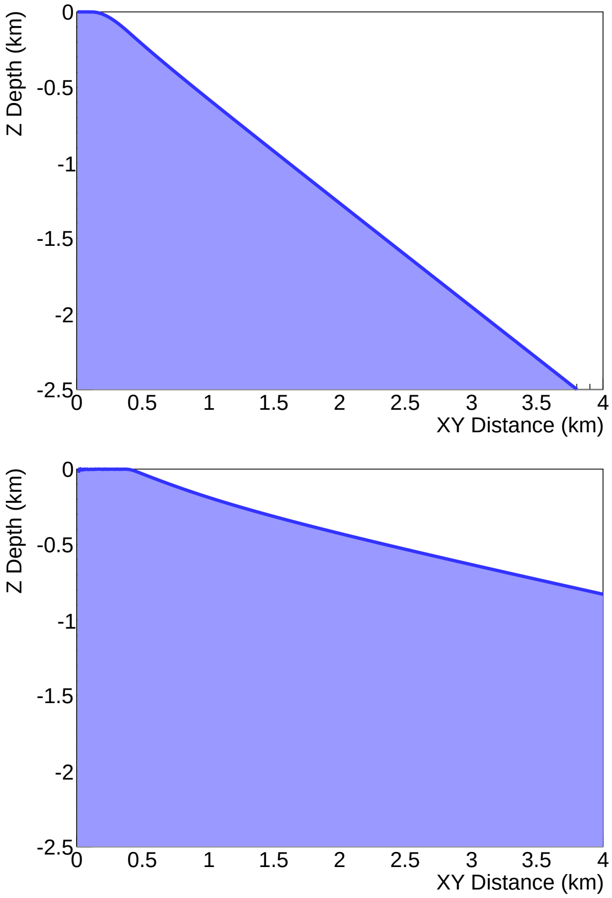

Figure 5.3: Plot showing the regions with ray-trace solutions for an antenna depth at 25 m (top) and 200 m (bottom). The greater depth allows an antenna at 200m depth to observe a larger volume of the ice.

solvable but can be solved numerically (see Appendix):

$$\begin{aligned}
&\ln\left(\frac{\sqrt{n^2-\sigma_0^2 n_0^2}+\sqrt{A^2-\sigma_0^2 n_0^2}}{n-A}+\frac{A}{\sqrt{A^2-\sigma_0^2 n_0^2}}\right)\\
&-\ln\left(\frac{\sqrt{n_0^2-\sigma_0^2 n_0^2}+\sqrt{A^2-\sigma_0^2 n_0^2}}{n_0-A}+\frac{A}{\sqrt{A^2-\sigma_0^2 n_0^2}}\right)\\
&+\frac{C\sqrt{A^2-\sigma_0^2 n_0^2}}{\sigma_0 n_0}(x-x_0)=0
\end{aligned}\tag{5.3}$$

where A is one of the parameter values from the index of refraction model ($n(z) = A + Be^{C \cdot z}$), n and n_0 are the index of refraction at the source and the target respectively, $x - x_0$ is the horizontal distance between the source and the target, and $\sigma_0 = \sin\theta_0$ which give us the information about the launch angle θ_0 at the source location. From this equation, we find an initial launch angle at the source location that makes the left-hand-side of the equation smaller than 10^{-4}. This first semi-analytic approach is much faster than the ordinary "trial and error" method as we don't need to trace the ray step-by-step for multiple trials. If RaySolver couldn't find the solution with the first semi-analytic method, it uses a "trial and error" technique to find the solution. This second trial of ray-solution calculation insures that we don't miss any possible ray-solution from the first semi-analytic method. Once RaySolver finds a first solution, it moves on to the next possible solution which is either a U-turned (or highly bent) in-ice trace or a surface reflected trace. It uses only a traditional "trial and error" method to search for a second solution. For the first and second solutions, the minimum distance between the ray and the target should be less than the required accuracy parameter which is 0.2 m.

From RaySolver, we obtain the travel distance and time from the shower to each antenna, the polarization of the signal and the receiving angle at each antenna so that we can apply the antenna responses to the signal.

5.1.5 Ice Attenuation Factor

After the travel distance of the ray is obtained from RaySolver, AraSim applies factors to account for ice attenuation to the signal. In AraSim, there are two ice attenuation length models. The default model uses a South Pole temperature profile from [73] folded in with a relationship between field attenuation length and ice temperature given in [74] as used in ANITA simulations and described in [75]. The

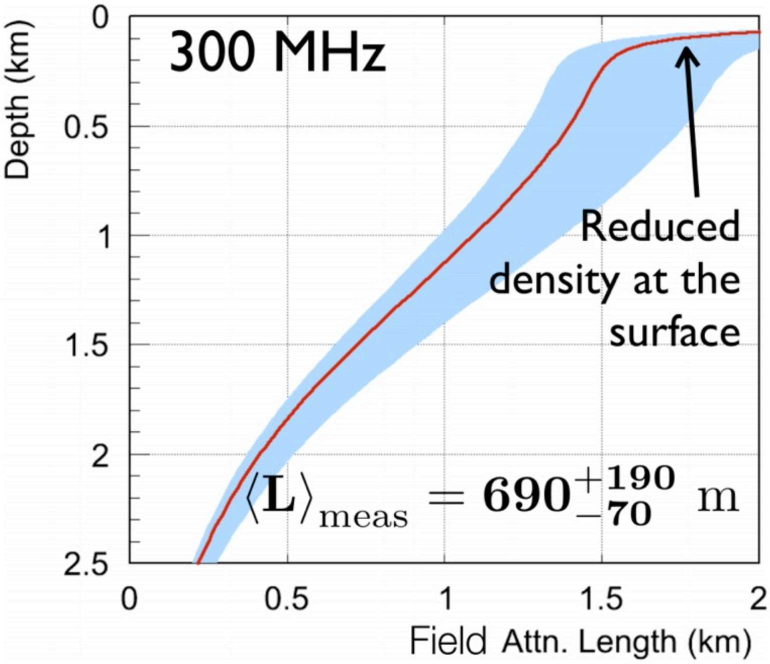

Figure 5.4: The electric field attenuation length as a function of depth from the ARA Testbed deep pulser data. The depth of the deep pulser was ~ 2 km and the path length was 3.16 km from the deep pulser to the ARA Testbed. From the single distance measurement, the average attenuation length over all depths are extrapolated.

alternative ice attenuation length model is based on the ARA Testbed measurement from IceCube deep pulser events published in [31]. The alternative model from ARA Testbed deep pulser data was measured with one depth location of the pulser which was ~ 2 km deep. From the data measured from a single distance, we deduced the ice attenuation length as a function of depth. Fig. 5.4 shows the ice attenuation length versus depth of ice with the mean value shown as a red line, while the error range shown as blue band.

The ice attenuation factor applied with no frequency dependence, using the distance along each ray-trace path through the ice and the attenuation factor to the electric field is:

$$F_{\text{IceAtten}} = e^{-D_{\text{travel}}/L_{\text{atten}}} \tag{5.4}$$

where D_{travel} is the ray travel distance from RaySolver and L_{atten} is the ice attenuation length.

5.1.6 Antenna Response

When the rays arrive at each antenna, we apply the antenna's properties to the signal. Antenna models in AraSim are obtained from NEC2 simulation software [76]. In NEC2, we can run an antenna simulation with information about a known antenna shape used in ARA. The vertically polarized antennas (Vpol) and horizontally polarized antennas (Hpol) have different shapes, and therefore different NEC2 simulations are performed. For both, we took a bandwidth from 83 MHz to ~ 1 GHz with 60 steps in frequency. The angular response was calculated in 5° steps in both azimuth and zenith angle. Both gain and phase are obtained at each frequency and angle, for each antenna. For Vpol antennas, NEC2 simulation result is obtained with the geometric information from antenna's CAD design sheet. For Hpol antennas, however, due to the difficult in modeling slotted antennas in NEC2 we have two different methods to imitate Hpol's polarization.

The first method uses a simple dipole antenna model with a similar length and thickness as the slot of the actual Hpol antenna to reproduce the slot. In order to imitate the slot, we manually swapped the electric field (E-field) and magnetic field (B-field) response from the NEC2 simulation result which makes the antenna have a horizontally polarized response.

The second method uses exactly the same gain and phase response as Vpol but again manually changes the polarization by switching the E-field and B-field responses. By default, AraSim uses the second method for the Hpol response as it is found out that the simple dipole response is too optimistic in terms of gain and phase response based on the comparison between the simulated and measured calibration pulser events. A later version of AraSim will include more realistic antenna responses by using measured antenna properties.

Once the antenna gain and phase values are obtained from the NEC2 model, the effective height of the antenna is obtained by:

$$\begin{aligned} G &= 4\pi\frac{A_{eff}}{\lambda^2} \\ h_{eff} &= 2\sqrt{A_{eff}\frac{Z_r}{Z_{air}}} \\ &= 2\sqrt{\frac{Gc^2Z_r}{4\pi f^2\cdot n^2\cdot Z_{air}/n}} \end{aligned} \tag{5.5}$$

where G is the gain of the antenna at a specific receiving angle and frequency, A_{eff} is effective area of the antenna, Z_r is antenna radiation resistance which is 50 Ω, Z_{air} is resistivity of free space which is 377 Ω, f is frequency and n is the index of refraction of the medium at the antenna. In case of impedances matched between the antenna and the load, the voltage measured by the antenna (see the schematic Fig. 5.5) is $V_{\text{ant}} = h_{eff}\cdot E_{before}$, where E_{before} is the E-field strength right in front of the antenna. In Fig. 5.5, when impedance matched, $\mathrm{Z_A}$ and $\mathrm{Z_R}$ have zero reactance, and the same resistance. When we let the resistance for both $\mathrm{Z_A}$ and $\mathrm{Z_R}$ be R_r ($\mathrm{Z_A} = \mathrm{Z_R} = \mathrm{R_r}$), the actual signal we measure (the voltage across the load R_r, which is V in Fig. 5.5)

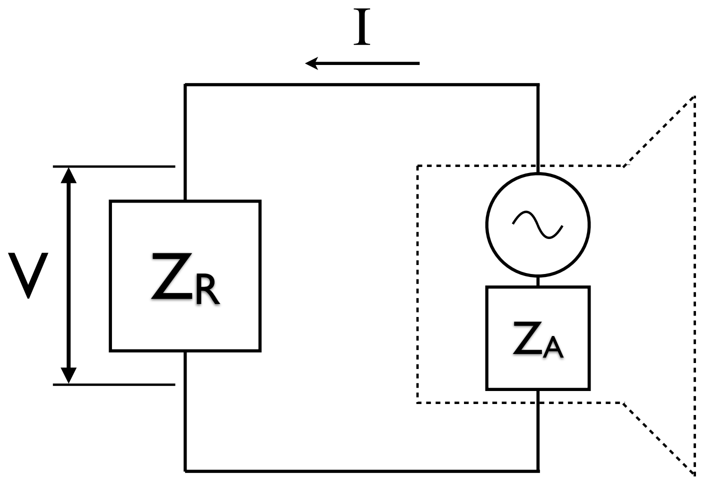

Figure 5.5: Signal receiver system's simple schematic. Right hand part (source and $\mathrm{Z_A}$) are the components from antenna while left hand part ($\mathrm{Z_R}$) is the signal receiver (such as DAQ). When impedance is matched, we can let reactance X from both $\mathrm{Z_A}$ and $\mathrm{Z_R}$ as zero and resistance for both $\mathrm{Z_R}$ and $\mathrm{Z_A}$ as the same value R_r ($\mathrm{Z_A} = \mathrm{Z_R} = \mathrm{R_r}$). V on the plot is the actual measured voltage signal which is $V = \mathrm{Z_R} \cdot \mathrm{I} = \mathrm{V_{measured}}$.

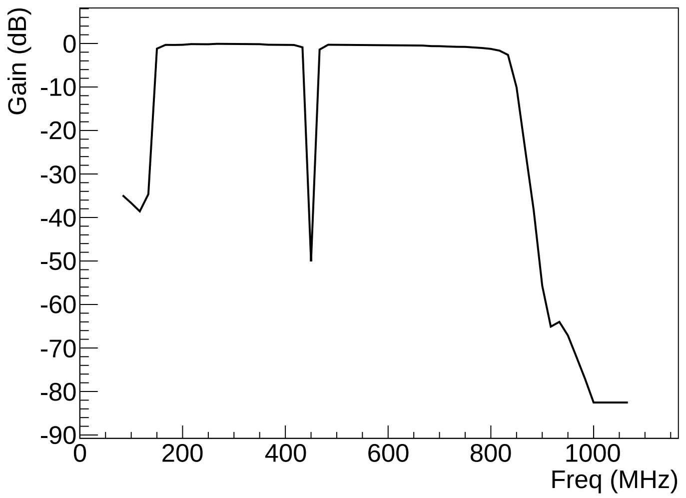

Figure 5.6: Filter's gain response which is in use for AraSim. The filter response consists of a high pass filter at 150 MHz, a low pass filter at 800 MHz, and a notch at 450 MHz to avoid the electronics communication frequency.

is then:

$$\begin{aligned} V_{measured} &= I \cdot R_r \\ &= \left(\frac{V_{\text{ant}}}{2R_r}\right) \cdot R_r \\ &= \frac{1}{2} E_{before} \cdot h_{eff} \end{aligned} \tag{5.6}$$

where I is the current through the circuit and $V_{measured}$ is the voltage we can actually measure over the load R_r.

5.1.7 Electronics Response

After the antenna, neutrino signals will pass through entire electronics chain such as a low noise amplifier (LNA), filter and fiber optic amplifier module (FOAM). The measured filter gain response which AraSim uses is shown in Fig. 5.6 as an example.

The phase response is derived from a Qucs Studio [77] model of filters with similar characteristics. Other components in the electronics chain (LNA and FOAM) do not have strong phase responses, so we only applied the gain response of them which is simply a multiply of gain to the signal spectrum. Once the received signal is convolved with the detector response, noise is added to the signal.

5.1.8 Generating Noise Waveforms

If any ray trace solution exists for a specific neutrino event, AraSim generates noise waveforms for each channel. Channel numbers shown in this chapter are introduced in Table 4.1. There are two thermal noise waveform generation models in Arasim, the nominal non-calibrated thermal noise model and calibrated thermal noise model. The nominal noise model is used as a first order estimation of the noise in AraSim while an accurately calibrated noise model is applied for all of the data analyses in this paper. A detailed explanation of how the noise model is calibrated can be found in Section 5.3.1.

The nominal noise model in AraSim starts with Johnson-Nyquist theory. From [78], one-sided (or single-sided) frequency band mean square noise voltage due to thermal noise from a open circuit is given as:

$$< V^2 >= 4 \cdot k_B \cdot T \cdot R_L \cdot \mathrm{BW} \tag{5.7}$$

where BW is the bandwidth (only one sided bandwidth, meaning bandwidth in only positive frequencies), R_L is the resistance of the load, T is the temperature, and k_B is the Boltzmann constant.

Now, with the open circuit consisting of a antenna and a load, mean voltage in Eq. 5.7, we can calculate the measured voltage in our system. In Fig.5.7, Z_A is the

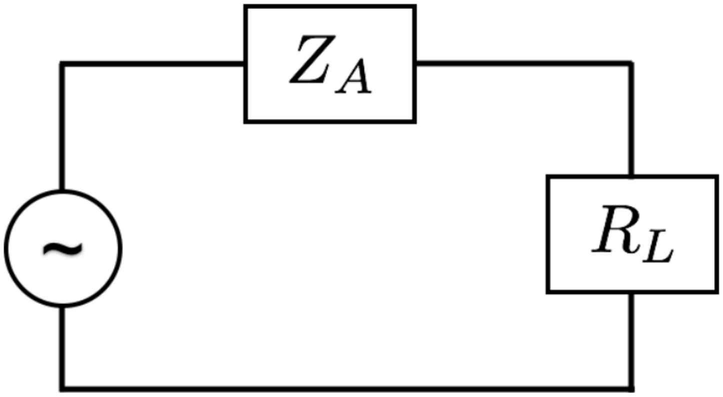

Figure 5.7: Simple closed circuit with voltage source (thermal noise source) and antenna (Z_A) and load (R_L).

antenna internal impedance, and R_L is the load resistance. In the case when the impedance is matched, the inductance of Z_A is zero ($X_A = 0$), and the resistance of both antenna and the load are same ($R_A = R_L$). Then the measured mean power is:

$$P = I^2 \cdot R_L = \frac{V^2 \cdot R_L}{(R_A + R_L)^2} = \frac{V^2}{4 \cdot R_L} \tag{5.8}$$

$$< P >= \frac{< V^2 >}{4 \cdot R_L} = k_B \cdot T \cdot \text{BW}. \tag{5.9}$$

Therefore, in order to get the result in Eq. 5.9, mean power spectral density value inside the bandwidth should be $k_B \cdot T$ in W/Hz.

Our default temperature value in AraSim is 325 K, found by assuming a 230 K average environmental temperature and a 95 K noise temperature for the low noise amplifier (LNA). From this perfectly flat noise spectrum, AraSim applies the band pass filter response to limit the bandwidth of the system to approximately 150 −

850 MHz (shown in Fig. 5.6). From the power spectrum that we produce, we apply a $0-2\pi$ random phase to each frequency bin and then obtain the time domain thermal noise waveform by taking the Fourier Transform.

Generated noise waveforms are required to have a long enough time length in order to add all time domain neutrino signals with proper time delay between channels. AraSim typically produce a ~ 6 μs noise waveform to encompass the arrival times for all ray solutions. The time-domain signal waveform is added to this noise waveform at its arrival time at the antenna from the ray tracing.

5.1.9 Trigger Analysis

Once the noise has been added from the previous step, the signal is split into the trigger and digitization paths. For the trigger path, the time-domain signal is convolved with a model of the tunnel diode power integrator which integrates the input waveform power over $\sim$ 10 ns (Section 4.1). This convolved time-domain response is then scanned for excursions above the power threshold. For the Testbed simulation, the power thresholds were calibrated against RF triggered events for each antenna as described in Section 5.3.2. When the trigger finds 3 such excursions among the 8 borehole antennas within a 110 ns window, the event is considered to have triggered. Once the trigger condition is met, waveforms are read out in 256 ns waveforms just like the data, and written into the same format as the data so that the simulated events can be analyzed with identical software.

5.2 Askaryan Radiation in AraSim

The contents of this section are in progress to be published.

In this section, two models for generating Askaryan signals in AraSim are described. The default mode in AraSim is one that produces a custom parameterized RF Cherenkov emission for each event. This technique was developed based on an approach suggested by [12,79]. This mode will generate the radiated signal with proper phase information for corresponding frequencies. The second alternative mode is based on the Alvarez-Muñiz, Vàzquez and Zas (AVZ) model [80]. This second mode is the signal generation mode from icemc, a ANITA simulation software. In this mode, Askaryan signals are calculated with a simple 90° phase assumption which makes an ideal impulsive waveform without dispersion.

5.2.1 Custom parameterized RF Cherenkov emission model

Approach of Alvarez-Muñiz, et. al. In Alvarez-Muñiz, *et. al.* [12], the authors suggest to generate Askaryan signals using a semi-analytic method which can maintain outcomes that agree well with results from a full shower simulation without adding too much computational time. The semi-analytic method consists of two separate steps for each event.

1. Generate 1D shower profiles from a full shower simulation
2. Use generated shower profiles to calculate Askaryan signals using analytic functions

In the first step, one obtains the shower profiles, which describe the charge excess as a function of shower depth. Alvarez-Muñiz, *et. al.* suggest to generate shower profiles using the ZHAireS shower simulation software which is the ZHS software modified to simulate showers in various media including ice [81]. Shower profiles for electromagnetic and hadronic showers are obtained separately as they have different properties. Obtaining the 1D shower profile for a shower is relatively quick and cheap

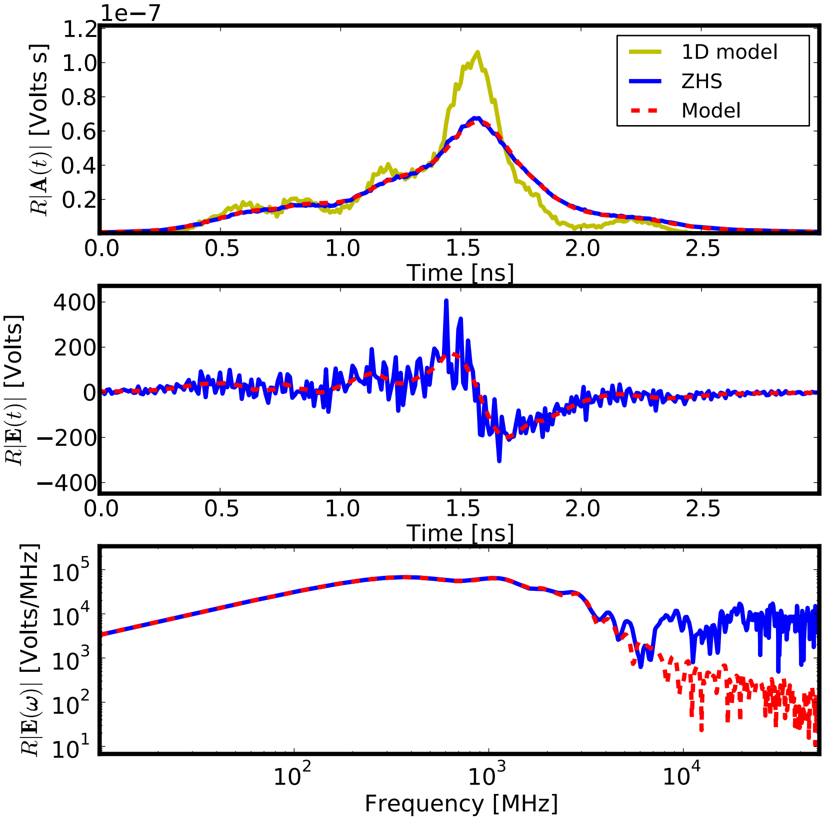

Figure 5.8: Comparison between the full shower simulation (ZHS) and the semi-analytic model of a 3×10^{18} eV electromagnetic shower at a viewing angle of $\theta = \theta_C - 0.3°$. The blue solid curve shows the result from ZHS full shower simulation, the red dashed curve shows the result from semi-analytic model, and the yellow solid curve shows the result from simple 1D model. The top plot shows the vector potential $R|\mathbf{A}|$ in the time domain, the middle plot shows the electric field $R|\mathbf{E}|$ in the time domain, and the bottom plot shows the spectrum in the frequency domain. All three plots show that the full ZHS simulation and the semi-analytic method agree well. The disagreement at the high frequencies seen in the middle and bottom plots are not important for ARA as the bandwidth of the system only goes up to 1 GHz. Plots from [12].

in computational time compared with the full shower simulation that calculates the emitted electric field.

The Askaryan signals are calculated in the second step. The vector potential from the shower is obtained from the parameterized Green's function solutions to Maxwell's equations. These analytic functions have form factor equations which are fitted to the profiles from the full shower simulation for electromagnetic and hadronic shower separately, for different media.

The vector potential equation under a far field assumption with a parameterized form factor F_p from [12] is:

$$\vec{\mathbf{A}}(\theta,t)=\frac{\mu}{4\pi R}\sin\theta\cdot\hat{\mathbf{p}}\int_{-\infty}^{\infty}dz'Q(z')\cdot F_p\left(t-\frac{nR}{c}-z'\left[\frac{1}{v}-\frac{n\cos\theta}{c}\right]\right)\tag{5.10}$$

where μ is the permeability of the medium, R is the distance between the shower and the receiver, $\hat{\mathbf{p}}$ is the unit vector pointing along the direction of vector potential, z' is the shower depth in meters, $Q(z')$ is the shower charge excess as a function of depth (Eq. 5.17), n is the index of refraction of the media, c is speed of light, v is the shower propagation velocity, and θ is the angle between the shower axis and the RF signal propagation direction (viewing angle). The form factor F_p is a key term in Eq. 5.10 which determines the shape of the radiated signal. The form factor F_p equation at the Cherenkov angle is obtained by fitting to the vector potential at the Cherenkov angle to the ZHS full shower simulation. For the case of an electromagnetic shower in ice, the form factor equation at the Cherenkov angle [12] is:

$$F_p\left(t-\frac{nR}{c}\right)=\frac{4\pi}{\mu}\frac{1}{LQ_{total}}\frac{1}{\sin\theta_C}\times -4.5\times 10^{-14}\frac{E}{\text{TeV}}$$
$$\begin{cases}\exp\left(-\frac{|t|}{0.057}\right)+(1+2.87|t|)^{-3}, & \text{if } t\geq 0\\ \exp\left(-\frac{|t|}{0.030}\right)+(1+3.05|t|)^{-3.5}, & \text{if } t<0\end{cases} \tag{5.11}$$

where LQ_{total} is integrated shower charge excess ($LQ_{total}=\int dz'Q(z')$), θ_C is the Cherenkov angle, E is the energy of the shower, R is the distance between the shower and the observer, and t is the time at the observer frame. The time t is defined that $t=0$ is when the observer is at a viewing angle of θ_C and a distance of R, receives the peak vector potential from the shower. For a hadronic shower in ice, the form factor equation is:

$$F_p\left(t-\frac{nR}{c}\right)=\frac{4\pi}{\mu}\frac{1}{LQ_{total}}\frac{1}{\sin\theta_C}\times -3.2\times 10^{-14}\frac{E}{\text{TeV}}$$
$$\begin{cases}\exp\left(-\frac{|t|}{0.043}\right)+(1+2.92|t|)^{-3.21}, & \text{if } t\geq 0\\ \exp\left(-\frac{|t|}{0.065}\right)+(1+3.0|t|)^{-2.65}, & \text{if } t<0.\end{cases} \tag{5.12}$$

With the far field assumption, the equation for the vector potential becomes Eq. 5.10 with either Eq. 5.11 or 5.12 being substituted for F_p with a proper time offset term accounting for the viewing angle ($z'[1/\nu - n\cos\theta/c]$ in Eq. 5.10).

After inserting the form factor equations, the electric field as a function of time is the time derivative of the vector potential. This method uses a 1D approximation of the shower profile but yields consistent results with the full 3D shower simulation (Fig. 5.8, [79]). Fig. 5.8 shows the comparison between ZHS [82] full shower simulation result and the semi-analytic model result. They agree well between each other up to few GHz range which is fine for ARA's 200 MHz to 850 MHz bandwidth.

Customized Approach in AraSim The default mode for generating Askaryan signals in AraSim uses a custom parameterized RF Cherenkov model which is a modified approach from the method suggested by Alvarez-Muñiz, *et. al.* [79] in order to reduce the computational time even more. Generating a shower profile from a full shower simulation software takes ∼hour while our custom parameterized RF Cherenkov model takes ∼second to calculate the RF signal. Among the two steps described in the beginning of Section 5.2.1, the first step, the full shower simulation, has been replaced by parameterized shower profile functions. The Greisen function [83] and Gaisser-Hillas function [84] are used to produce electromagnetic and hadronic shower profiles [85], respectively. The next step, calculating Askaryan signals using analytic functions, is the same. AraSim, however, has a custom time binning method to optimize the computational time of the second process, which is described in the next paragraph. This alternative method is a quick and easy way to produce a first order estimation of the shower profiles.

Detailed Description of the AraSim Custom Parameterized RF Cherenkov Model Our custom parameterized RF Cherenkov model calculates shower profiles from parameterized functions. For the electromagnetic shower, we chose the Greisen function [83] with proper parameter values for in-ice radiation. The Greisen function used in AraSim gives us the total number of electrons and positrons:

$$N_{\mathrm{total}}(X) = \frac{0.31}{\sqrt{\ln{(E_0/E_c)}}} \cdot e^{X-1.5X\ln{((3X)/(X+2\ln{(E_0/E_c)}))}} \tag{5.13}$$

where N_{total} is total number of electrons and positrons, E_c is a critical energy, 0.073 GeV in ice, E_0 is the energy of the shower in GeV, and X is shower depth in units of radiation length. Fractional excess of electrons (ΔN) is given by:

$$\Delta N = \frac{N(e^-) - N(e^+)}{N(e^-) + N(e^+)} \sim 0.25 \tag{5.14}$$

and the number of excess electrons (N_{excess}) is:

$$N_{\text{excess}} = N_{\text{total}} \cdot \Delta N \tag{5.15}$$

Based on the ZHS in-ice shower simulation (Fig. 5.9), a constant 25% fractional excess of electrons in the shower is chosen.

For hadronic showers, a Gaisser-Hillas function [84] is used to obtain shower profiles. As for the electromagnetic shower case, parameter values for the Gaisser-Hillas function are chosen for in-ice radiation:

$$N_{\text{total}}(X) = S_0 \cdot \frac{E_0}{E_c} \cdot \frac{X_{max} - \lambda}{X_{max}} \cdot e^{(X_{max}/\lambda - 1)} \left(\frac{X}{X_{max} - \lambda} \right)^{X_{max}/\lambda} \cdot e^{(-X/\lambda)} \tag{5.16}$$

where S_0 is 0.11842, λ is 113.03 g/cm^2, X_0 is 39.562 g/cm^2, E_c is 0.17006 GeV, E_0 is the energy of the shower in GeV, and X is shower depth in g/cm^2. As for the electromagnetic shower case, we use a constant 25% charge excess over the entire shower. For both electromagnetic and hadronic showers, the charge excess is then:

$$Q(X) = q \cdot N_{\text{excess}}. \tag{5.17}$$

where q is an electric charge of an electron.

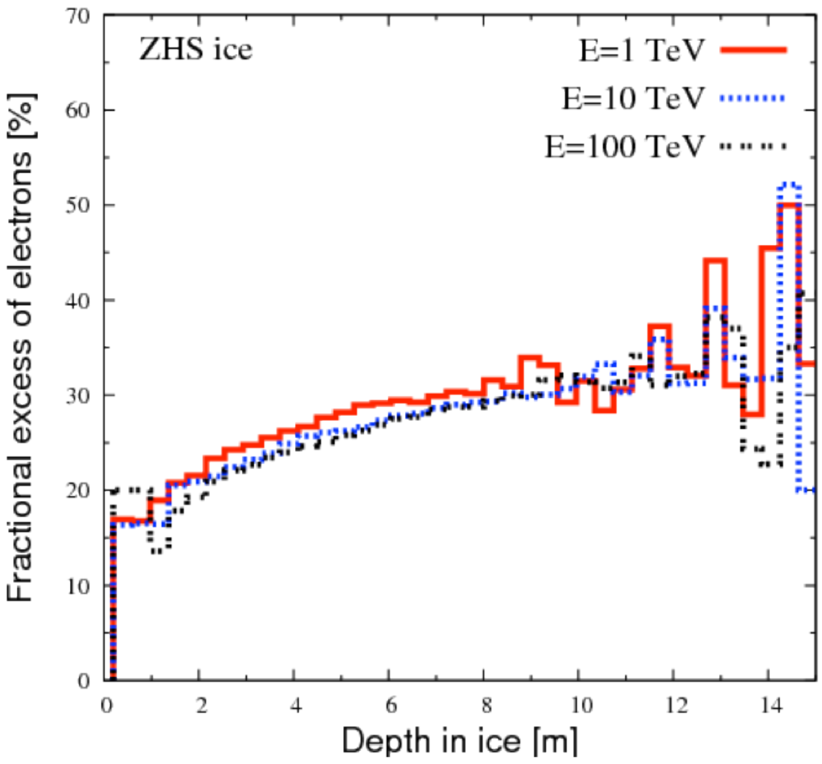

Figure 5.9: Fractional excess of electrons from ZHS in-ice simulation. Horizontal axis shows the shower depth in ice. The plot shows that fractional excess of electrons varies from 20% at the beginning of a shower to 30% for larger depths regardless of the energy of the shower. Based on this plot, constant 25% excess of electrons is chosen.

We defined a bin size in time for calculating the vector potential in Eq. 5.10 to obtain proper length of the signal with 64 bins. This constant number of bins give us a constant computation time to calculate the signal. In Eq. 5.10, we must integrate the right-hand-side of the equation over the length of the shower for each time bin t_i. The time duration of the signal change as a function of the viewing angle θ [79] and in order to include entire signal waveform in constant 64 bins, we change the size of the time bin as a function of the viewing angle (in Eq. 5.19). While the duration of the signal is minimal when the viewing angle is at the Cherenkov angle, $\theta = \theta_C$, the signal gets stretched in time when the viewing angle is further away from the Cherenkov angle. This is due to the fact that all signals radiated from charged particles in the shower arrive at the receiver at the same time when the receiver is located right at the Cherenkov angle relative to the shower axis. We define a factor that is a measure of how off the Cherenkov angle the observer sits:

$$f_{\text{offcone}} \equiv 1 - n \cdot \cos\theta. \tag{5.18}$$

And using this factor, we define the total duration of the signal:

$$T_{\text{total}} = |f_{\text{offcone}}| \cdot T_{\text{shower}} \cdot A_0 + 2 \text{ ns} \tag{5.19}$$

where T_{shower} is the total travel time of the shower in the medium in ns, and A_0 is a constant parameter value which changes the total length of the signal. The A_0 value is chosen such that T_{total} at $\theta = \theta_C \pm 10^\circ$ give us a long enough length of time to include the entire signal ($A_0 = 1.2$). If the receiver is located at the Cherenkov angle relative to the shower axis, then f_{offcone} becomes zero and T_{total} will be 2 ns. We calculate the RF Cherenkov signal with 64 time bins for all cases. Therefore, the time domain bin size is:

$$\Delta t = T_{\text{total}}/64. \tag{5.20}$$

Our custom parameterized RF Cherenkov emission mode in AraSim shows consistent results with results from the ZHS simulation. Fig. 5.10 shows a shower profile for a 1 PeV electromagnetic shower from AraSim and ZHS simulation. Since it is an electromagnetic shower, AraSim uses a Greisen function (Eq. 5.13) to generate the shower profile. From the shower profile, AraSim calculates the vector potential (Fig. 5.11). From the time derivative of the vector potential ($\vec{\mathbf{E}} = -\partial\vec{\mathbf{A}}/\partial t$), the electric field is obtained in Fig. 5.12. Again, the plot shows the result from AraSim and the ZHS simulation which agree well with each other. This example shows that our custom parameterized RF Cherenkov emission mode in AraSim generates the RF signal which agree well with ZHS full shower simulation.

This custom parameterized RF Cherenkov emission model produces the electric field in the time-domain directly from a custom shower profile. This way, we have improved phase information for each signal compared to the former RF emission model (Section 5.2.2).

Limitations of Custom Parameterized RF Emission Model One drawback of the current version of this method is that we cannot account for the Landau-Pomeranchuk-Migdal (LPM) effect [86,87] in the shower as we use the parameterized shower profile functions.

The LPM effect becomes significant when the energy of the particle in the shower is larger than the LPM threshold energy ($E_{\text{LPM}} = 2 \times 10^{15}$ eV in ice). Then, the Bethe-Heitler radiation length and the mean free path for the pair production become comparable. This means there is an interference between a radiated photon and

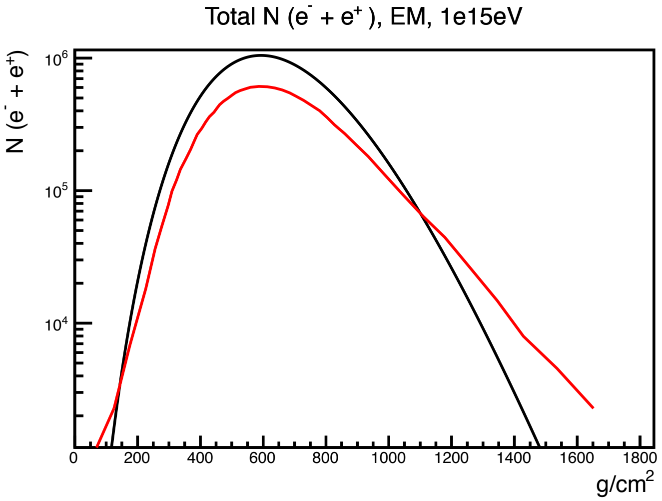

Figure 5.10: Shower profiles from AraSim and ZHS simulation for 1 PeV electromagnetic shower. The black curve is obtained from AraSim using Greisen function (Eq. 5.13), and the red curve is obtained from [13] Fig. 3 which is the result from the ZHS simulation.

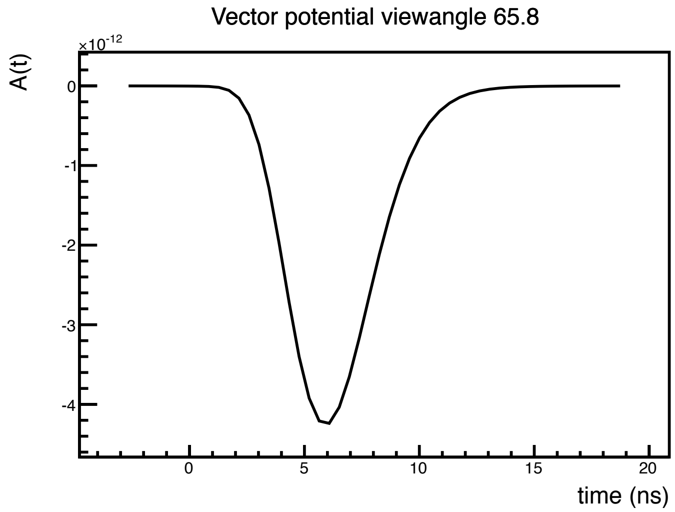

Figure 5.11: Vector potential obtained from AraSim for the same shower shown in Fig. 5.10. Here, the vector potential is calculated 1 m from the shower. Viewing angle is $\theta = \theta_C + 10° = 65.8°$.

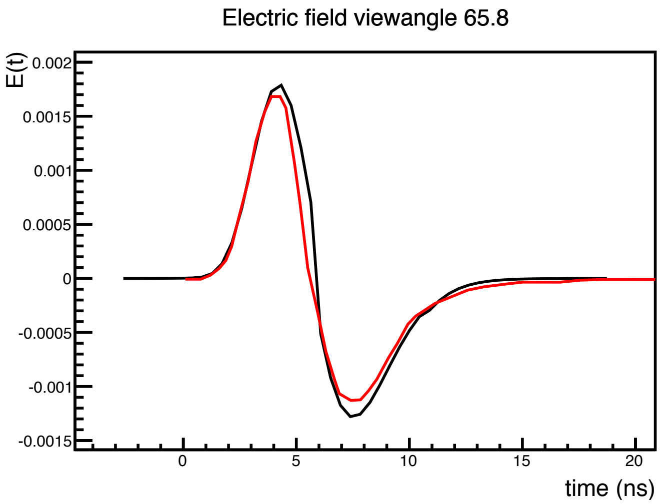

Figure 5.12: Electric field in the time domain from AraSim compared to ZHS simulation for the same shower as shown in Fig. 5.10 and 5.11. The black curve is obtained from AraSim, and the red curve is obtained from [13] Fig. 3 which is the result from ZHS simulation. Even though there was some disagreement in the shower profile (Fig. 5.10), the overall electric field signal power don't differ by more than 25%.

a subsequent interaction (or in other words, interference between Bremsstrahlung interaction and pair production). This interference increases the interaction length in the shower.

We will revise the method in order to account for the LPM effect in the future. One quick-and-dirty way to account the LPM effects is to simply stretch the shower profile by factor of:

$$F(E_0) = \left(\frac{E_{\rm LPM}}{0.14 \cdot E_0 + E_{\rm LPM}} \right)^{0.3} \tag{5.21}$$

where $E_{\rm LPM}$ is the LPM effect threshold energy which is 2 PeV for ice, and E_0 is the energy of the shower [88]. When we stretch the shower profile by $F(E_0)$, we have to conserve the total number of produced particles in the shower ($LQ_{total} = \int dz' Q(z')$).

Therefore, we have to apply a factor $1/F(E_0)$ to the shower charge excess:

$$Q'(z') = Q(z') \cdot \frac{1}{F(E_0)}. \tag{5.22}$$

Another method which is more sophisticated is to use shower profile, that are generated from a shower simulation that includes the LPM effect. In order to reduce the computation time of the simulation, we can first generate a library of shower profiles for different shower energies using a shower simulation such as ZHAireS. While running the AraSim simulation, we can choose one of the shower profiles from the library for the corresponding shower energy. These improvements will be added to AraSim as a separate simulation mode in near future. For now, we found the amount that the sensitivity changed due to the LPM effect using the old parameterized AVZ model (Section 5.2.2) turned on and off. We accounted the same factor to the sensitivity obtained using our custom parameterized RF Cherenkov emission mode.

5.2.2 Parameterized AVZ RF Cherenkov emission model

The second mode for generating Askaryan signals in AraSim is based on the fully parameterized RF Cherenkov emission model by Alvarez-Muñiz, Vãzquez and Zas (AVZ model) [80]. While the default Cherenkov emission model in AraSim (Section 5.2.1) produces the electric field with improved phase information, the second mode calculates the electric field with a trivial 90° phase in positive frequencies and −90° phase in negative frequencies. From the AVZ model, which is a fully parameterized model of the frequency spectrum using a 1D approximation of the shower, the electric field spectrum at the Cherenkov angle is:

$$R|\vec{\mathbf{E}}(\omega, R, \theta_C)| \simeq \frac{1}{2} \times 2.53 \times 10^{-7} \left[\frac{E_0}{\mathrm{TeV}}\right] \left[\frac{\nu}{\nu_0}\right] \left[\frac{1}{1 + (\nu/\nu_0)^{1.44}}\right] \tag{5.23}$$

where $\nu_0 = 1.15\ GHz$, E_0 is the energy of the shower, and the unit of the equation is V/MHz. The very first 1/2 factor is added to the original Eq. 5 in [80]. This is due to the fact that the AVZ model is based on the ZHS model [82] which uses an unconventional Fourier transform equation (Eq. 8 in [82] contains a factor of 2 compared to the conventional Fourier transform equation:

$$\vec{\mathbf{E}}(\omega, \vec{\mathbf{x}}) = 2 \int dt e^{i\omega t} \vec{\mathbf{E}}(t, \vec{\mathbf{x}}) \tag{5.24}$$

while Fourier transforms in AraSim follows conventional transform:

$$\vec{\mathbf{E}}(\omega, \vec{\mathbf{x}}) = \int dt e^{i\omega t} \vec{\mathbf{E}}(t, \vec{\mathbf{x}}). \tag{5.25}$$

Also, one point to note is that both [80] and [82] calculate a double-sided electric field spectrum, which means even if there is only a spectrum for positive frequencies shown in the plots, there is the same amount of power in the negative frequencies. As the Fourier transform in AraSim assumes a double-sided spectrum, there is no additional factor needed to account double-sided spectrum in Eq. 5.23.

In this model, the electric field spectrum at a viewing angle away from the Cherenkov angle is obtained by applying a parameterized factor. This factor depends on the width of the Cherenkov cone, which depends on the length of the shower. The longer the length of the shower, the narrower the width of the Cherenkov cone become.

The width of the Cherenkov cone for the electromagnetic shower [88] in AraSim is:

$$\Delta\theta_{\text{em}}(\nu) = 2.7 \cdot \frac{\nu_0}{\nu} \left(\frac{E_{\text{LPM}}}{0.14 E_\nu + E_{\text{LPM}}} \right)^{0.3} \tag{5.26}$$

where $\nu_0 = 1.15\ GHz$, E_{LPM} is the LPM effect threshold energy which is 2 PeV for ice, and E_ν is the energy of the electromagnetic shower. Eq. 5.26 above shows that the width of the Cherenkov cone depends on the LPM threshold energy. Since the LPM effect shows up predominantly in electromagnetic showers, AraSim only accounts for this lengthening effect in electromagnetic showers.

The width of the Cherenkov cone for hadronic showers is parameterized for different shower energies in [89]. The angular width of the Cherenkov cone is:

$$\Delta\theta_{\mathrm{had}} = \begin{cases} \frac{\nu_0}{\nu}(2.07 - 0.33\epsilon + 0.075\epsilon^2), & \text{if } 0 \leq \epsilon < 2 \\ \frac{\nu_0}{\nu}(1.744 - 0.0121\epsilon), & \text{if } 2 \leq \epsilon < 5 \\ \frac{\nu_0}{\nu}(4.23 - 0.785\epsilon + 0.055\epsilon^2), & \text{if } 5 \leq \epsilon < 7 \\ \frac{\nu_0}{\nu}(4.23 - 0.785 \times 7 + 0.055 \times 7^2) & \\ \times[1.0 + (\epsilon - 7.0) \times 0.075], & \text{if } \epsilon \geq 7 \end{cases} \tag{5.27}$$

where $\epsilon = \log_{10} E_\nu/\mathrm{TeV}$.

The electric field at a viewing angle θ depends on the signal strength at the Cherenkov angle θ_C and the width of the Cherenkov cone $\Delta\theta$ [88, 89]. The equation is:

$$E(\theta) = \frac{\sin\theta}{\sin\theta_C} E(\theta_C) \cdot \exp\left[-\left(\frac{\theta - \theta_C}{\Delta\theta_{\mathrm{em,had}}}\right)^2\right] \tag{5.28}$$

where the signal strength at the Cherenkov cone, $E(\theta_C)$, is from Eq. 5.23, and the width of the Cherenkov cone for electromagnetic and hadronic showers are given at Eq. 5.26 and 5.27, respectively.

The default custom parameterized RF emission model and the AVZ RF emission model show results comparable with each other. Fig. 5.13 shows an example spectrum

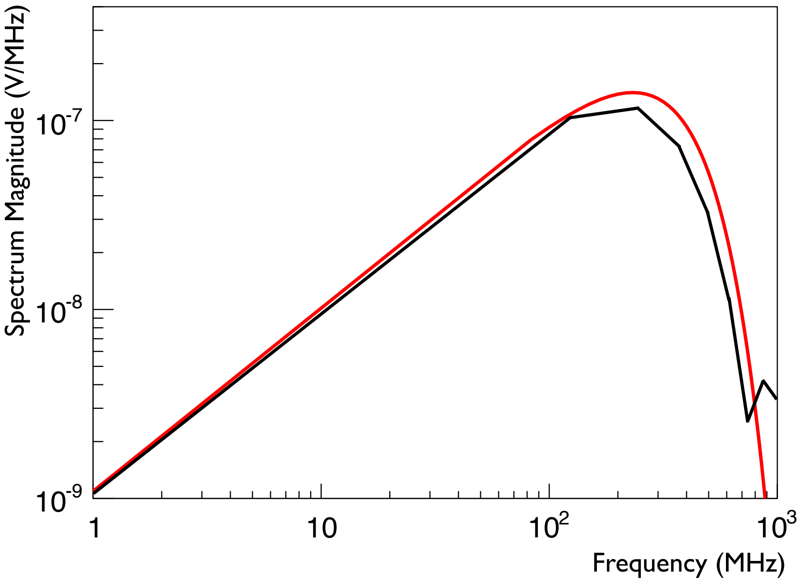

Figure 5.13: Comparison of spectra obtained from the two Cherenkov emission modes in AraSim. The red curve is obtained from the AVZ RF model and the black curve is the result from custom parameterized RF Cherenkov model (Section 5.2.1). Both results have exactly same shower parameters (electromagnetic shower with 10 TeV energy and viewing angle of $\theta = \theta_C - 5°$). The two RF signal emission models show consistent results.

from the two models with the same shower parameters. Overall the maximum electric field signal difference between the two modes for various shower conditions we tested was 70% where as for most cases the difference was $\sim$ 40%. Considering that the two models use a significantly different approach, we think the difference between two models is reasonable. For the analysis presented in this paper, we use the first custom parameterized RF Cherenkov model as a default model while we considered the AVZ emission model with a simple model for the detector phase response to estimate a systematic error in Section 6.6.

5.3 Calibrating AraSim to the Testbed Data

Calibrating the simulation to data is very important as we are modeling our sensitivity to neutrinos with our simulation. Here we will show how we calibrated thermal noise waveforms and trigger thresholds.

5.3.1 Calibrating Thermal Noise

Thermal noise events dominate the triggered background events from the ARA detector. Therefore, calibrating our thermal noise model to measured data is essential. There are multiple steps for calibrating thermal noise which are going to be explained in following paragraphs.

Thermal Sample We first have to select events that are minimally contaminated by anthropogenic noise. The software trigger causes an event to be recorded every second to monitor the RF background. While there is a chance that an event was triggered by both the software trigger and RF triggers, we selected events that are only triggered by the software trigger in order to avoid contamination from anthropogenic backgrounds such as continuous wave (CW) and impulsive signals.

Make Waveforms have Consistent Binning As the thermal noise calibration will be done for each frequency bin separately, it is crucial to make each channel and event have the same binning in the frequency domain. From the collected software triggered sample, we make the waveforms in all channels and events have the same number of bins and bin size in time. Due to the limitation in the Testbed DAQ, the number of bins of the waveform varies $\sim \pm 10$ between events and bin size is not constant. This can be achieved by making time domain waveforms with the same number of bins and the same bin size. We force the waveforms to have the same number of bins by zero-padding them. We made all waveforms have 1024 bins by filling up the first

$\sim$512 bins with the original waveform data and setting the rest of the bins to zero. After that, we make the zero-padded waveform to have a constant 0.5 ns bin size by interpolating. We use the interpolation function in the ROOT software with the "AKIMA" option, which uses a continuously differentiable sub-spline interpolation function.

Make Frequency Domain Spectrum Using the waveforms that are processed up to the previous step, we produce the frequency domain spectrum from the time domain waveform using a Fast Fourier Transform (FFT). As all channels and events have the same time binning, the frequency domain spectrum will also have the same binning between channels and events.

Fit Normalized Plots with Rayleigh Distribution Function We fit the normalized distribution plot with the Rayleigh probability density function:

$$f(x;\sigma)_{freq,ch} = \frac{x}{\sigma^2} e^{-x^2/(2\sigma^2)} \tag{5.29}$$

where x is the voltage at specific frequency ($freq$), channel (ch) and σ is the only fit parameter value which is called the scale parameter. We obtained the fit parameter σ for all channels and frequency bins separately. We apply a normalization factor to each plot such that

$$\int_0^\infty f(x;\sigma)_{freq,ch} dx = 1. \tag{5.30}$$

The normalization is done by multiplying by a normalization factor:

$$N = \frac{1}{\sum_i n_i \cdot \Delta_{\text{bin}}} \tag{5.31}$$

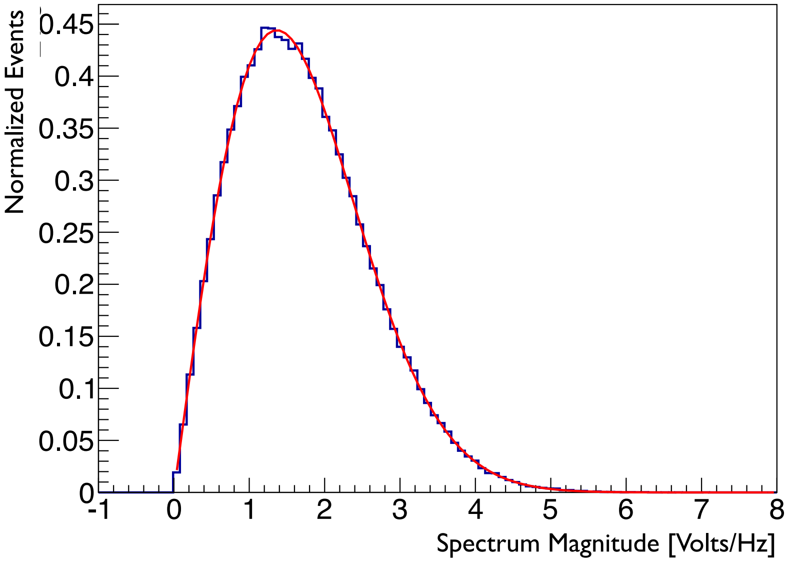

Figure 5.14: Distribution of voltages at 200 MHz and its best-fit Rayleigh distribution function. Thermal noise events from Testbed data set (software triggered events, blue curve) and their best-fit Rayleigh distribution function (red curve) are shown. The voltage distribution at 200 MHz, Channel 2 (Vpol antenna) is chosen for the plot and the integral is normalized to 1 in order of have same normalization for the Rayleigh distribution function (Eq. 5.29). Good agreement between the distribution and the fit function is shown on the plot.

where N is the normalization factor, n_i is the number of events in i^{th} bin, and Δ_{bin} is the bin size of the distribution plot. Fig. 5.14 shows a example of the voltage distribution and its Rayleigh distribution fit result for Channel 2 at 200 MHz (Channel 2 shown in Table 4.1).

Generate Thermal Noise Waveforms We use the fit results to generate thermal noise waveforms. A noise waveform for a channel is generated by selecting a voltage for each frequency bin from the fitted Rayleigh probability density function. Each frequency bin has a random phase chosen between 0 and 2π. Figs. 5.15 and 5.16 show the comparison between simulated thermal noise waveforms and the waveforms

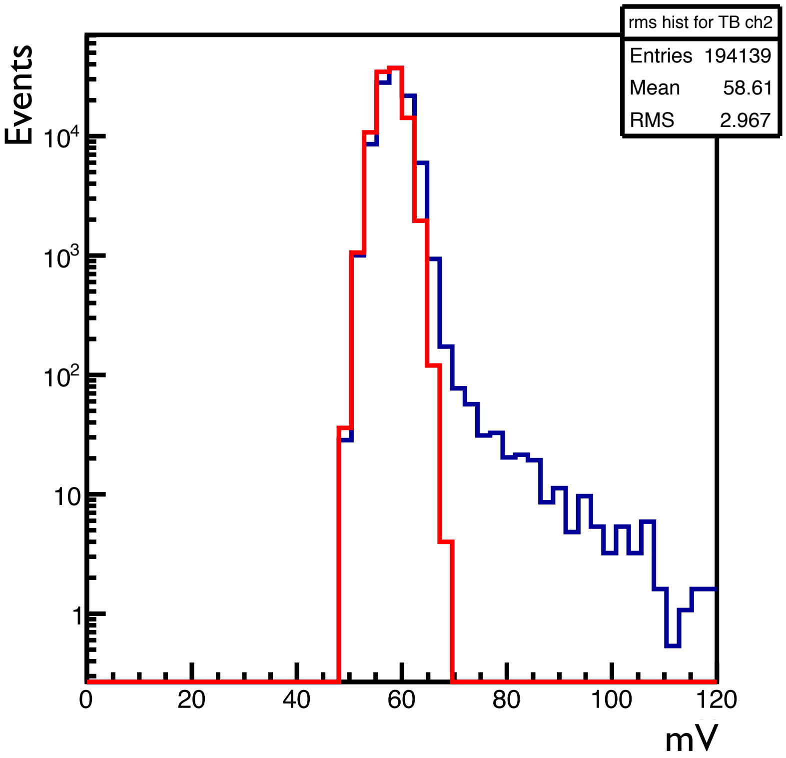

Figure 5.15: Plot of the RMS voltage distribution from generated thermal noise waveform using the best-fit Rayleigh distribution. The red curve is the distribution from generated thermal noise waveforms, while the blue curve is from Testbed data. In the Testbed data set (blue curve), there is an extended tail feature which the simulated noise doesn't have. This tail is coming from non-thermal background events such as CW and anthropogenic impulsive events. Overall, the dominant thermal noise part is well match between the data and the simulation.

from Testbed software-triggered events. Both plots show that the thermal noise part of the distribution (lower voltages) agree well between each other, while the Testbed data has extra non-thermal anthropogenic background events, which make up the extended tail on the plot. Those non-thermal backgrounds are not reproducible with the fitted Rayleigh distribution as only the pure thermal noise will follow the Rayleigh distribution.

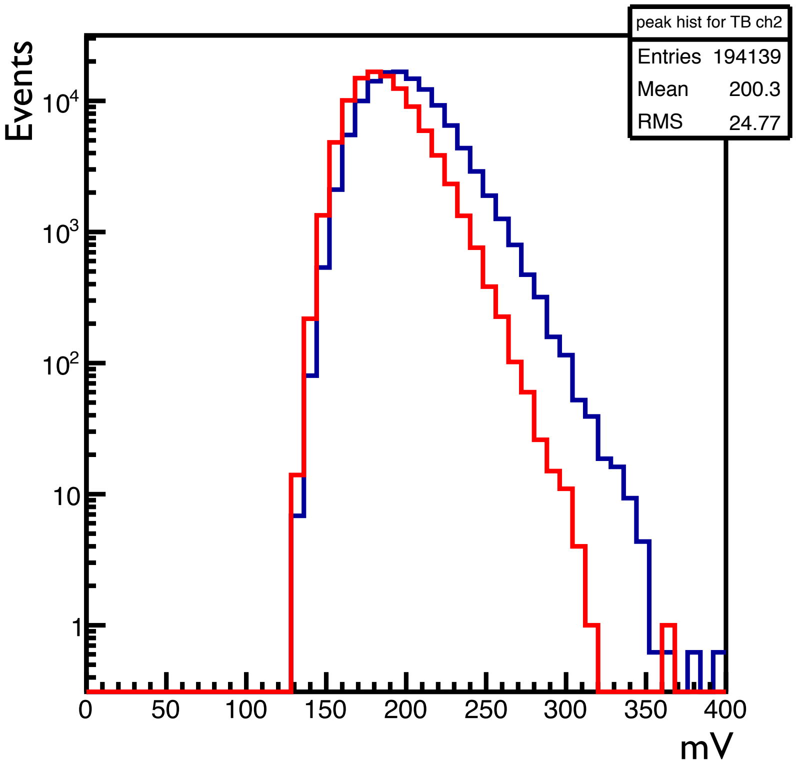

Figure 5.16: Plot of the distribution of peak voltages from thermal noise waveforms generated using the best-fit Rayleigh distribution and Testbed data. The red curve is the distribution from the generated thermal noise waveforms, while the blue curve is from the Testbed data. The part of the distribution at low voltages shows agreement between simulated noise and the data. Like the RMS distribution (Fig. 5.15), the extended tail feature in the data set is due to non-thermal background events such as CW and anthropogenic impulsive events.

5.3.2 Calibrating the Trigger Threshold

The trigger threshold is directly related to our sensitivity to neutrinos. The best situation to calibrate the trigger level in the simulation would be one where the actual hardware trigger level is well understood which is not the case for the Testbed. Therefore we had to find the variable the most sensitive to the trigger threshold and use it to calibrate the simulation.

Our calibration procedure relies on two properties of the trigger in the Testbed. First, a tunnel diode is used in the detector which means the trigger is sensitive to power. Second, the TestBed station requires three or more channels pass the trigger threshold within a 100 ns coincidence window. Combining the first and second conditions, we decided to use the third highest peak square voltage among channels in the trigger coincidence window as the variable sensitive to the trigger threshold (3rd highest V^2).

We found the timing of the trigger coincidence window with respect to the stored waveform for each channel separately (red boxes shown in Fig. 5.17). Using calibration pulser events in the data and the simulation, we reproduced calibration pulser events in the simulation and tuned the time difference between the trigger coincidence window and the timing of actual stored waveforms (result shown in Table. 5.1). For this, the unknown trigger threshold level is not crucial as the calibration pulser signal is a strong impulsive signal. Once we set the trigger threshold level high enough to avoid any trigger contamination from the thermal noise, this trigger coincidence window search is good to go.

Using the known distribution of trigger coincidence window timings with respect to the waveform, we found the 3rd highest V^2 inside the trigger coincidence window, which is the variable sensitive to the trigger threshold. One example of finding the 3rd highest V^2 from a calibration pulser event data is shown in Fig. 5.17. In order

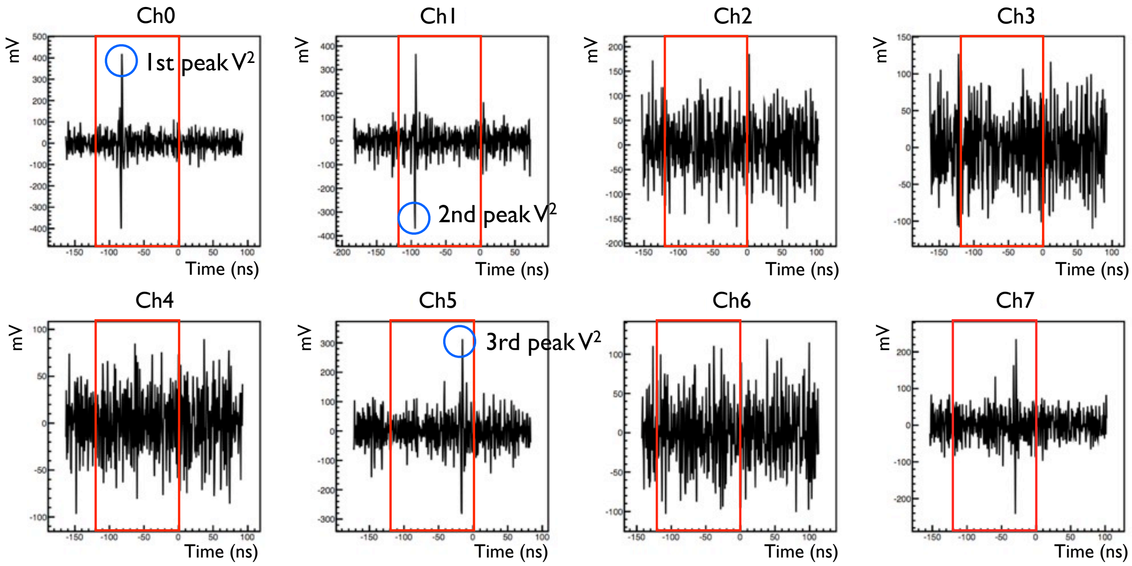

Figure 5.17: One example of finding the trigger-threshold sensitive variable from 8 borehole channels. The trigger-threshold sensitive variable is the 3rd highest peak square voltage among channels in trigger coincidence window. In the plots, red box is the trigger coincidence window for each corresponding channel. In the plots, Channel 0 has the highest peak V^2 among all channels, Channel 1 has the send highest peak V^2, and Channel 5 has the 3rd highest peak V^2 which is the trigger sensitive variable. The distribution of this trigger-threshold sensitive variable is shown in Fig. 5.18.

Channel Number	0	1	2	3	4	5	6	7
Waveform Time Offset (ns)	0	+50	-10	+20	+30	+20	-10	+10

Table 5.1: The tuned time offset between channels by comparing Testbed calibration pulser waveforms and simulated calibration pulser waveforms. Offset values are obtained with respect to Channel 0.

Channel Number	0	1	2	3	4	5	6	7
Trigger Threshold	-6.1	-5.4	-5.8	-5.5	-5.1	-5.9	-5.5	-5.9

Table 5.2: The trigger threshold obtained from the minimum χ^2 between the simulation and the Testbed data. The unit of trigger threshold is RMS of tunnel diode output from thermal noise waveform.

to calibrate the trigger level for each individual channel, we generated numerous thermal noise simulation sets with different trigger threshold levels. For each channel separately, we obtained the distribution of the 3rd highest V^2 from the thermal noise simulations and Testbed data (see Fig. 5.18) with different trigger threshold values. The unit of trigger threshold is RMS of tunnel diode output from thermal noise waveform. As tunnel diode is a power integrator, trigger threshold is proportional to the power of the input waveform over $\sim$ 10 ns (Section 4.1). For the Testbed data, we applied quality cuts and a stringent CW cut to remove CW contamination from the data set. From the distributions, we found the threshold which gave us the minimum χ^2 between the simulation and the Testbed data. The trigger threshold values that gave the minimum χ^2 between the simulation and the Testbed data are shown in Table. 5.2. After the calibrations on the thermal noise and trigger threshold are done, we generated numerous neutrino simulation sets for our data analysis.

Appendix: First estimation on Ray Tracing

RaySolver in AraSim uses a semi-analytic approach to obtain the first estimated launching angle at the source location given the horizontal distance to the source and indices of refraction at the source and target. Here, we provide the derivation of Eq. 5.3 for the exponential index of refraction model. The index of refraction model

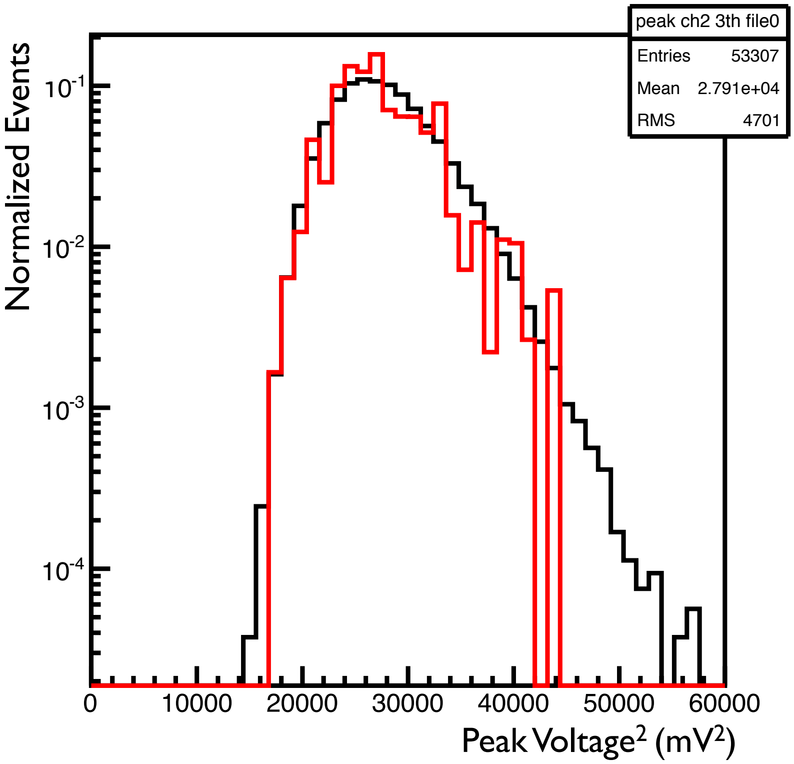

Figure 5.18: Comparison between the simulated triggered events and Testbed RF triggered events for Channel 2. The trigger threshold value used for the simulation set give us the minimum χ^2 from the Testbed data. Good agreement between the simulation and the data is shown.

is given as:

$$n(z) = A + Be^{C\cdot z} \tag{5.32}$$

where n is index of refraction value, z is the depth, and A, B, and C are fitted parameter values from the South Pole measurements. From the above equation, we can obtain:

$$\begin{aligned} \frac{dn}{dz} &= BCe^{C\cdot z} \\ \frac{dn}{n} &= \frac{BCe^{C\cdot z}}{A + Be^{C\cdot z}}dz, . \end{aligned} \tag{5.33}$$

Now we take θ to be the launch angle of a signal with respect to the normal to the surface. Taking n_{r} and $\sin\theta$ for the index of refraction and refracted angle with respect to normal, we can derive using Snell's law:

$$\begin{aligned} n\sin\theta &= n_{\mathrm{r}}\sin\theta_{\mathrm{r}} \\ dn &= \frac{-n_{\mathrm{r}}\sin\theta_{\mathrm{r}}}{\sin^2\theta}\cos\theta d\theta \\ \frac{dn}{n} &= -\cot\theta d\theta \end{aligned} \tag{5.34}$$

where θ is the direction of the ray with respect to the direction normal to the surface.

Using Eq. 5.33 and 5.34 and integrating from the source location to the target location, we obtain:

$$\begin{aligned}
\int_{z_0}^{z} \frac{BCe^{Cz}}{A + Be^{Cz}} &= \int_{\theta_0}^{\theta} -\cot\theta \\
\ln(A + Be^{C\cdot z'})\Big|_{z_0}^{z} &= -\ln(\sin\theta')\Big|_{\theta_0}^{\theta} \\
\frac{A + Be^{C\cdot z}}{A + Be^{C\cdot z_0}} &= \frac{\sin\theta_0}{\sin\theta} \\
\theta = \arcsin &\left(\sin\theta_0 \frac{A + Be^{C\cdot z_0}}{A + Be^{C\cdot z}}\right). \qquad (5.35)
\end{aligned}$$

where θ_0 is the launch angle at the source location with respect to normal to the surface and z_0 is the depth at the source.

Using Eq. 5.35 and the relation $dx/dz = \tan\theta$:

$$dx = \tan\left[\arcsin\left(\sin\theta_0 \frac{A + Be^{C\cdot z_0}}{A + Be^{C\cdot z}}\right)\right] dz \qquad (5.36)$$

and integrating the equation from the source location to the target location, we obtain:

$$\begin{aligned}
x - x_0 &= \int_{z_0}^{z} \tan\left[\arcsin\left(\sin\theta_0 \frac{A + Be^{C\cdot z_0}}{A + Be^{C\cdot z'}}\right)\right] dz' \\
&= \int_{z_0}^{z} \frac{\sin\theta_0 (A + Be^{C\cdot z_0})}{A + Be^{C\cdot z'} \sqrt{1 - \left(\frac{\sin\theta_0 (A + Be^{C\cdot z_0})}{A + Be^{C\cdot z'}}\right)^2}} dz'. \qquad (5.37)
\end{aligned}$$

In order to make above Eq.5.37 more manageable, we let:

$$\begin{aligned}\sigma_0 &\equiv \sin\theta_0 \\ n &\equiv A + Be^{C\cdot z} \\ dn &= BCe^{Cz}dz \\ dz &= \frac{dn}{C(n-A)}\end{aligned} \tag{5.38}$$

and with these substitutions, Eq. 5.37 becomes:

$$\begin{aligned}x - x_0 &= \frac{\sigma_0 n_0}{C}\int_{n_0}^{n}\frac{dn'}{n'(n'-A)\sqrt{1-\left(\frac{\sigma_0 n_0}{n'}\right)^2}} \\ \frac{C}{\sigma_0 n_0}(x-x_0) &= \int_{n_0}^{n}\frac{dn'}{(n'-A)\sqrt{n'^2-\sigma_0^2 n_0^2}}.\end{aligned} \tag{5.39}$$

Now substituting n with $m \equiv n - A$, the equation becomes:

$$\begin{aligned}&\frac{C}{\sigma_0 n_0}(x-x_0) \\ &\quad= \int_{m_0}^{m}\frac{dm'}{m'\sqrt{m'^2+2Am'+A^2-\sigma_0^2 n_0^2}}.\end{aligned} \tag{5.40}$$

From Eq. 5.40, we can make the equation more compact with an additional substitution $X \equiv a + bm' + cm'^2$ where $a = A^2 - \sigma_0^2 n_0^2$, $b = 2A$, and $c = 1$. With the replacement, the equation is now:

$$\frac{C}{\sigma_0 n_0}(x-x_0) = \int_{m_0}^{m}\frac{dm'}{m'\sqrt{X}}. \tag{5.41}$$

With the condition that $a \geq 0$ due to the fact that A is the index of refraction value at the deep ice and $\sigma_0 = \sin\theta_0 \geq 0$, the integration of the right-hand-side of the Eq. 5.41 can be solved using [90]:

$$\int \frac{dx}{x\sqrt{X}} = \frac{-1}{\sqrt{a}} \ln \left(\frac{2a + bx + 2\sqrt{aX}}{x} \right). \tag{5.42}$$

After the integration from Eq. 5.40, the equation becomes:

$$\begin{aligned} &\frac{C\sqrt{A^2 - \sigma_0^2 n_0^2}}{\sigma_0 n_0}(x_0 - x) \\ &= \ln \left(\frac{\sqrt{\left(n^2 - \sigma_0^2 n_0^2\right)\left(A^2 - \sigma_0^2 n_0^2\right)} + An - \sigma_0^2 n_0^2}{n - A} \right) \\ &- \ln \left(\frac{\sqrt{\left(n_0^2 - \sigma_0^2 n_0^2\right)\left(A^2 - \sigma_0^2 n_0^2\right)} + An_0 - \sigma_0^2 n_0^2}{n_0 - A} \right). \end{aligned} \tag{5.43}$$

This is Eq. 5.3, and all values are given parameters from the index of refraction model and the source and target locations except the launching angle σ_0 which is the single unknown.

Chapter 6

A Search for UHE Neutrinos in the Testbed Station of the Askaryan Radio Array

The contents of this chapter are largely taken from [2].

The Askaryan Radio Array (ARA) is an ultra-high energy (UHE, $> 10^{17}$ eV) cosmic neutrino detector in phased construction near the South Pole. ARA searches for radio Cherenkov emission from particle cascades induced by neutrino interactions in the ice using radio frequency antennas ($\sim$ 150-800 MHz) deployed at a design depth of 200 m in the Antarctic ice. A prototype ARA Testbed station was deployed at $\sim$ 30 m depth in the 2010-2011 season and the first three full ARA stations were deployed in the 2011-2012 and 2012-2013 seasons. We present the first neutrino search with ARA using data taken in 2011 and 2012 with the ARA Testbed and the resulting constraints on the neutrino flux from 10^{17}-10^{21} eV.

6.1 Introduction

The Askaryan Radio Array (ARA) aims to measure the flux of ultra-high energy (UHE) neutrinos above 10^{17} eV. While UHE neutrinos are so far undetected, they are expected both directly from astrophysical sources and as decay products from the

GZK process [21, 22], as first pointed out by Berezinsky and Zatsepin [91, 92]. The GZK process describes the interactions between cosmic rays and cosmic microwave and infrared background photons above a $\sim 10^{19.5}$ eV threshold.

The interaction of a UHE neutrino in dense media induces an electromagnetic shower which in turn creates impulsive radiofrequency (RF) Cherenkov emission via the Askaryan effect [61, 62, 93–96]. In radio transparent media, these RF signals can then be observed by antenna arrays read out with $\sim$ GHz sampling rates.

Currently, the most stringent limits on the neutrino flux above 10^{19} eV have been placed by the balloon-borne ANITA experiment sensitive to impulsive radio signals from the Antarctic ice sheet [9]. Below 10^{19} eV, the best constraints on the neutrino flux currently come from the IceCube experiment, a 1 km^3 array of photomultiplier tubes in the ice at the South Pole using the optical Cherenkov technique [11]. IceCube has recently reported the first cosmic diffuse neutrino flux, which extends up to $\sim 10^{15}$ eV. This is two orders of magnitude lower energy than ARA's energy threshold [97].

Due to the ~ 1 km radio attenuation lengths in ice [31, 98], radio arrays have the potential to view the 100s of km^3 of ice necessary to reach the sensitivity to detect ~ 10 events per year from expected UHE neutrino fluxes.

6.2 Method

Our analysis reconstructs events using an interferometric map technique. For this analysis, we consider RF triggered events from January 8th, 2011 to December 31st, 2012 and use a set of optimized cuts using AraSim calibrated against Testbed data to eliminate background events from our final sample. This analysis is performed in two stages. Stage 1 was a complete analysis on a limited data set that had been processed at an early period of data processing. This Stage 1 analysis is carried on data from February-June of 2012 only, optimizing cuts on the 10% set before opening the box on that time period alone. Then, in Stage 2 the analysis is expanded to the remainder of time in the two year period once more processed data became available. In Stage 2, the cuts were re-optimized on the 10% set for the two year period but excluding February-June 2012 which had already been analyzed.

6.2.1 Testbed Local Coordinate

All the correlation and interferometric maps shown in this analysis are based on the Testbed local coordinate system which is defined with the $+\hat{x}$ along the direction of the ice flow. The $x-y$ plane is a tangent to the geoid at the time the Testbed is deployed and $\hat{z}$ is defined as $\hat{z} = \hat{x} \times \hat{y}$. The origin of the coordinate is the mean of the antenna positions which is ~ 20 m deep in the ice for the Testbed. The azimuthal angle at $\phi = 0^\circ$ is the direction towards $+\hat{x}$, and $\phi = 90^\circ$ is $+\hat{y}$ direction. The zenith angle $\theta = 0^\circ$ the horizontal direction from the origin, while $\theta = +90^\circ$ and $\theta = -90^\circ$ are $+\hat{z}$ and $-\hat{z}$ direction, respectively.

6.2.2 Analysis Cuts

Here we begin a description of all of the cuts applied in the Interferometric Map Analysis. In both stages of the analysis, first we apply Event Quality Cuts to reject anomalous electronics behavior. Due to the increase in radio backgrounds during the summer season at the South Pole, we only allow events from February 16^{th} to October 22^{nd} in each year to pass our cuts. This period is selected based on the IceCube drilling periods in the 2011 to 2013 seasons. The period from April 6^{th} to May 12^{th} 2012 was characterized by consistent instability in the digitization electronics and thus this period is excluded as well. We remove calibration pulser events with a timing cut of width 80 ms centered around the beginning of the GPS second, which is when the

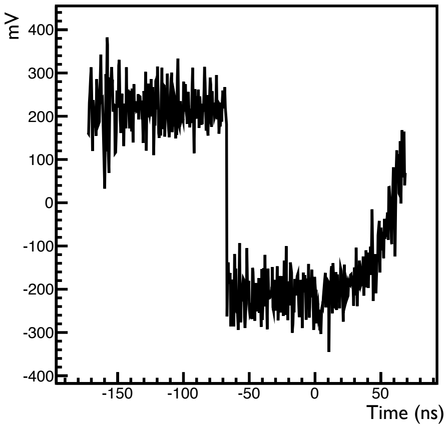

Figure 6.1: An example of an event waveform with a weird electronics error. The DC component of the waveform provides the power contribution below the 150 MHz high-pass-filter of the system and thus rejected by the Event Quality Cuts.

calibration pulser signal is expected to arrive. We also remove events with corrupted waveforms, which comprise $\sim 1\%$ of the entire data set. We also reject an event if, in two or more channels, the power in frequencies below the high-pass-filter cut-off frequency of 150 MHz is greater than 10% of the waveform's power. This cut is designed to eliminate specific electronics errors that are otherwise difficult to identify. Fig. 6.1 is an example waveform which is rejected by this cut. The percentage of simulated neutrino events rejected by this cut is less than 1%.

We attempt a directional reconstruction for each event using the relative timing information and maximizing a summed cross-correlation over a set of hypothesized source positions. We perform a cross-correlation on the waveforms from each pair of antennas of the same polarization. This cross-correlation function measures how similar the two waveforms are with a given offset in time. For each pair of antennas, we calculate the expected delays between the signal arrival times as a function of the position of a putative source relative to the center of the station. The center of the station is located at the mean of the antenna positions ~ 20 m deep in the ice. These signal arrival times account for the depth-dependent index of refraction in the firn layer and the abrupt change at the ice-air interface (Section 5.1.4). If there are two ray trace solutions, only the direct one is considered. For a given source position, the cross-correlation value for an antenna pair is given by:

$$C = \frac{\sum_{i=1}^{N_{\text{bins}}} V_{1,i} \cdot V_{2,i+n}}{\sqrt{\sum_{i=1}^{N_{\text{bins}}} V_{1,i}^2} \cdot \sqrt{\sum_{i=1}^{N_{\text{bins}}} V_{2,i+n}^2}} \tag{6.1}$$

where $V_{1,i}$ is the voltage in the i^{th} bin at the first antenna in the pair and $V_{2,i+n}$ is the voltage in the $(i+n)^{\text{th}}$ bin at the second antenna where n is the number of bins corresponding to the expected time delay between the antennas for a signal from the putative source position. Then, for each source direction, the correlation values for each pair of antennas of the same polarization are weighted by the inverse of the integrated power of the overlap between the waveforms (denominator of Eq. 6.1) and Hilbert-transformed before being summed together to make the summed cross-correlation. The Hilbert-transformation is done in order to interpret the correlation power. Fig. 6.2 shows an example of obtaining the correlation function from a calibration pulser event. The top two plots are the voltage waveforms from two chosen channels to make the correlation function. The cross-correlation waveform from these two waveforms, using the Eq. 6.1, is shown in the bottom left plot of Fig. 6.2. The final correlation function, which is the Hilbert-transformation of the bottom left plot of Fig. 6.2, is shown in the bottom right plot of Fig. 6.2.

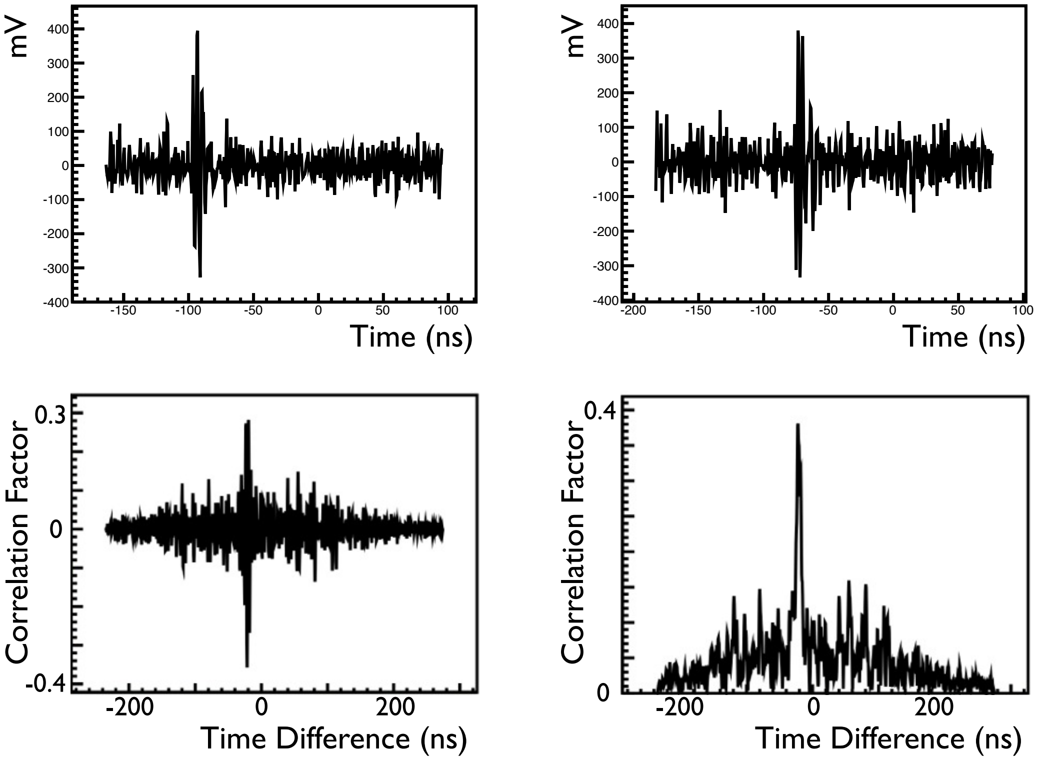

Figure 6.2: Series of waveforms that show the process to obtain the correlation function from a pair of antennas. The top two plots are two voltage waveforms from two antennas that are chosen as a pair to produce the correlation function. All plots are obtained from same calibration pulser event. Both plots are from horizontally polarized antennas Channel 0 and Channel 1, respectively. The bottom left plot is the cross-correlation waveform from the top two waveforms. The bottom right plot is the Hilbert-transformed of the bottom left plot.

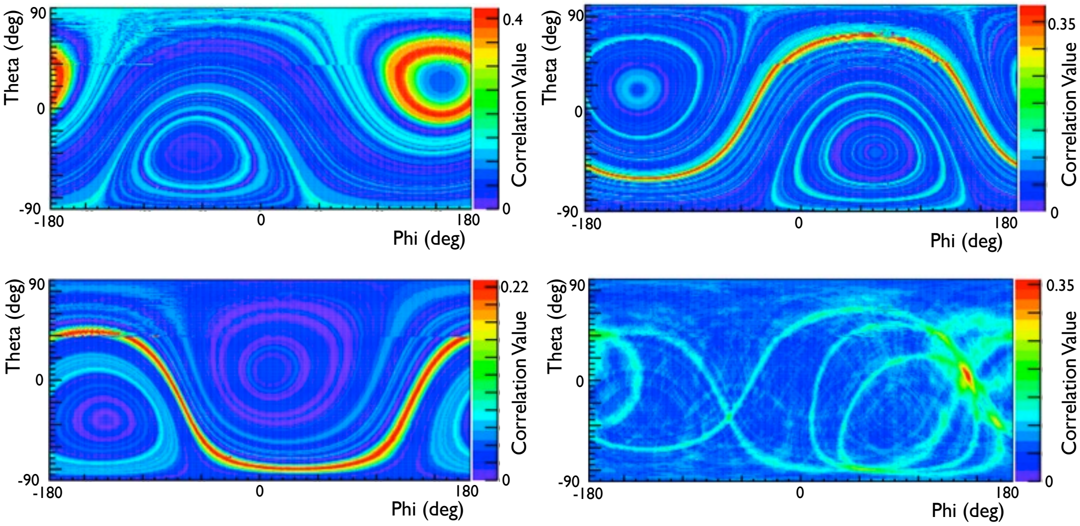

Figure 6.3: Examples of correlation maps and the final interferometric map from the calibration pulser event (same event with Fig. 6.2). All maps are obtained from 30 m source distance assumption in order to reconstruct the calibration pulser which is located ∼ 30 m from the Testbed. The top two plots and the bottom left plot are the correlation maps from different pair of antennas in same polarization. From the Testbed, there are total 6 pairs for each polarization. The correlation value on the map is the projection of the cross-correlation function (bottom right plot of Fig. 6.2) with the corresponding signal travel time difference between the antennas. The bottom right plot is the final interferometric map obtained by summing correlation maps from all pairs with the normalization factor 6 from the number of pairs. The best reconstruction direction from the map (red peak region around 0° zenith and 140° azimuthal angle) is the direction of the calibration pulser as expected.

Summed cross-correlations for each polarization for each event are summarized in maps with 1°×1° bins in zenith and azimuth for source distances of 3 km and 30 m only. We use the 30 m map to determine if the event is a calibration pulser signal that has not been properly flagged, and the 3 km map to determine the reconstruction direction of sources hypothesized to be from far away, such as neutrino events. The two top plots and the bottom left plots in Fig. 6.3 are the examples of correlation map from a pair of antennas for a calibration pulser event (same event as in Fig. 6.2). Each 1°×1° bin value in the correlation map is the correlation function (bottom right plot of Fig. 6.2) at the expected signal delay difference between antennas for that source direction and distance. The final interferometric map is obtained by summing all correlation maps with the additional normalization factor 6, which is the number of pair of antennas (bottom right plot of Fig. 6.2). We define the reconstruction direction to be the location of the peak in the interferometric map. Based on the calibration pulser events, our pointing resolution on the RF direction is $\sim 1^\circ$ (Fig. 6.4).

Based on the reconstruction map generated by the interferometric reconstruction technique just described, we decide whether the map is of good quality in terms of pointing directionality. When the signal is coming from one specific location and generates a consistent pattern of waveforms across multiple channels, the reconstruction map will point back to the direction of the source location. A set of Reconstruction Quality Cuts ensure that the event can be characterized by a single well-defined pointing direction that does not have an overly broad spot size on the map. Thermal noise events will not exhibit this strong well-defined peak in an interferometric map. The Reconstruction Quality Cuts also require that any strong correlation is not found in only a single 1°×1° bin on the map with no other comparable sized correlation values nearby. This would not be consistent with the antenna and electronics responses of the detector.

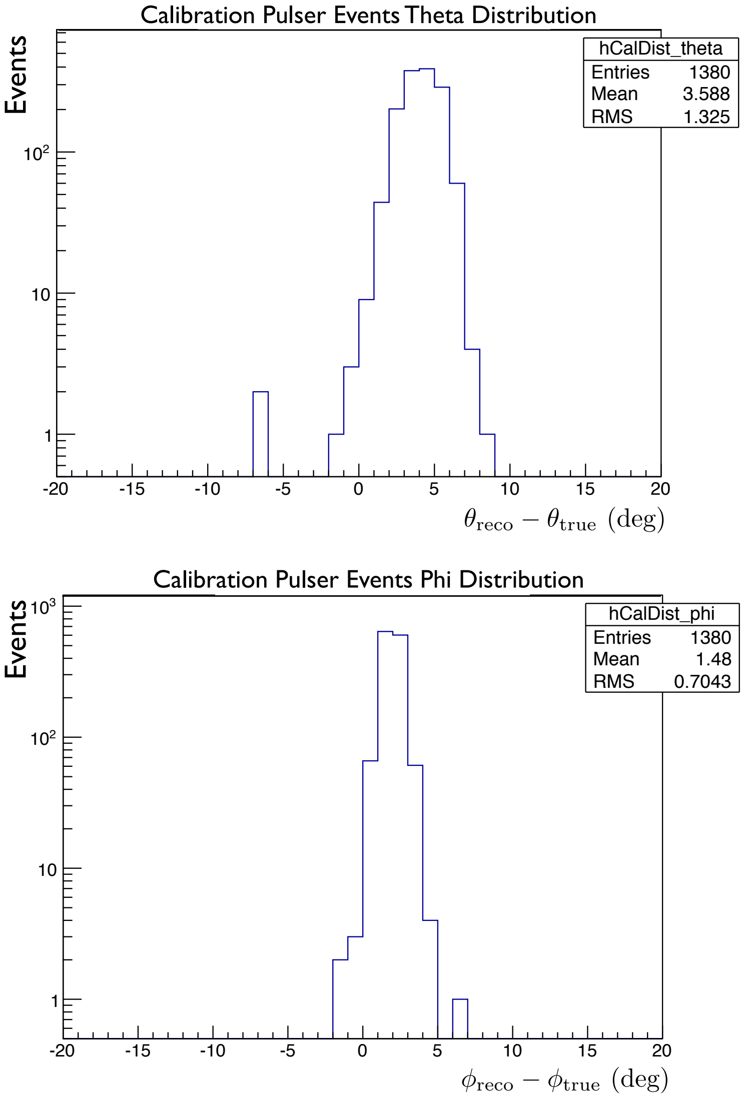

Calibration Pulser Events Theta Distribution

Calibration Pulser Events Phi Distribution

Figure 6.4: Distribution of calibration pulser events' reconstructed direction. The top plot is the distribution in zenith angle (θ) difference between the true direction and the reconstructed direction, while the bottom is the distribution plot in azimuthal angle (ϕ). Zenith angular resolution is approximately factor of two worse than azimuthal angular resolution due to the error in depth-dependent index of refraction model.

The Reconstruction Quality Cuts are based on an area surrounding the peak correlation where the correlation remains high, A_{peak}, and the total area on the map showing high correlations, A_{total}. We first find the 85% contour surrounding the point of peak correlation and the area of that contour in square degrees, which we call A_{peak}. The choice of the 85% level for the contour was somewhat arbitrary. A different choice would have led to a different maximum allowed A_{peak}. Fig. 6.5 and 6.6 are examples of an interferometric map and its 85% contour area plot, respectively. The total area on the map that shows a correlation higher than 85% of the maximum correlation value is called A_{total}.

The first Reconstruction Quality Cut condition requires the size of A_{peak} to be greater than 1 deg^2 and less than 50 deg^2. The minimum of that range is the area of a single bin on the map, due to individual time bins in the waveforms and in Fig. 6.7 bottom plot shows that this $A_{\text{peak}} > 1$ deg^2 cut doesn't dramatically affect the neutrino efficiency for the maximal Kotera *et al.* flux model. The 50 deg^2 was chosen because in a distribution of A_{peak} from calibration pulser events shown in the top plot of Fig. 6.7, it was $\sim 2\sigma$ away from the mean of the distribution at ~ 36.8 deg^2. Note that the area of the 85% contour around the peak is not the same as the resolution of the reconstruction. Instead, the area of the contour is related to the width of the readout impulse.

The second condition for the Reconstruction Quality Cut requires the ratio between A_{total} and A_{peak} to be less than 1.5. This means that only one reconstruction direction dominates the map.

Each event is separated into VPol and HPol channels based on which polarizations pass the Reconstruction Quality Cuts. A VPol or HPol channel is required to pass both Reconstruction Quality Cuts in the 3000 m maps. If an event passes both VPol and Hpol Reconstruction Quality Cuts, that event will be analyzed in both VPol and

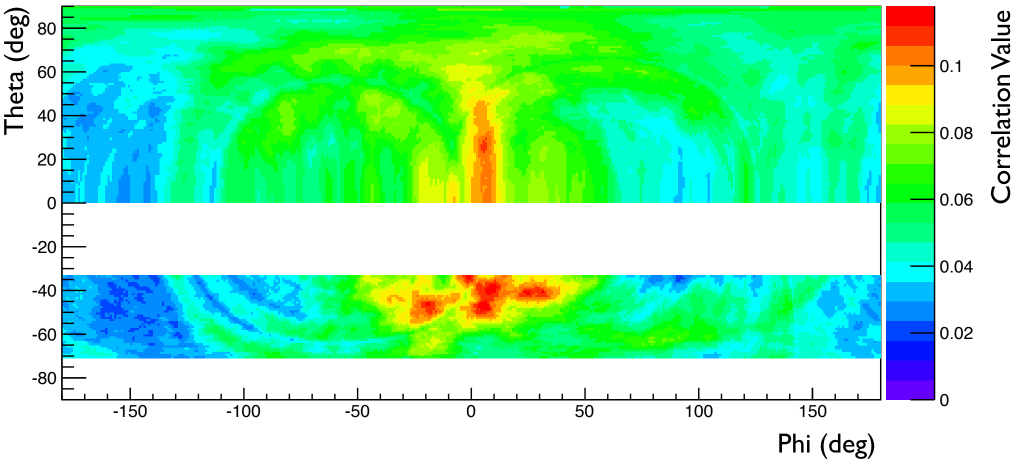

Figure 6.5: An example of a interferometric map used for reconstruction. This map is obtained from VPol channels with a 3000 m distance assumption from the station. The shadow region due to the ray-tracing in the depth-dependent index of refraction yielded the empty horizontal band in the middle of the plot. The shadow region effect is illustrated in Fig. 5.3. The 85% contour around the peak of this plot is shown in Fig. 6.6.

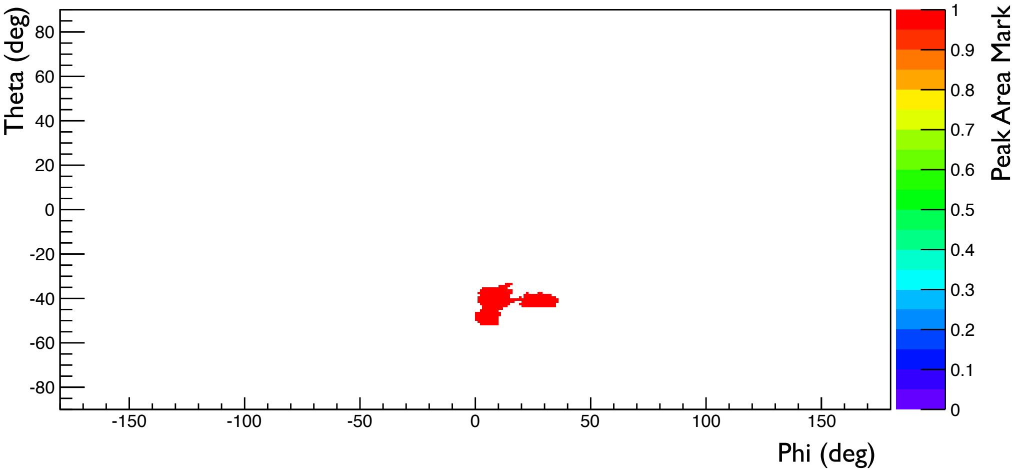

Figure 6.6: An example of an 85% contour around the peak. This plot of peak area is obtained from Fig. 6.5. The red colored filled area is the 85% contour region around the peak and the integrated solid angle of the region is $A_{\text{peak}} = 226.5\ \text{deg}^2$.

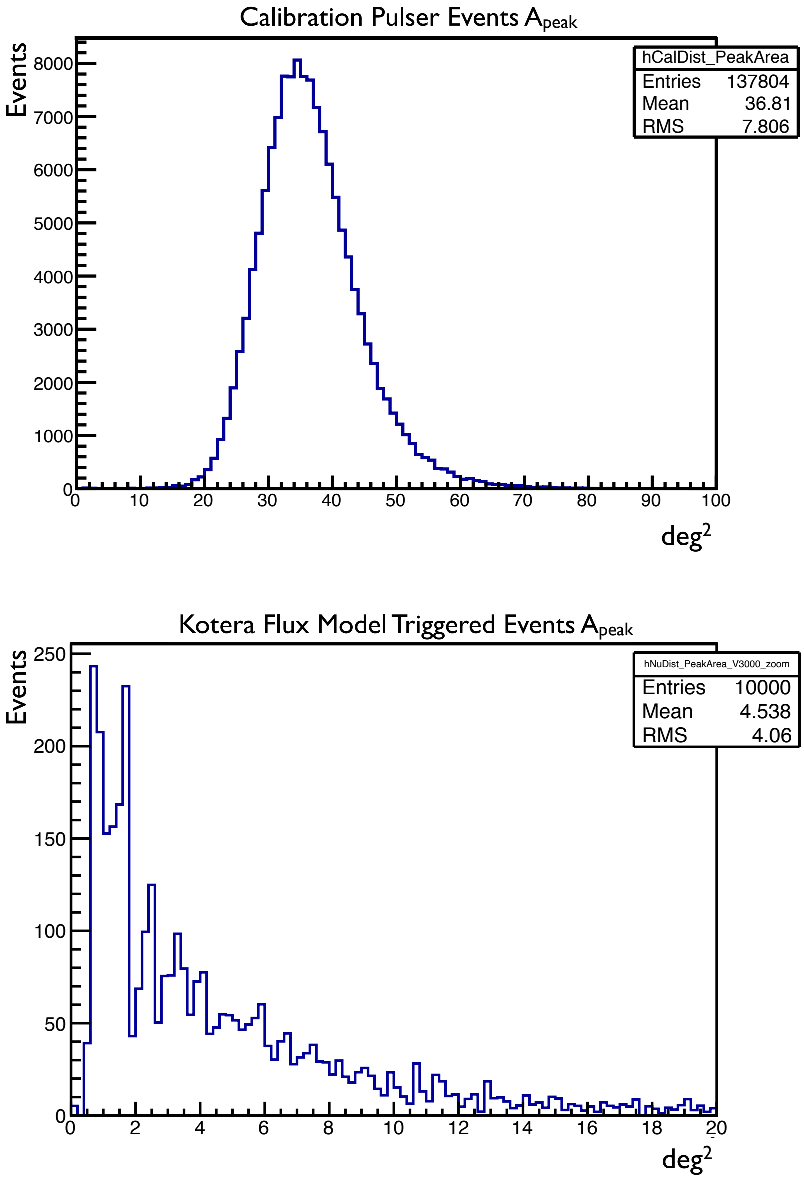

Figure 6.7: The distribution of 85% contour area from 2012 HPol calibration pulser events (top) and simulated neutrino events from maximal Kotera *et al.* flux model. From the calibration pulser events' plot, we set the maximum allowed A_{peak} at $\sim 2\sigma$ away from the mean of the distribution, at 50 deg^2. The signal plot (bottom) shows that the minimum allowed A_{peak} at 1 deg^2 has a minimal effect on the neutrino efficiency.

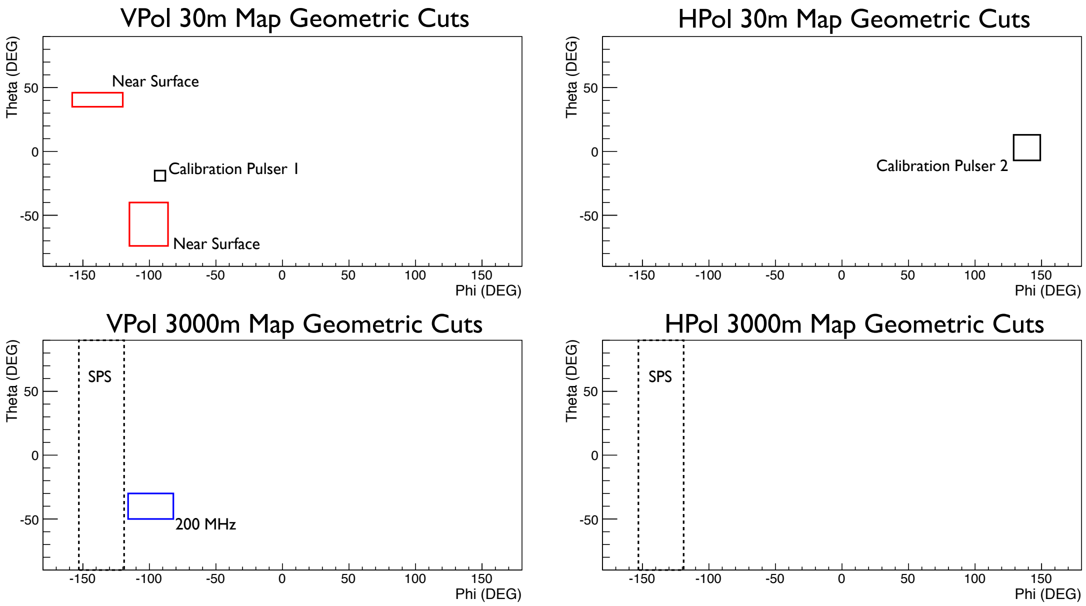

Figure 6.8: All Geometric Cuts for each reconstruction map.

HPol channels. For the purpose of tabulating results, the rest of the cuts are applied to VPol and/or HPol channels separately after the Reconstruction Quality Cut. The cuts applied to each polarization are the same and for any event, one or both channels may pass the cuts.

A set of Geometric Cuts reject events that reconstruct to locations where background due to anthropogenic noise is expected to be high, either where there is known human activity or where signals reconstruct to the same location repeatedly. See Fig. 6.8 for all Geometric Cuts for each reconstruction map. The reconstructed directions used for this cut are derived using the interferometric reconstruction technique described above. Events that reconstruct to South Pole Station (SPS) are rejected. This area covers a region from -153° to -119° in azimuthal angle. Events that reconstruct to within a box in zenith and azimuth centered around the location of a calibration pulser are also rejected. There are two calibration pulsers for the Testbed and therefore two box regions for each of them. The first calibration pulser box includes zenith angles of $-23° < \theta < -15°$ and azimuthal angles of $-96° < \phi < -88°$ in VPol 30 m map (calibration pulser 1 in Fig. 6.8). The second calibration pulser box is centered at 3° zenith angle and 139° in azimuthal angle in the HPol 30 m map, and stretches in both zenith and azimuthal angles in $\pm 10°$ (calibration pulser 2 in Fig. 6.8).

Additionally, we reject regions where multiple events reconstruct after the Event Quality Cuts, Reconstruction Quality Cuts, Continuous Wave (CW) Cut, and Delay Difference Cut have been applied (the CW Cut and the Delay Difference Cut are described in following paragraphs). These applied cuts reject known backgrounds (CW backgrounds) and poorly reconstructing events and make us look at the distribution of the direction of the events. Thermal noise events will isotropically distribute over the map while events that are originated from specific locations will cluster toward to source direction. As neutrino events are not expected to originate from the same position repeatedly, we reject events that reconstruct to the repeating source locations. From the distribution maps after the set of cuts, we calculated the expected background events for each repeating location using the Gaussian functional fit in azimuth and zenith angles. We defined the size of the box for the repeating locations so that the total expected background events from the clustering Geometric Cuts are same with the background expectation from the final Peak/Correlation Cut (Section. 6.2.3).

Three repeating locations were identified in the Interferometric Map Analysis, two in the VPol 30 m map, and another on the VPol 3 km map (Fig. 6.8). The events reconstructing to either repeating location in the Vpol 30 m map are characterized as “near surface” events as they appear to come from a point near the surface of the ice at $\theta \approx +40°$ relative to the station center. The two locations in the VPol 30 m map reject the “near surface” events where the best reconstructed location for these type of events can be either of two locations depending on the strength of the signal.

The first of these two reconstruction locations for “near surface” events is centered at a zenith angle of 40° and an azimuth of -140°. We reject any events whose VPol 30 m reconstruction peak points to within a box that is 10° in zenith and 40° wide in azimuth and centered on that location. The second of the two reconstruction locations for “near surface” events is centered at a zenith angle of -57° and an azimuth of -100°. We reject any events whose VPol 30 m reconstruction points within a $30^\circ \times 30^\circ$ box in zenith and azimuth surrounding that point.

One repeating location was identified in the VPol 3 km map and these events are characterized by an excess of power in a $\sim$ 50 MHz band around 200 MHz, and as such are labeled “200 MHz” events. This “200 MHz” repeating region from the VPol 3000 m map is centered at a zenith angle of -40° and an azimuth of -99° with the rejection region being 20° wide in azimuth and 34° high in zenith. As with the “near surface” events, there is a secondary reconstruction point but it is located within the SPS reconstruction region and thus events that reconstruct there are already rejected. These events from repeating locations are expected to be more effectively rejected by other means after improving the reconstruction method in a future analysis.

A Saturation Cut rejects events where the saturation of the amplifier induces distortion of the waveform. When the signal strength is strong enough to saturate the amplifier and change the linearity of the amplification factor, we may have misleading reconstructed information from the event and thus we want to remove it from consideration. As the maximum dynamic range of the amplifiers of the borehole antennas is $\sim \pm 1$ V, we set the saturation point of the output voltage to ± 995 mV and when two or more channels’ waveforms have maximum voltage values that exceed the saturation point, we reject the event.

The Gradient Cut is a pattern recognition cut to reject “200 MHz” background events which have a strong gradient in signal strength across the Testbed in one direction. The Geometric Cut for “200 MHz” was not sufficient to reject this specific type of background event because the Geometric Cuts are effective for sources located at ~ 30 m or > 1 km distance from the Testbed, while only a closer source can give us such a large gradient in signal strength across the station. We first check whether there is a gradient in signal strength in the direction that matches that of these background events, where one of the two VPol channels facing SPS has the strongest $\mathrm{V_{peak}}$/RMS value for these events while one of other two VPol channels have the weakest signal strength. When the above pattern matches for an event, we calculate the gradient value, G, given by

$$G = \frac{|V_{\mathrm{max}} - V_{\mathrm{min}}|}{\sqrt{V^2_{\mathrm{RMS,max}} + V^2_{\mathrm{RMS,min}}}} \qquad , \tag{6.2}$$

where V_{max} is the peak voltage of the channel with the highest $\mathrm{V_{peak}}$/RMS, V_{min} is the peak voltage of the channel with the lowest $\mathrm{V_{peak}}$/RMS, and $V_{\mathrm{RMS,max}}$ and $V_{\mathrm{RMS,min}}$ are the RMS voltages of those same channels respectively. If the gradient value is greater than 3.0 we reject the event. Fig. 6.9 shows the distribution of gradient values from events that pass the Event Quality Cuts, while Fig. 6.10 shows gradient values' distribution after applying the Event Quality Cuts, the Saturation Cut, the Delay Difference Cut and the Geometric Cuts. The goal of the Gradient Cut is to reject events in Fig. 6.10 (target background events) and allowing events in Fig. 6.9 (other backgrounds which are not meant to be rejected by the Gradient Cut). A Gradient cut value 3.0 gives us $\sim 2.3\ \sigma$ and $\sim 1\ \sigma$ from the mean value for Fig. 6.9 and 6.10, respectively.

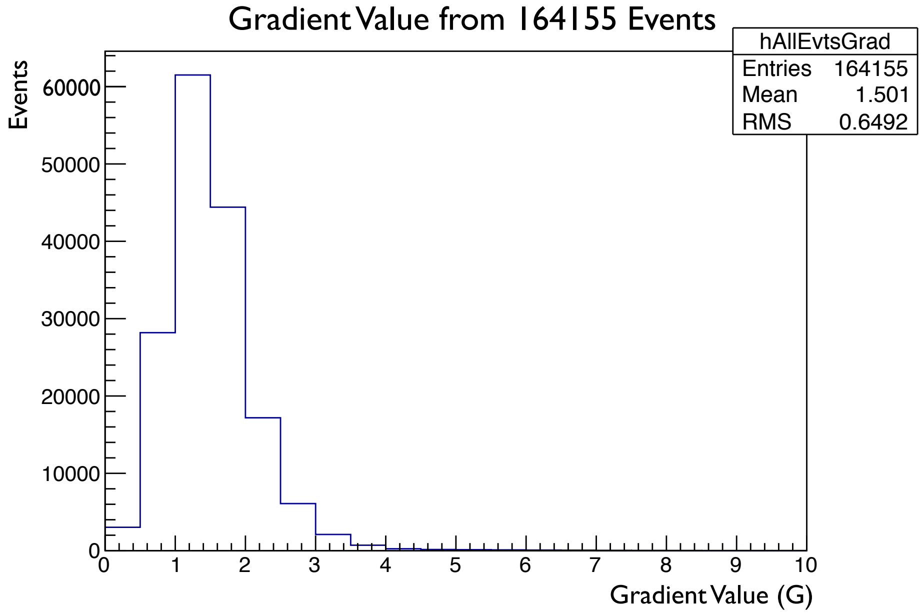

Figure 6.9: The distribution of gradient value G from 10% Testbed burned sample with the Event Quality Cuts applied. Our gradient cut value 3.0 is approximately 2.3 σ away from the mean value 1.5. Distribution of gradient value from the selected background events are shown in Fig. 6.10.

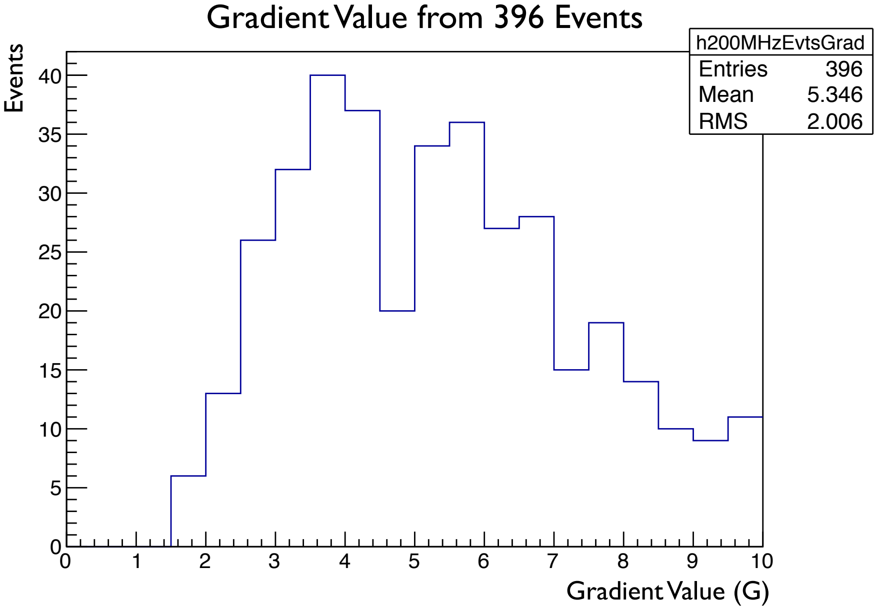

Figure 6.10: The distribution of gradient value G from the Testbed 10% burned sample with analysis cuts to select events that should be rejected by gradient cut. The Saturation cut, Delay Difference cut, and Geometric Cuts are applied. The gradient cut value of 3.0 is approximately 1 σ from the mean value.

The Delay Difference Cut ensures that the reconstruction direction derived from all of the borehole antennas of the same polarization is consistent with the delay observed between the signals in the two antennas with the strongest signals. In the case of an impulsive signal like one coming from a neutrino event, we expect this correlation to exist whereas a thermal noise event in general should not exhibit this behavior in general. We calculate the time delay $\Delta t_{1,2,\mathrm{peak}}$ between the peak voltages $\mathrm{V_{peak}/RMS}$ in the two channels with the highest peak voltages. We also find the time delay that would be expected between those two channels based on the direction of reconstruction, $\Delta t_{1,2,\mathrm{reco}}$. We then find the difference between these two values, $\Delta \mathrm{T_{delay}} = \Delta \mathrm{t_{1,2,peak}} - \Delta \mathrm{t_{1,2,reco}}$. If $|\Delta \mathrm{T_{delay}}| > 20$ ns, we reject the event. The distribution of $|\Delta \mathrm{T_{delay}}|$ from calibration pulser events, 10% burned sample with the Quality Cuts and Geometric Cuts applied, and simulated neutrino events are shown in Fig. 6.11, 6.12, and 6.13. Both calibration pulser events and simulated neutrino events (Fig. 6.11 and 6.13) show that most of events are clustered at ~0 ns delay. On the other hand, Fig. 6.12 from the 10% burned sample with the Quality Cuts and Geometric Cuts applied, shows most of events distributed at a 2^{nd} highest $\mathrm{V_{peak}/RMS}$ less than 7 and widely spread over Delay Difference values. This is because both thermal noise and CW background events don't have impulsive signals (small 2^{nd} highest $\mathrm{V_{peak}/RMS}$) and correlation between the direction of reconstruction and the peak voltages in the waveforms (large Delay Difference values).

An In-Ice Cut rejects events that reconstruct to directions above horizontal as viewed by the Testbed. This cut is made because we are searching for neutrino events that are coming from the ice.

A Continuous Waveform (CW) Cut rejects events that are contaminated with narrowband anthropogenic noise. This cut rejects events that show a narrowband peak above an expected noise spectrum. To apply this cut, we need to first find the average

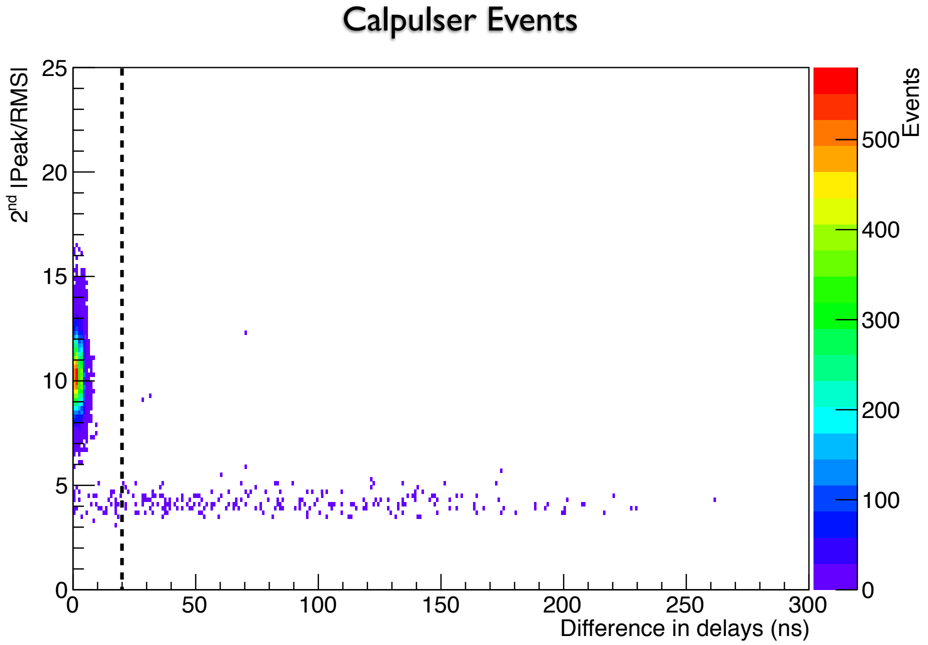

Figure 6.11: Distribution of the Delay Difference value $\Delta T_{\mathrm{delay}}$ from calibration pulser events. As expected, most events are clustered at ∼0 ns delay which means there is a strong correlation between the time difference between waveforms and the best reconstructed direction. The small number of events distributed at low V_{peak}/RMS are caused by thermal noise events that have leaked into the calibration pulser trigger timing window. Our Delay Difference Cut value of 20 ns is shown as a black vertical dotted line on the plot.

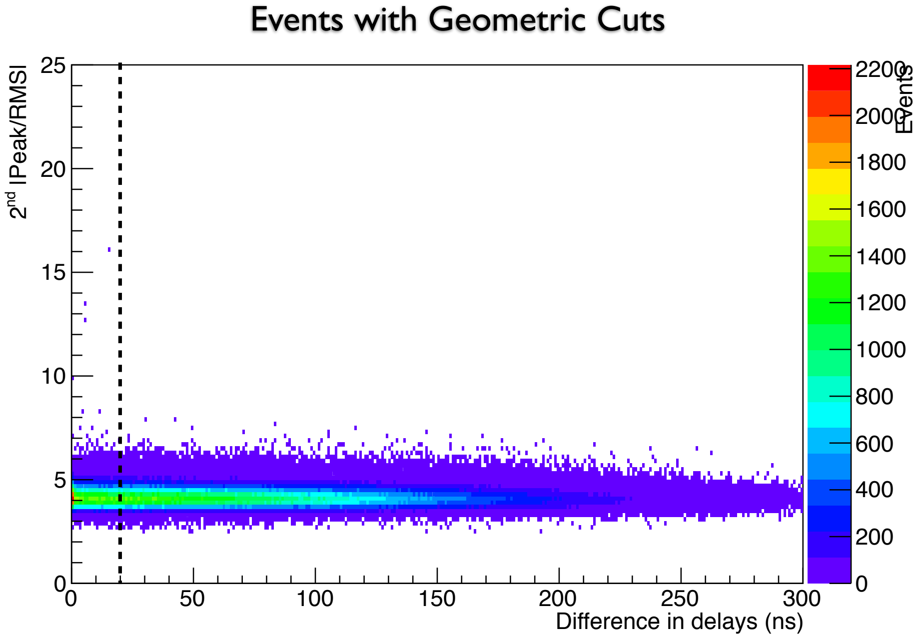

Figure 6.12: Distribution of the Delay Difference value ΔT_{delay} from the 10% Testbed burned sample with the Quality Cuts and Geometric Cuts applied. The distribution shows that most of events have a V_{peak}/RMS value less than 7 and widely spread over Delay Difference values. Therefore the dominant portion of events are thermal noise events and Continuous Waveform (CW) events. Our Delay Difference Cut value of 20 ns is shown as a black vertical dot line on the plot.

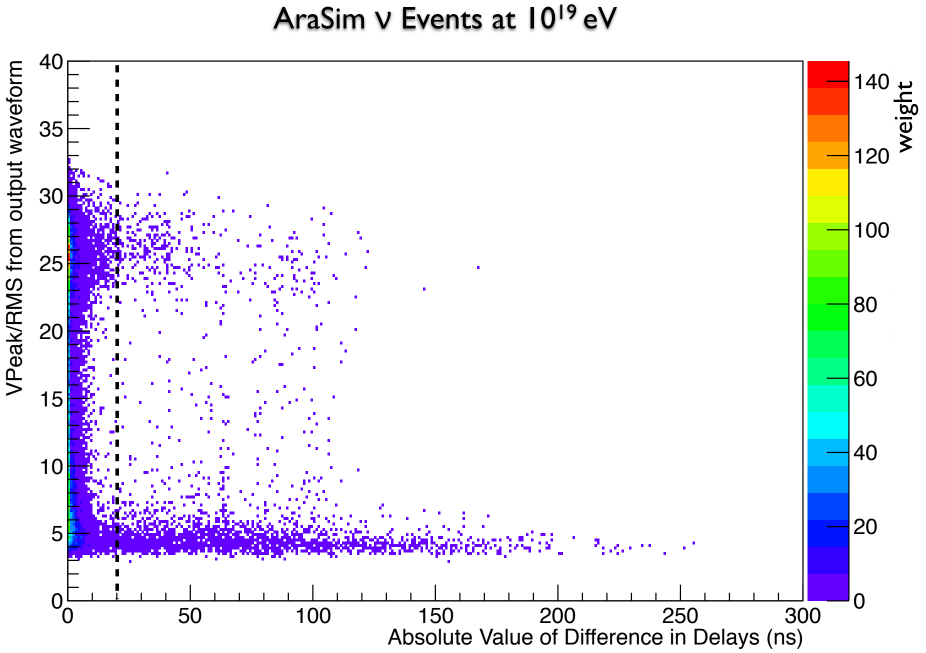

Figure 6.13: Distribution of the Delay Difference value $\Delta\mathrm{T}_{\mathrm{delay}}$ from triggered neutrino events from AraSim. The simulation is run with a fixed neutrino energy at 10^{19} eV. The delay Difference Cut value of 20 ns is shown as a black vertical dotted line on the plot, rejecting only a small portion of triggered neutrino events. The clustered events at high V_{peak}/RMS and low $\Delta\mathrm{T}_{\mathrm{delay}}$ are due to the Saturation Cut which restricts the maximum V_{peak}/RMS to ~ 30.

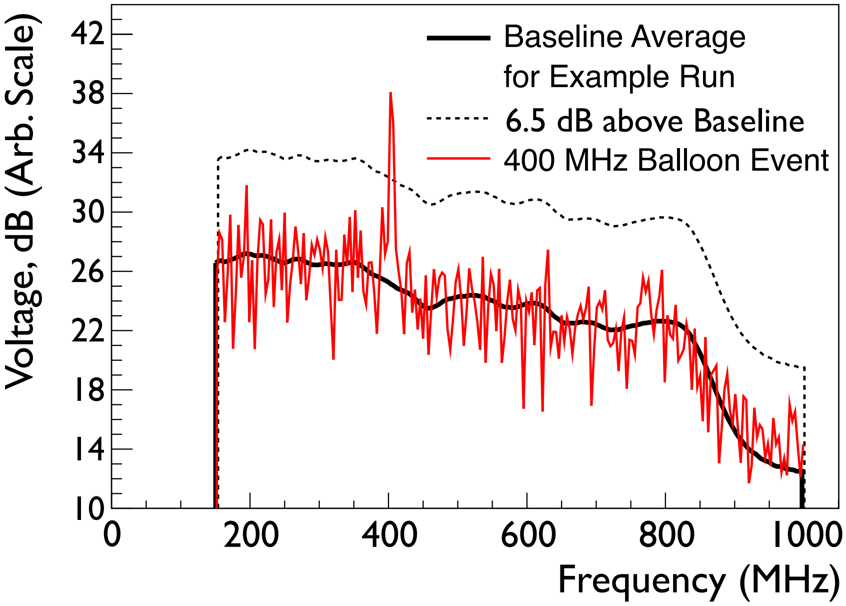

Figure 6.14: And example of CW Cut baseline and a spectrum of strong CW background event. The baseline is an average spectrum for a run data (approximately 30 minutes period of data). The example event has a strong CW background at ∼400 MHz, which is a weather balloon communication signal. The spectrum peak at 400 MHz is strong enough to exceeds the 6.5 dB above the baseline (dashed curve).

spectrum for each data run to serve as a "baseline" for comparison against individual events. Then for each channel, we compare the individual event's waveforms against the baseline. A frequency bin is flagged as containing CW if that bin in one channel exceeds 6.5 dB above the baseline, and two other channels also have a bin within 5 MHz of the first that exceeds the threshold. In order to maintain a high efficiency for neutrinos, we require that this excess is narrowband before rejecting the event. Fig. 6.14 shows an example of baseline, a 6.5 dB above the baseline, and a strong CW background event at one of the channels. We define a signal to be narrowband if less than 50% of frequency bins in a 40 MHz band around the peak are above 6.0 dB above the baseline.

Before a baseline is determined to be an acceptable representation of the average background for a given run, we examine the characteristics of the run overall to determine if it is contaminated by a large number of CW events. To do this, we calculate the maximum correlation between waveforms of neighboring events. If a significant number of CW events are found, they will be highly correlated with each other. We do not use baselines in which more than 10% of neighboring events are well correlated (contain a correlation between waveforms from any two of the same antennas between events > 0.2). In this case, we use the nearest acceptable baseline from ±10 run files (approximately ±5 hours) instead.

As a last cut, a Peak/Correlation Cut is applied. Since we expect impulsive events to exhibit a correlation between the $V_{\text{peak}}/\text{RMS}$ values from the waveforms and maximum correlation value from the reconstruction map, we designed a cut using these two values, as in [9]. CW-like events tend have high correlation values but low $V_{\text{peak}}/\text{RMS}$ values. Conversely, thermal noise events may fluctuate to high $V_{\text{peak}}/\text{RMS}$ values but not correlate well in any particular direction.

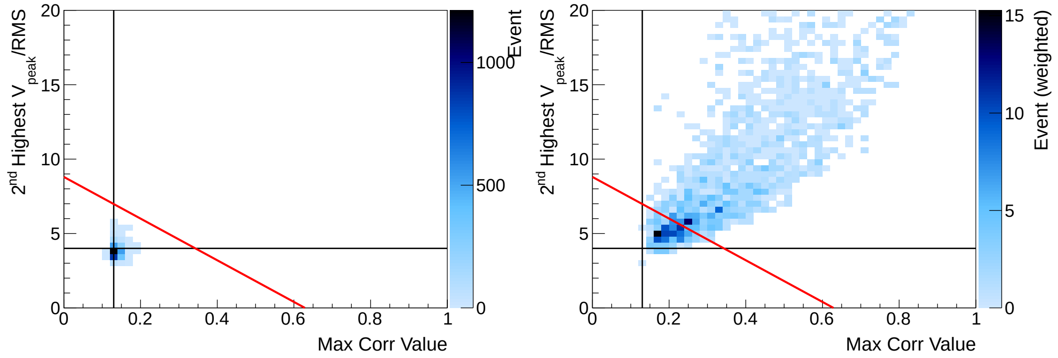

Figure 6.15: The distribution of 2nd highest V_{peak}/RMS and correlation values for the vertical polarization channel for the left plot from the 10% examination data set and the right plot from events simulated at 10^{18} eV. Both plots show only events that have survived all other cuts. The red line shows the selected cut parameter and thus all events above this line survive the cuts and those below are removed. For the data (left plot), no events fall above the cut line. For the simulated events (right plot), there is a sizable percentage of events that lie above the cut line and thus survive. These simulated events extend to a range of higher correlation and $\mathrm{V_{peak}}$/RMS values.

The Peak/Correlation Cut is based on a 2-dimensional scatter plot that has the 2^{nd} highest $\mathrm{V_{peak}}$/RMS on the vertical axis and the maximum correlation value on the horizontal axis for the corresponding polarization (see Fig. 6.15 and Fig. 6.16). The maximum correlation value is defined as the peak correlation value of a interferometric map which passed the Reconstruction Quality Cuts (for example, peak z-axis value on bottom right plot of Fig. 6.3). We choose the 2^{nd} highest $\mathrm{V_{peak}}$/RMS value from the waveforms in order to ensure that the value represents the signal strength in at least two channels and not a random fluctuation from thermal noise. First, we set constant cuts at 2^{nd} highest $\mathrm{V_{peak}}/\mathrm{RMS} > 4.0$ and maximum correlation value > 0.13. After this, we define a cut as a line on the plot of $\mathrm{V_{peak}}$/RMS vs. maximum correlation as shown in the figures. Events located to the upper right this line will pass the cut.

We choose the Peak/Correlation Cut that gives us the best expected limit on the maximal Kotera *et al.* flux model [99] (pink dot-dashed line in Figure 9). First we pick

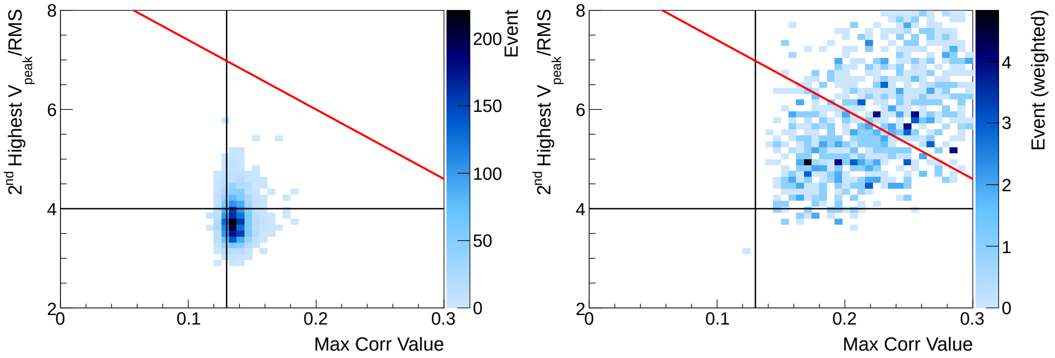

Figure 6.16: These plots are zoomed in versions of the plots above (Fig. 6.15). In the data (left plot), the events are dominated by thermal noise and thus concentrate around specific low correlation and V_{peak}/RMS values of 0.135 and 3.7, respectively. The simulated events (right plot) are dominated by the simulated signal and thus do not tend to cluster around a particular value for the correlation and signal strength.

a slope for the straight line cut (red curve in Fig. 6.15 and 6.16). We tried 20 different slope values (Fig. 6.18) and for each slope value, we obtained an exponential function fit for the expected background events. Fig. 6.17 shows the differential distribution of events from Peak/Correlation Cut slope of -14. We obtained a similar differential distribution of events and its exponential fit function for each slope value. For each cut slope, we generated 10000 toy simulation sets which have the same number of events as the Testbed data and follows the fitted exponential function's distribution. We calculated the likelihood value from each toy simulation set ($-2\log(L)$) for the exponential fit and obtain the p-value from the distribution (Fig. 6.19). Peak/Correlation Cut slope of -14 gives us a reasonable p-value at 0.235 which is close to 1σ of normal distribution. This slope choice was not a unique result but just one of the possible choices with reasonable p-value.

After the slope for the Peak/Correlation Cut is decided, we find the Peak/Correlation Cut value (vertical offset) which give us the best expected limit. We assume that there

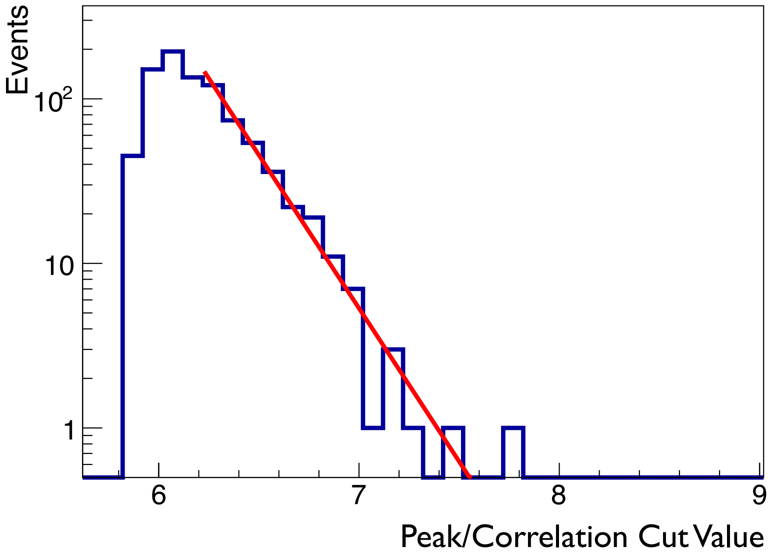

Figure 6.17: The differential distribution of events that pass the Peak/Correlation Cut using the optimal slope shown in 6.15. The horizontal axis is a measure of the vertical offset of the red line in Fig. 6.15, and is the 2nd highest V_{peak}/RMS where the red line intersects the Max Corr Value=0 axis. This distribution is fitted against an exponential function which is used to extrapolate to the number of events expected to pass the cut.

are zero signal event in the Testbed data set due to the low sensitivity to neutrinos compared to other experiments such as ANITA which didn't detect neutrino events. We use Bayesian statistics to find the upper limit on the number of neutrino events with 90% confidential level. In a poisson distribution, the likelihood to detect events is:

$$L(n|s) = \frac{(s+b)^n}{n!} e^{-(s+b)} \tag{6.3}$$

where $L(n|s)$ is the likelihood to detect n events with s mean signal events expected, and b is the expected number of background events. Therefore, we let $n = b$ in Eq. 6.3. With 90% confidence level, the upper limit on the number of signal events can be obtained by:

$$1 - \alpha = \int_0^{S_{up}} p(s|n)ds = \frac{\int_0^{S_{up}} L(n|s)ds}{\int_0^{\infty} L(n|s)ds} \tag{6.4}$$

where $1 - \alpha$ is the confidence level ($1 - \alpha = 0.9$ for 90% C.L.), S_{up} is the maximum allowed signal events, and $p(s|n)$ is the probability to have mean signal events s when we detected n events from the experiment. From Eq. 6.4, we can obtain S_{up} for each Peak/Correlation Cut value.

The Peak/Correlation Cut value which give us the best limit is determined from:

$$S_{up} = N = f \times \sum A_{eff,i} \cdot T_{live} \cdot F_i \cdot \Delta E \tag{6.5}$$

where N is expected neutrino events with a factor f applied to our detector's sensitivity, $A_{eff,i}$ is a effective area at energy bin i, T_{live} is a livetime of the detector, F is a flux at energy bin i, ΔE is the energy bin size, and f is a constant factor applied to our detector to have S_{up} expected neutrino events from the detector. The best

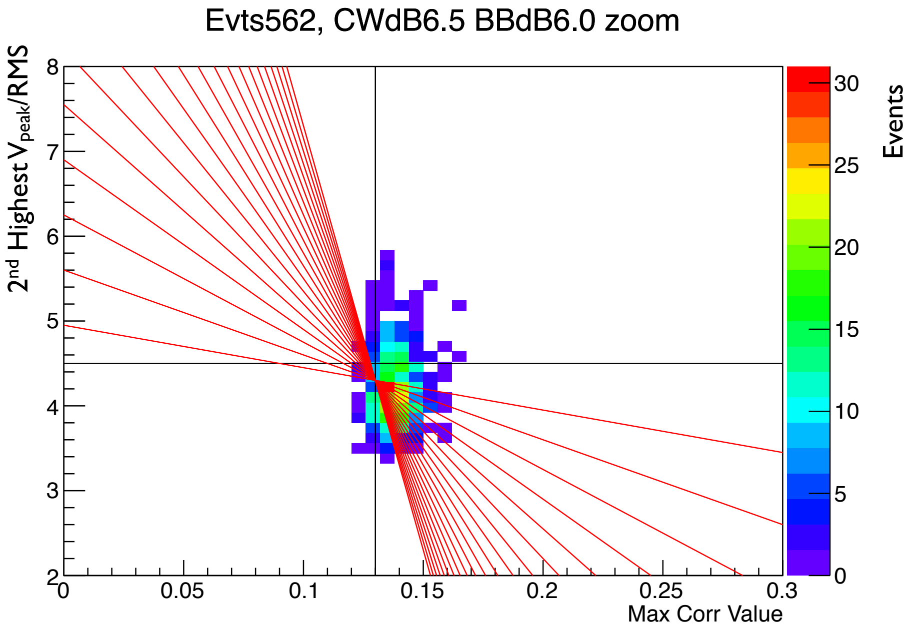

Figure 6.18: Plot showing the Peak/Correlation Cut for each trial slopes. Among all 20 slopes, we choose a slope of -14 which give us a reasonable p-value from the corresponding toy simulation set (see Fig. 6.19).

limit is achieved when we have maximum $1/f = N/S_{up}$ (or minimum $f = S_{up}/N$). Fig. 6.20 shows how we found the optimized Peak/Correlation Cut value to be 8.8 where N/S_{up} is maximum.

6.2.3 Background Estimation

To estimate the background, we use the 10% data set and fit the differential number of events rejected by the Peak/Correlation cut as a function of the vertical offset to an exponential function, shown in Fig. 6.17. We use the fit function $N_{\text{diff}} = e^{a\cdot x+b}$ where x is the 2nd highest $\mathrm{V_{peak}}$/RMS where Max Corr Value=0, N_{diff} is the differential number of events rejected by the Peak/Correlation cut when it is vertically

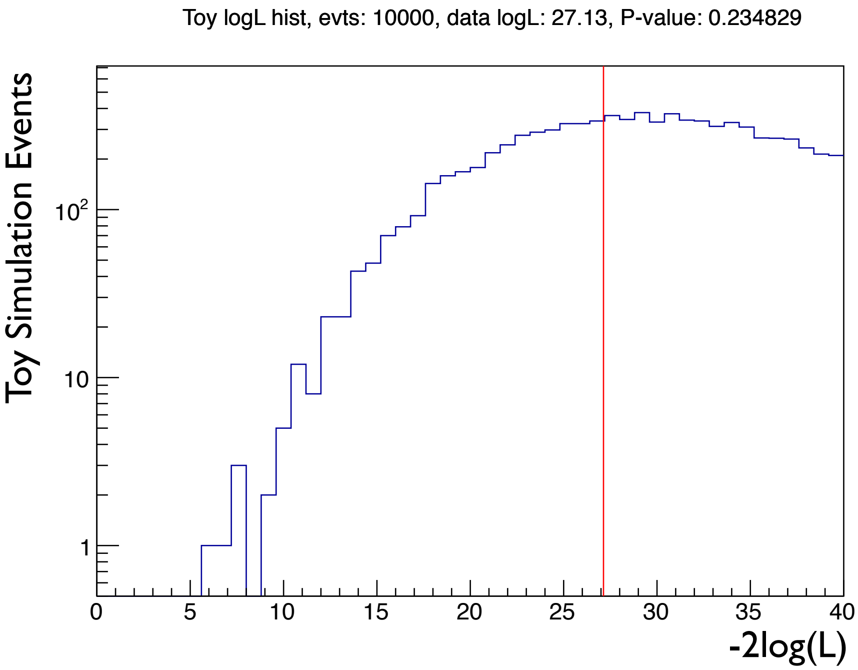

Figure 6.19: Distribution of minimum log likelihood from the toy simulation set with Peak/Correlation Cut slope of -14. The red vertical line is the value from the Testbed data set. The p-value is the ratio between the total number in the toy simulation set to the number in the toy simulation set that has a smaller $-2\log(L)$ value than the one from the Testbed data. A p-value of 0.235 is close to 1σ for a normal distribution.

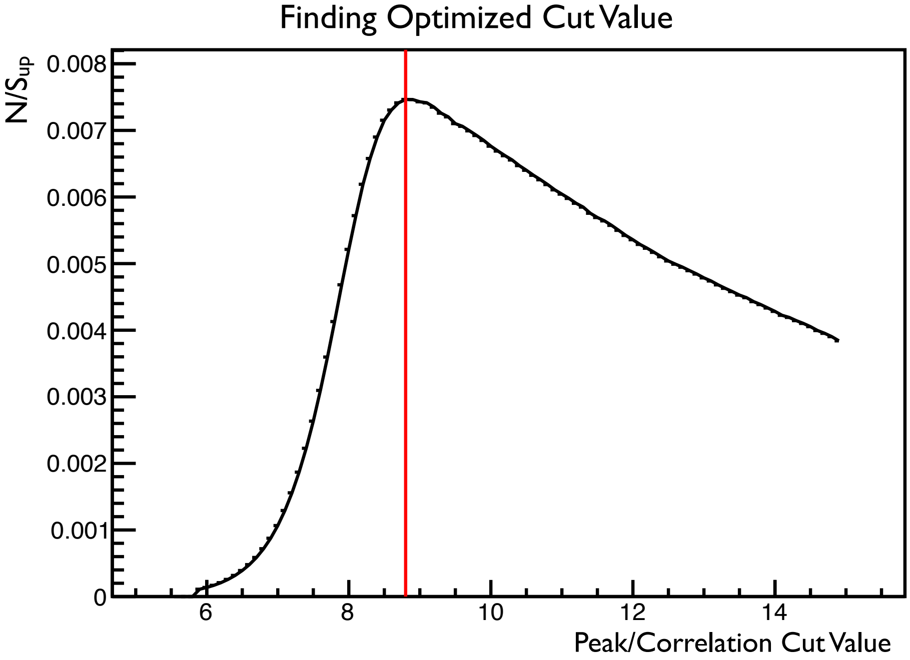

Figure 6.20: Finding the optimal Peak/Correlation Cut value by maximizing N/S_{up}. The red vertical line is the optimal Peak/Correlation Cut value (intercept in 2nd highest V_{peak}/RMS in Fig. 6.15 and 6.16) which is 8.8. Peak/Correlation Cut values smaller than the optimal value are too weak so allow too many background events. Peak/Correlation Cut values bigger than the optimized value are, on the other hand, too stringent and reject too many neutrino events.

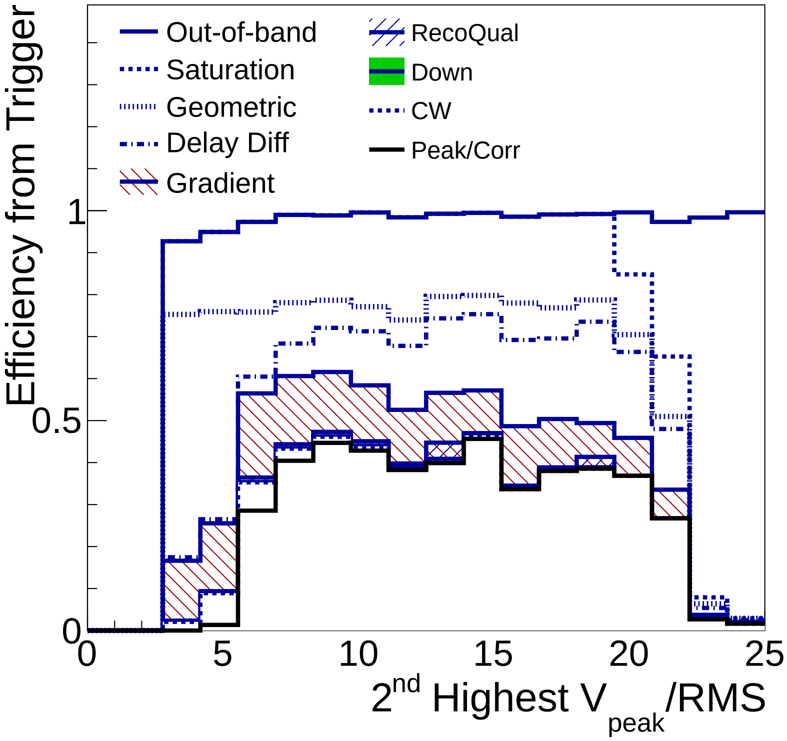

Figure 6.21: The efficiency of each cut in sequence compared with the total number of triggered events for a simulated data set generated from an optimistic Kotera *et al.* 2010 flux model. After the cuts designed to reject thermal background are applied (beginning with the Delay Difference Cut), the efficiency turns on and plateaus for 2^{nd} highest $\mathrm{V_{peak}/RMS} > 6$.

offset by dx, and a and b are two fit parameters in the exponential function. From the fit, we obtained $a = -4.29 \pm 0.26$ and $b = 31.70 \pm 1.67$ where the deviation of each parameter is the one sigma error from the best fit result. The optimal cut gives us 0.06 estimated background events and 0.02 expected neutrino events from the maximal Kotera *et al.* flux model in the 90% data set in the Stage 2 analysis.

Fig. 6.21 shows the efficiencies of each analysis cut in sequence for triggered events as modeled in AraSim for the Interferometric Map analysis. For this plot, we use the 2^{nd} highest $\mathrm{V_{peak}/RMS}$ on the horizontal axis as in the Peak/Correlation Cut. The analysis efficiency for the maximal Kotera *et al.* flux model is ∼ 40 % for signal strengths between 7 and 20 in 2nd highest V_{peak}/RMS. The first noticeable cut on the plot is the Saturation Cut which rejects most of events above 20 V_{peak}/RMS signal strength. After that, the Geometric Cuts reject ∼ 20% of the events mostly due to the SPS Geometric Cut and are consistent across all signal strengths. The Delay Difference Cut and the Reconstruction Quality Cut reject poorly reconstructing events, bringing the efficiencies to the ∼ 40 % for high SNR. The remaining cuts, such as the Down, CW and Peak/Correlation Cuts, don't significantly affect the total efficiencies.

6.3 Survived Events

In Stage 1 of the analysis, we had three events survive all cuts from 0.0285 expected background events and 0.00362 expected neutrino events. These three events were all believed to be known types of anthropogenic impulsive events ("200 MHz" and "Near Surface" type events). Among them, one event appears to be a "200 MHz" type event, and we had intended to reject those with the Gradient Cut and so this cut was modified slightly to better match the pattern that it was trying to identify. The original definition of the cut required that the highest V_{peak}/RMS value came from a VPol channel before the gradient condition was checked for the event. Through what appears to be an aberrant single-bin fluctuation, this event had its highest V_{peak}/RMS in an HPol channel. Since the requirement that the highest V_{peak}/RMS value be from a VPol channel is not a necessary condition for the pattern recognition, it was removed from the definition of the cut. The altered cut just checks that the gradient among the VPol channels matches the pattern and using this adjusted definition, the event was then rejected.

Remaining two survived events are rejected by alternating the Geometric Cut regions. The Geometric Cut region for "200 MHz" and "Near Surface" type events in Stage 1 analysis was initially defined as a box which contains all those type events from 10% data set. The altered "200 MHz" and "Near Surface" Geometric Cuts were defined by Gaussian fits to the azimuth and zenith distributions of the events with only the Event Quality, Reconstruction Quality Cut, Delay Difference and CW Cuts applied (See Fig. 6.22). The edges of each cut region were defined by the criterion that one would expect a total of 0.04 background events to reconstruct outside the region based on this Gaussian fit with only these four cuts applied. This modification increased the total size of the Geometric Cut area, including the SPS, Calibration Pulser, and Clustering Cuts, by $\sim$ 14%. After these modifications, zero neutrino candidate events survived from Stage 1 analysis.

Using these new Geometric Cut regions, two events survived from Stage 2 analysis. These two events that passed were again leaked anthropogenic impulsive events that were intended to be rejected by the "200 MHz" Geometric Cut (See the bottom plot on Fig. 6.22) and thus were removed by slightly expanding the Geometric Cut region in the 3 km map. The alterations to the Geometric Cut regions increase the total acceptance of the Geometric Cut (which includes the South Pole region) by less than 5%. After these modifications, zero neutrino candidate events survived. In future analyses, we plan to design cuts to reject these type of events by other means, with less reliance on the Geometric Cuts.

6.4 Livetime Calculation

A livetime is obtained for each analysis, defined as the total amount of time covered by the data set where the trigger is available, excluding any periods of time that were rejected by the analysis.

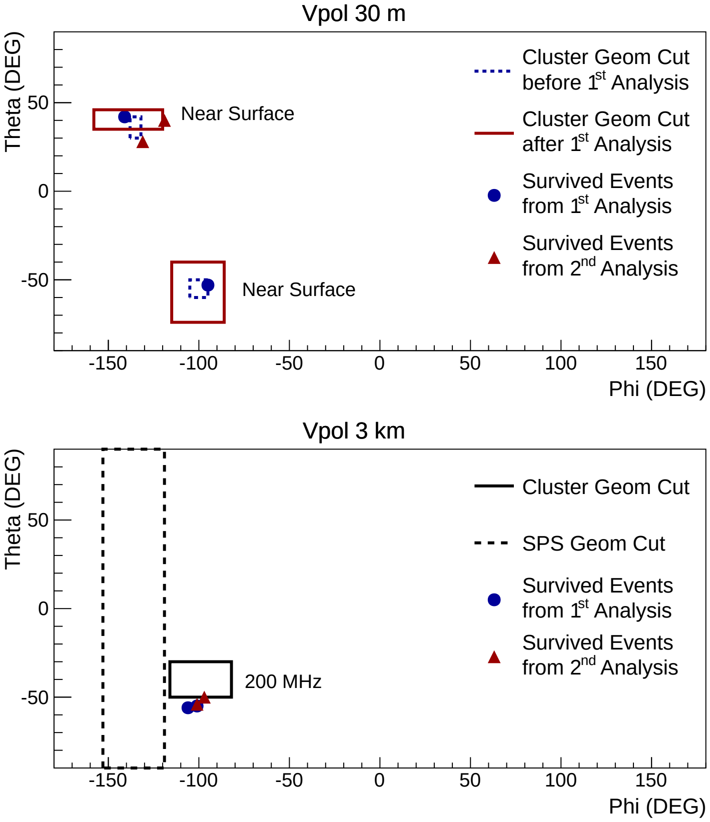

Figure 6.22: The reconstruction directions of the events that passed both Stage 1 and Stage 2 of the analysis in the 30 m (upper) and 3 km (lower) maps. Events that passed the unaltered cuts in Stage 1 are shown in blue and those that passed the Stage 2 cuts are shown in red. The initial Geometric Cut regions (dashed blue line) were adjusted after Stage 1 (solid red lines) based on a Gaussian fit to the background event distribution with a limited set of cuts applied.

For each analysis, the trigger deadtime is calculated by accumulating the number of 10 MHz clock cycles N_c during one GPS second when the trigger was not available due to the waveform readout process after the trigger or any other issue that would cause the Testbed to be unable to trigger. This counted number of clock cycles N_c gives us the livetime fraction of that second as $1 - N_c/10^7$. The total livetime of the Testbed is obtained by accumulating the livetime fraction from each second over the entire data set while avoiding double counting of the livetime from same GPS second. If any second has a deadtime $> 10\%$, the entire second is rejected.

We conservatively reject the events from October 22$^{\text{nd}}$ to February 16$^{\text{th}}$ for both 2011 and 2012 data set which is the summer season at the South Pole. Additionally, the calibration pulser timing cut reduces the livetime by $\sim 8\%$. This strict timing cut requirement will be able to be relaxed in future analyses. The CW Cut also requires the identification of a good baseline and if this baseline is not found in a nearby time period, that run period is rejected. This requirement reduces the livetime by $\sim 15\%$ but better CW analysis techniques will be able to remove this requirement as well. The overall livetime from the 2011-2012 Testbed data is 224 days.

6.5 Results

No neutrino candidate events were found and the results from this analysis are used to derive constraints on the neutrino flux.

The effect of the successive cuts in Stage 2 of the Interferometric Map Analysis is summarized in Table 6.1. After the Event Quality and the Reconstruction Quality Cuts are applied, for this table the events are examined in HPol and VPol channels separately. While a single event can pass the HPol and VPol Reconstruction Quality Cut simultaneously and be considered in both channels, only a small number of events (~ 100) did so.

After finding no neutrino candidate events passing all cuts, we set limits on the neutrino flux given the effective volume of the Testbed derived from AraSim and the total livetime of the period examined. The effective volume, V_{eff}, is found for each

Total	3.3E8			
Cut	Number passing (either polarization)			
Event Qual. Recon. Qual.	1.6E8 3.3E6			
	VPol		HPol	
	Rejected		Rejected	
	In sequence	as last cut	In sequence	as last cut
Recon. Qual.	1.8E6		1.4E6	
SP Active Period	1.4E6	125	1.1E6	13
Deadtime < 0.9	1.4E6	0	1.1E6	0
Saturation	1.4E6	0	1.1E6	0
Geometric, except SP	1.3E6	7	1.0E6	0
SP Geometric	1.1E6	0	9.0E5	1
Gradient	1.1E6	0	9.0E5	0
Delay Difference	1.8E5	0	1.5E5	0
CW	1.8E5	0	1.4E5	1
Down	1.7E4	15	1.9E4	1
V_{peak}/Corr	**0**	1.7E4	**0**	1.9E4

Table 6.1: This table summarizes the number of events passing each cut in the Interferometric Map Analysis, in Phase 2 (2011-2012, excluding Feb.-June 2012). We list how many events survive after each cut in sequence and how many events each cut rejects as a last cut. After the Event Quality and Reconstruction Quality Cuts are applied, VPol and HPol and considered as two separate channels for the purpose of tabulation, independent of one another.

energy bin by simulating a large number ($\sim 10^6$) of events:

$$V_{\text{eff}} = \frac{V_{\text{cylinder}}}{N} \sum_{i=1}^{N_{\text{passed}}} w_{\text{i}}. \tag{6.6}$$

Each event is given a weight w_{i} equal to the probability that the neutrino was not absorbed in the earth, given its direction and position of the interaction. Then $\sum\limits_{i=1}^{N_{\text{passed}}} w_{\text{i}}$ is the weighted sum of the number of events that triggered and passed all analysis cuts, and N is the total number of events thrown. The neutrino interactions are thrown in a cylindrical volume centered around the detector, denoted V_{cylinder}.

The effective area is then calculated from the effective volume by the following:

$$A_{\text{eff}} \approx \frac{V_{\text{eff}}}{l_{\text{interaction}}} \tag{6.7}$$

where $l_{\text{interaction}}$ is the interaction length.

The 90% differential flux limit on the number of events in each decade in energy then be calculated from this equation:

$$E\ F(E) = \frac{1}{4\pi A_{\text{eff}} T} \frac{2.3}{\ln(10)} \tag{6.8}$$

where T is the total livetime of the examined period, the factor of 2.3 is the 90% Poisson confidence level upper limit on number of expected signal events with zero events observed, and the ln(10) is a correction factor for the log-scale binning. Using 2.3 as a number of detected events from the flux $F(E)$ in ΔE bin, we can let:

$$\begin{aligned} 2.3 &= F(E) \cdot A_{\text{eff}} 4\pi T \cdot \Delta E && (6.9) \\ &= E\ F(E) \cdot A_{\text{eff}} 4\pi T \cdot \frac{\Delta E}{E} && (6.10) \\ &= E\ F(E) \cdot A_{\text{eff}} 4\pi T \cdot \Delta \ln(E) && (6.11) \\ &= E\ F(E) \cdot A_{\text{eff}} 4\pi T \cdot \ln(10) \Delta \log(E). && (6.12) \end{aligned}$$

We set our limit at 2.3 events in one decade of energy ($\Delta \log(E) = 1$) and obtained Eq. 6.8. Fig. 6.23 shows the limit obtained from our Testbed with 224 days of livetime. The projected limits for ARA37 shown in Fig. 6.23 are derived from trigger-level sensitivities only, with 100% analysis efficiencies assumed for simplicity.

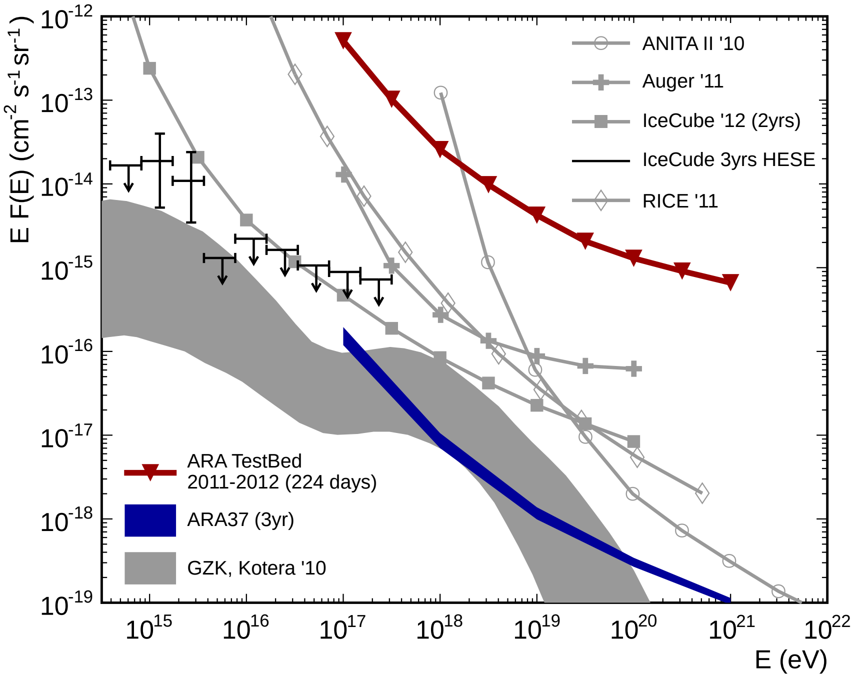

Figure 6.23: The limits placed compared with the projected ARA37 trigger-level sensitivity and results from other experiments.

6.6 Systematic Uncertainties

In this section, we will discuss the systematic uncertainties in the Interferometric Map Analysis. We considered systematic uncertainties in both the background estimation and analysis efficiency. While the uncertainty on our background estimation is derived solely from the errors on the best fit line used to extrapolate the background estimate described in Section 6.2.3, for the analysis efficiency we consider the effect of the antenna model, ice index of refraction model, ice attenuation model, and neutrino cross section model. Each systematic error is obtained by changing only one parameter value at a time from the default and estimating the impact on the result from each.

The systematic uncertainty on the background estimation is derived from the errors on the best fit exponential function used in the extrapolation described in Section 6.2.3. Recall that the best fit to $N_{\text{diff}} = e^{a \cdot x + b}$ gave $a = -4.29 \pm 0.26$ and $b = 31.70 \pm 1.67$. We moved each fit parameter alone by one standard deviation in both the positive and negative directions, and obtained the maximum deviation in the background estimate in each direction. We find the number of background events to be $0.06\ ^{+0.52}_{-0.05}$ events in the 90% data set in the Stage 2 analysis.

Modeling the expected frequency-dependent phases of the neutrino-induced measured pulses contributes an important systematic error to our analysis efficiencies. We use two different techniques for modeling the phases, and they put upper and lower bounds on our limit and projected sensitivity for ARA37, which are based on our current trigger and given the effects so far included in our simulations. Conservatively, our main result in this paper (the red line in Fig. 6.23) uses our default model, while we believe that a more accurate model would give an improved limit.

We model the phase of a received pulse from a neutrino interaction using two different methods, the first being the default and the second for comparison. We believe that the "true" phases would give a result that is in between the two. The first, default approach models the frequency-dependent phase of the RF emission, as well as the phase response of antennas, filters and amplifiers as described in Chapter 5. The second model for the phase, used for comparison, is quite simplistic, with the phase of the radio emission being +90° for positive frequencies and -90° for negative frequencies, and the phase response of antennas and electronics being flat.

While the second, simple model of the phase response produces a received pulse that is too narrow, we have found by comparing simulated and measured calibration pulser waveforms that our default method simulates pulses that are too broad (see Fig. 6.24). The narrow pulses from the second method result in analysis efficiencies that are too high, and the broader pulses from the default method fail our cuts more often than they should. This excessive broadening of the pulse is believed to be dominated by the antenna response model, and future measurements of the phase response of our antennas are expected to greatly reduce this systematic uncertainty.

The second model gives a trigger level sensitivity that is approximately 65% larger than the first model at 10^{17} eV, 50% larger at 10^{18} eV and 20% larger at the highest energy simulated, 10^{21} eV. At low energies, the dispersion of the signal has a more dramatic effect on the trigger efficiency whereas at higher energies the dispersion has less of an effect due to the the strength of the signal.

The choice of model for the depth dependence of the index of refraction in the firn, both for event generation and for event reconstruction, provides another source of systematic uncertainty in our analysis efficiency since it determines the path taken through the ice and the arrival direction at the antennas, and also impacts the interferometric maps that are used in analysis. By default, we used the exponential fit

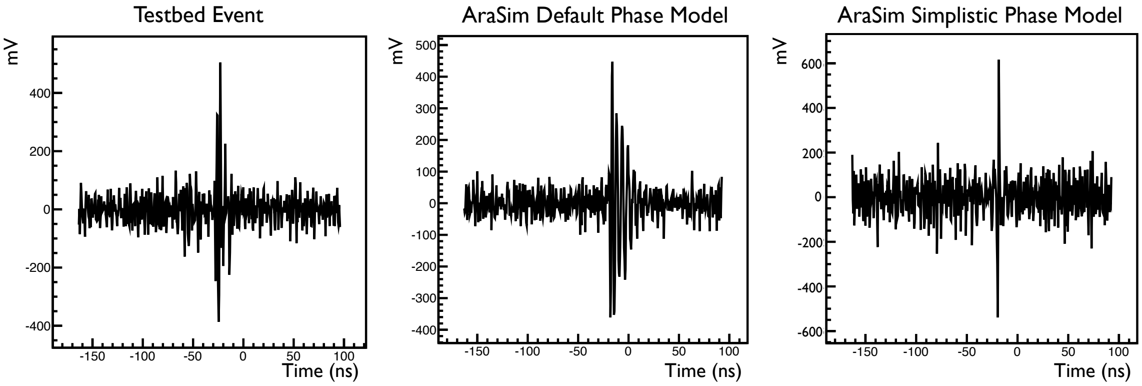

Figure 6.24: Channel 0 waveform from a calibration pulser event. The left plot is from the Testbed data, the middle plot is from AraSim with default phase model, and the right plot is from AraSim with simplistic ±90° phase model. Even though the amplitude of the waveforms in two AraSim plots are not calibrated to the Testbed, we can see that the pulse in the simplistic phase model is too narrow while the pulse in the default phase model is too broad compared to the Testbed waveform.

function for the index of refraction as a function of depth:

$$n(z) = 1.78 - 0.43 \cdot e^{-0.0132 \cdot z} \tag{6.13}$$

where n is the index of refraction and z the depth of ice (positive value for deeper location). The alternative index of refraction model we tested was an inverse exponential fit function:

$$n(z) = 0.92 + \frac{0.86}{1 + e^{-0.0132 \cdot z}}. \tag{6.14}$$

Both functions gives an index of refraction of 1.35 at the surface and 1.78 in deep ice. The exponential model has a more shallow firn layer ($\sim$ 200 m) compared to the inverse exponential model ($\sim$ 250 m), and thus shows a more dramatic change in index of refraction as a function of depth. The exponential model is chosen as the default since it fits better with measurements [71], and we use the same model for both event generation and reconstruction in the analysis.

This strategy of course assumes perfect knowledge of the index of refraction when carrying out the reconstruction. In order to estimate the systematic error due to imperfect knowledge of the depth-dependence of the ice, we try using each of the two models for event reconstruction and/or reconstruction, giving four combinations including the default combination, and find the largest excursions from the baseline result in either direction. We find the efficiency can increase by 4.9% or decrease by 16.4% at $E_\nu = 10^{18}$ eV compared to the default due to imperfect knowledge of the depth-dependence of the index of refraction in ice.

Likewise, we assess the systematic uncertainty due to in-ice field attenuation by comparing our results when two different models are used. The default model uses a South Pole temperature profile from [73] folded in with a relationship between field attenuation length and ice temperature given in [74] as used in ANITA simulations and described in [75]. The alternative ice attenuation length model is based on the ARA Testbed measurement from IceCube deep pulser events published in [31].

By default, our modeling of the effect of ice attenuation is based on ANITA simulations [75], where profiles of ice attenuation vs. depth are considered, and for each event, the ice attenuation length is averaged over depth from the neutrino-ice interaction location to the surface and the result is denoted $\langle L_{\mathrm{atten}} \rangle$. The attenuation length is assumed to remain a constant $\langle L_{\mathrm{atten}} \rangle$ over the entire path of the ray in the ice, and an ice attenuation factor,

$$F^{\mathrm{total}}_{\mathrm{IceAtten,default}} = e^{-D_{\mathrm{travel}}/\langle L_{\mathrm{atten}} \rangle}, \tag{6.15}$$

is then applied to the electric field. Here, $F^{\text{total}}_{\text{IceAtten,default}}$ is the ice attenuation factor and D_{travel} is the ray travel distance between the neutrino-ice interaction location and the antenna.

The second calculates the total attenuation factor every few 10 m along the path of the ray for each event, and uses the ice attenuation lengths measured by the ARA Testbed [31]. The total ice attenuation factor from this method is then:

$$F^{\text{total}}_{\text{IceAtten,alter}} = \prod_{i=1}^{N} e^{-D_{\text{i}}/L_{\text{atten}}(z_i)} \tag{6.16}$$

where $F^{\text{total}}_{\text{IceAtten,alter}}$ is the ice attenuation factor applied to the electric field strength from the alternative model, N is the total number of ray tracing steps from the neutrino-ice interaction location to the antenna, D_{i} is the ray travel distance for the corresponding ray trace step i, and $L_{\text{atten}}(z_i)$ the ice attenuation length at a corresponding ray tracing step's depth z_i. Due to the fact that the second technique gives us longer attenuation lengths near the surface, it gives a $\sim 10\%$ larger efficiency at $E_\nu = 10^{18}$ eV compared to the default model.

Finally, we estimate the uncertainty due to our $\nu - N$ cross section model. The νN cross section model in our simulation is from Connolly *et al.* [68] which gives us the central values and upper and lower bounds for the $\nu - N$ cross section as a function of ν energy. At $E_\nu = 10^{18}$ eV, the uncertainty in the $\nu - N$ cross section give us up to $\sim 30\%$ variance from the central value (from the upper bound on the neutral current cross section). A higher cross section will lower the sensitivity due to the increased Earth screening effect. However, there's also a counter effect from a higher cross section which increases the probability to interact between neutrino and nucleon in the ice, and thus increases the sensitivity. At 10^{18} eV, the lower bound on the νN cross section gave a $\sim 6.2\%$ higher neutrino efficiency while the upper bound

Systematic uncertainties at 10^{18} eV	+ (%)	− (%)
Index of Refraction	4.9	16.4
Ice Attenuation Length	10.2	N/A
νN Cross Section	6.2	N/A
Phase Response	50.9	N/A
Total	52.5	16.4

Table 6.2: Summary of systematic uncertainties on the neutrino efficiency at 10^{18} eV.

From the Testbed to ARA37 at 10^{18} eV

	$A\Omega_{\text{eff}}$ [km^2sr]	Accumulative factor
Testbed analysis	2.8E-4	1
Testbed trigger	1.5E-3	5
ARA one-station trigger	4.0E-3	14
ARA37 trigger	1.3E-1	464

Table 6.3: Factors that bring the Testbed sensitivity to ARA37 sensitivity for $E_\nu = 10^{18}$ eV using AraSim.

on the νN cross section gives a negligible change to the efficiency in comparison to the baseline model.

Overall, we estimate that we expect $0.06 + 0.52 - 0.05$ background events with uncertainties of +52.5% and −16.4% on our neutrino efficiency.

6.7 Projections for ARA3 and ARA37

The ARA collaboration aims to build an array of 37 stations to gain enough sensitivity to measure of order 100 UHE neutrinos and exploit the physics and astrophysics information that they carry. In this section we illustrate the factors that bring us from the sensitivity of this Testbed analysis to the expected ARA37 trigger sensitivity

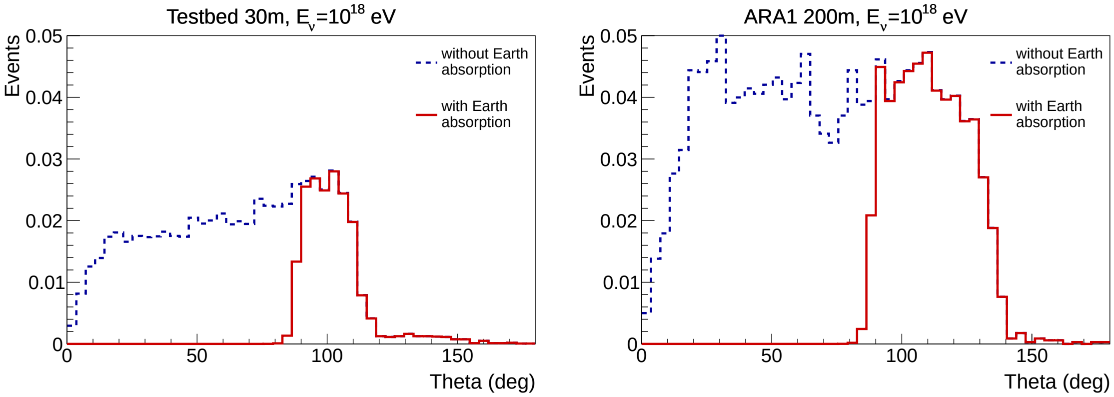

Figure 6.25: These figures show the distribution of zenith angles of incident momenta for simulated neutrinos at 10^{18} eV that pass the trigger in AraSim for (left plot) Testbed at 30 m and (right plot) a design station at a depth of 200 m. Events on the left side of each plot come from up-going neutrinos with respect to the South Pole, while events on the right come from down-going neutrinos. The viewable arrival direction zenith angles are generally limited to less than 120° for the Testbed and less than 150° for a design station. This limited range of observable arrival directions is due to the combination of the limited viewing region seen in Fig. 5.3 and the requirement that the coherent signal is emitted near the Cherenkov angle, which is relative to the arrival direction. When one adds in the screening effect of the Earth (red lines), almost all events with zenith angles less than 90° disappear as well and thus the observable range of zenith angles is limited by the geometry of the Testbed by a factor of about 2.

in Fig. 6.23. For future detector configurations we compare sensitivities at the trigger level only. We do not know what our analysis efficiencies will be at those stages but expect that they will improve.

Table 6.3 lists the factors that bring the Testbed sensitivity in this paper to that expected for an ARA37 array at $E_\nu = 10^{18}$ eV, where, for many cosmogenic neutrino flux models, we expect to measure the largest number of neutrinos. The factors in Table 6.3 are all derived from the AraSim simulation and we use the effective area× solid angle $A\Omega_{\text{eff}}$ as the figure of merit to compare the sensitivity of the detector at different stages. The effective area at the Testbed trigger level is a factor of 5 higher than at the analysis level at 10^{18} eV. Going from the Testbed trigger level to an ARA deep station, we find a factor of 3.2 improvement in sensitivity. This is both because a shallow station is limited in the angle of incident RF emission that it can observe, and also because neutrinos steep enough to produce observable RF emission are subject to more earth absorption (see Fig. 6.25). From one ARA station to ARA37, the sensitivity scales as the number of stations since at these energies, events tend to be seen by only one station and each station serves as its own independent detector.

In addition to the improvements in sensitivity expected from increasing the number of deep stations as listed in Table 6.3, we expect that our livetime, analysis efficiencies, and background rejection will all improve in the next neutrino searches in deep stations. Future improvements to the trigger (from a 3/8 coincidence to one based on pattern recognition, for example) will improve how efficiently we record neutrino signals in the first place.

Livetime improvements will come from two factors. The A2 and A3 stations have been running since February 2013 with $\sim 95\%$ livetime, without the intermittent periods of deadtime we encountered with the Testbed. In addition, we expect to be able to remove the cut on the period when the South Pole is active and recover 3 months per year of livetime. We find that the number of events rejected by the cut on the period of South Pole activity (125 VPol, 13 HPol) is manageable and at a level that we can reasonably expect to reject by other means. Also A2 and A3 data will not have as strong anthropogenic backgrounds as Testbed 2011-2012 data set during the summer season at the South Pole since the full IceCube 86 strings have finished deploying. Note that only one event in Table 6.1 was rejected by the SP Geometric Cut and not rejected by any other cut.

Another expected improvement from A2 and A3 is the increased field-of-view from SP Geometric Cut. As the Testbed is the closest station to the SP station and

IceCube array, the increase distance from SP station and IceCube array to A2 and A3 make the size of the SP Geometric Cut smaller than the Testbed. In case we use the same definition of the SP Geometric Cut, A2 and A3 will have ∼44% of SP Geometric Cut region compared with the Testbed. Therefore we expect to have approximately 10% improvement in the analysis efficiency from the new SP Geometric Cut for A2 and A3.

We expect analysis efficiencies for deep stations to improve compared to the Testbed due to the better uniformity of deep ice, the increased number of borehole antennas (four to eight), and analysis experience. The deep ice and increased number of antennas bring improved event reconstructions. This leads to improved rejection of backgrounds (which allows for looser analysis cuts) and a higher maximum correlation value for improved separation between signals and noise.

Chapter 7

Gamma-Ray Burst Neutrino Search

The contents of this chapter are in progress to be published.

We searched for ultra-high energy (UHE) neutrinos from Gamma-Ray Burst (GRB) with the Askaryan Radio Array (ARA) Testbed station's 2011-2012 data set. Among ~ 600 GRBs monitored by the Gamma-Ray Coordinate Network (GCN) catalog from Jan. 2011 to Dec. 2012, 57 GRBs were selected to be analyzed. These GRBs were chosen because they occurred during a period of low anthropogenic background and high stability of the station, and fell within our geometric acceptance. We searched for UHE neutrinos from 57 GRBs and observed 0 events, which is consistent with 0.106 estimated background events. With this result, we set the limits on the UHE GRB neutrino fluence and quasi-diffuse flux from 10^{16} to 10^{19} eV. This is the first limit on the UHE GRB neutrino quasi-diffuse flux limit at energies above 10^{16} eV.

7.1 Introduction

As Gamma-Ray Bursts (GRBs) are among the most energetic events in the universe, GRBs are candidates for the sources of UHECRs and neutrinos [100, 101]. In the standard Fireball shock model, relativistic plasma in the series of jets produce high energy gamma-rays from synchrotron radiation and inverse Compton scattering inside the jet. Neutrinos will be also produced via $p-\gamma$ interactions from gamma-rays and protons that are accelerated in a jet through the shock acceleration [102].

So far many experiments have searched for neutrinos from GRBs using different techniques [103–105], but most of these experiments are sensitive at energies lower than 10^{18} eV. In this paper, we present the fluence limit from 57 selected GRBs and the first limit on the UHE GRB neutrino quasi-diffuse flux from 10^{16} to 10^{19} eV. GRB neutrino fluences are obtained from Neutrinos from Cosmic Accelerators (NeuCosmA), a full numerical calculation software package [106] using parameter values from the Gamma-Ray Coordinate Network (GCN) catalog [107].

7.2 Previous GRB Neutrino Analyses

There are multiple UHE or very-high energy (VHE) GRB neutrino searches from IceCube [103], ANTARES [104], and ANITA [105] and they are complementary. IceCube uses the optical Cherenkov technique, located at the South Pole (Southern hemisphere) and searches up-going neutrinos. Recently IceCube reported the most stringent GRB neutrino limit from 10^{14} to 10^{16} eV (the VHE region) [103]. An IceCube GRB neutrino search, previously using a Waxman-Bahcall (WB) GRB neutrino flux model [108] has been updated to a new result using a numerical GRB neutrino flux model [103]. ANTARES is an optical Cherenkov experiment similar to IceCube but located in the Mediterranean Sea and therefore uses water as a detection medium. As ANTARES is located at Northern hemisphere, the field of view of IceCube and ANTARES do not overlap significantly. Using the same optical Cherenkov technique, ANTARES is sensitive to a similar region of neutrino energy as IceCube. ANTARES's GRB neutrino analysis is based on NeuCosmA, a numerical GRB neutrino flux model [106], and its GRB neutrino flux limit is approximately an order of magnitude weaker than the limit from IceCube [109].

ANITA is a balloon-born Antarctic experiment that uses the radio Cherenkov technique. At its $\sim$ 37 km altitude, ANITA can monitor an extremely large volume of Antarctic ice ($\sim$ 1.6Mkm^3 at once [9]). Although ANITA provided the first GRB neutrino limit in the UHE region, there are some limitations. First, the ANITA GRB neutrino analysis was based on a simple model that used an E^{-4} spectrum, which is based on the analytic WB GRB neutrino flux model [54]. The GRB neutrino fluence from the WB model shows approximately an order of magnitude difference when compared to numerical calculation models such as NeuCosmA [106]. Secondly, the $\sim$ 30 day livetime of a balloon experiment limits the number of analyzable GRBs to approximately 30 events as GRBs occur $\sim$ once per day. Compared to the ANITA analysis, our analysis uses the NeuCosmA package to obtain GRB neutrino fluences and benefits from a 224 day livetime [2].

7.3 The ARA Instrument

The full proposed ARA detector would consist of 37 stations spaced 2 km apart at a depth of 200 m. The first three design ARA stations were deployed in the 2011-2012 and 2012-2013 seasons, while an ARA prototype TestBed station, which we use for this GRB neutrino search, was deployed in the 2010-2011 season [2].

7.3.1 TestBed station

The ARA TestBed station is a prototype station of ARA detector. It contains 16 antennas: four bicone vertically polarized (Vpol) antennas, four bowtie-slotted cylinder horizontally polarized (Hpol) antennas, two discone Vpol antennas, two batwing Hpol antennas, two quad-slotted cylinder Hpol antennas and two surface located antennas. Most of the components in the TestBed are similar to the ARA stations.

However, the maximum depth of the borehole antennas in the TestBed is approximately 30 m while ARA design stations are at 200 m depth. Each borehole in the TestBed has one Vpol and one Hpol antenna with bandwidth from 150 MHz to 1 GHz. A more detailed description about ARA Testbed can be found in [2, 31].

7.4 Analysis Tools

In order to get the expected neutrino spectra and the ARA Testbed efficiency for GRB neutrinos, we use NeuCosmA GRB neutrino model and AraSim, the ARA detector simulation software. Highlights for NeuCosmA and AraSim are described in the following sections.

7.4.1 GRB Neutrino Model: NeuCosmA

NeuCosmA is a Monte Carlo GRB neutrino fluence calculation code. It provides detailed calculations for primary pions, kaons and secondary particles production modes using current Standard Model particle physics as shown in [14]. These detailed calculations in NeuCosmA yield a significant difference in the neutrino flux by an order of magnitude compared to the full analytic WB model and add spectral shape content to the neutrino flux (Fig. 7.1). We expect NeuCosmA to deliver more reliable GRB neutrino fluences compared to analytic models.

NeuCosmA uses measured parameter values such as T_{90}, the time in which 90 % of the fluence is emitted, α and β, the first and second gamma-ray spectral indexes, and redshift z in order to obtain the neutrino spectrum that is consistent with a measured gamma-ray spectrum. We use parameter values for each GRB taken from the Gamma-Ray Coordinate Network (GCN) catalog. If some of the parameter values are missing for a GRB, default values are used instead. The GCN catalog provides default values

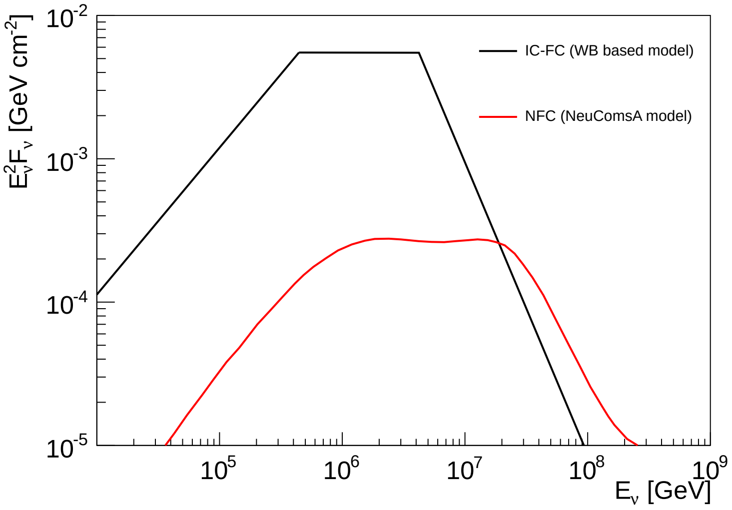

Figure 7.1: Muon neutrino fluence of GRB080603A from analytic calculation based on WB model (IC-FC, back curve) and NeuCosmA model (NFC, red curve). Detailed calculations in NeuCosmA yield changes in the magnitude and the shape of the neutrino fluence. Figure digitized from [14].

for the parameters that are missing or incomplete from the measurements and we used the same default values as inputs into NeuCosmA.

7.4.2 Simulation: AraSim

AraSim is a software package used within the ARA collaboration to simulate neutrino signals as they would be observed by the detector. It simulates the full chain of neutrino events such as the neutrino's path through the Earth, radio Cherenkov emission, the path and response of the emitted signal in the ice, and the trigger and data acquisition mechanisms of the detector. It uses custom parameterized radio Cherenkov emission model inspired by [12], which generates the signal with proper phase response. In AraSim, neutrino efficiencies as a function of source direction are properly accounted through modeling of two main effects, neutrino absorption by the Earth and the path through the ice of the emitted radio Cherenkov signal. With AraSim, we can study the radio Cherenkov emission with respect to the source direction. Fig. 7.2 show the distributions of the reconstructed RF signal source's direction from various neutrino travel directions from Vpol channels and Hpol channels. For each neutrino event, the reconstructed RF source direction with respect to the neutrino source direction is calculated and plotted on the map (Fig. 7.2). These distribution plots could be used to make a the stringent geometric cut for point sources such as GRBs. However, as the thorough study of the relationship between the reconstructed direction and the source direction has not been carried out, we did not utilized this technique in this GRB neutrino search.

7.5 Data Analysis

We first selected 57 GRBs from a total of $\sim$ 600 GRBs from Jan. 2011 to Dec. 2012. We used the IceCube GRB catalog, which is a database based on the Gamma-Ray Coordinate Network (GCN), to find GRBs during the time period of interest.

From $\sim$ 600 GRBs from Jan. 2011 to Dec. 2012 in the catalog, we rejected GRBs that failed good-timing cuts which leave us 257 GRBs. The good-timing cuts consist of three cuts which require a low background level and stable data-taking. The first cut is a simple time window cut which rejected GRBs that occurred during the summer season at the South Pole in order to avoid strong anthropogenic backgrounds. For each year, we rejected GRBs that occurred from October 22nd to February 16th.

We also require that the data is not contaminated by any strong continuous waveform (CW) source by rejecting any GRBs that occurred within an hour of any run where 10 % or more events are highly correlated with each other.

The last timing cut is a livetime cut which requires the detector to be running and stably storing data during the GRB period. The livetime represents the fraction

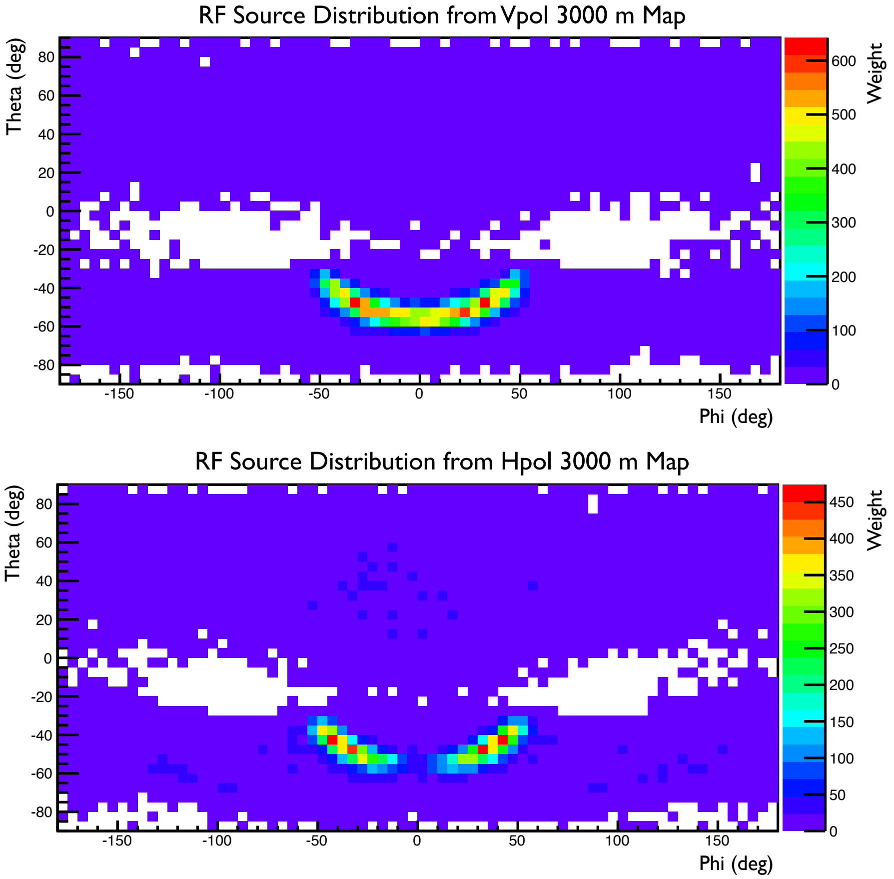

Figure 7.2: Distribution of the reconstruction location from the neutrino source direction from a simulated sample of 10^{18} eV neutrinos. The neutrino source direction is at $\theta = 0°$ and $\phi = 0°$. The plot is obtained from events with neutrino source directions pointing zenith angles from 37° to 102°. Two circular empty bins (white bins) in the plot are caused by the shadowing effect from the ray tracing in ice (Fig. 6.5).

of a second that trigger was available. If there was any instance when the livetime of the detector was lower than 10 % during the hour before or after a GRB, we reject that GRB from our analysis.

From the 257 GRBs that survived the good-timing cuts, we also applied an additional cut which requires that the GRB should be included in the Testbed detector's field of view. In order to define a range of sensitive field of view for the ARA Testbed,

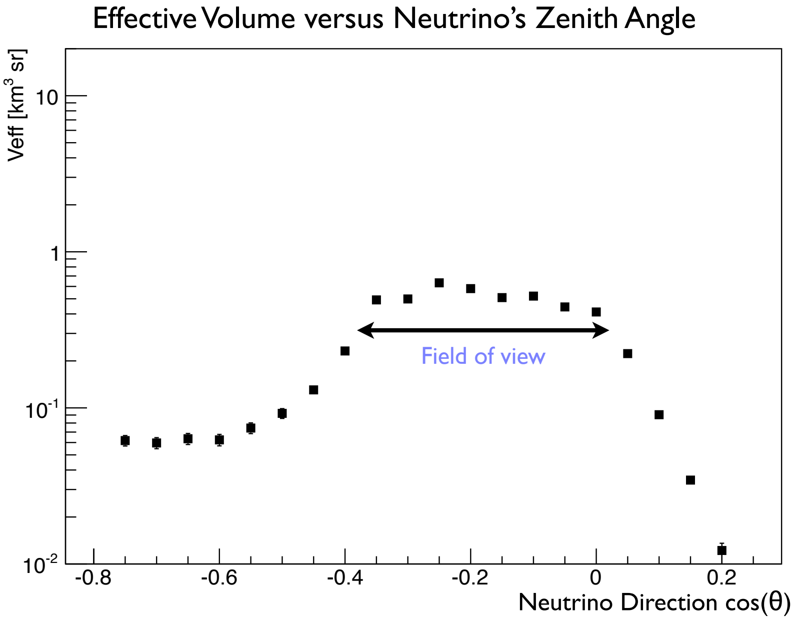

Figure 7.3: Effective volume as a function of neutrino travel direction plot. θ is the zenith angle of the neutrino travel direction. Field of view range is defined as the Full Width Half Maximum (FWHM) of the effective volume which is $-0.4 < \cos(\theta) < 0.05$.

we used simulation set with multiple incident angles of neutrinos at 10^{17} eV and obtained the effective volume as a function of neutrino direction.

In Fig. 7.3, the effective volume versus zenith angle of neutrino direction is shown. The zenith angle range of greatest sensitivity is defined as the Full Width Half Maximum (FWHM) of the effective area (arrow shown in Fig. 7.3). The decrease in effective volume on the right hand side and the left hand side of Fig. 7.3 come from different effects. The Earth absorption effect reduces the effective volume at high $\cos(\theta)$ (RHS of the plot) while the shadowing effect from the ray tracing in ice (Fig. 5.3) causes the cut-off at low $\cos(\theta)$ (LHS of the plot).

We applied this additional GRB geometric cut to select GRBs that are most likely to be detectable with the ARA Testbed. After applying this field-of-view cut,

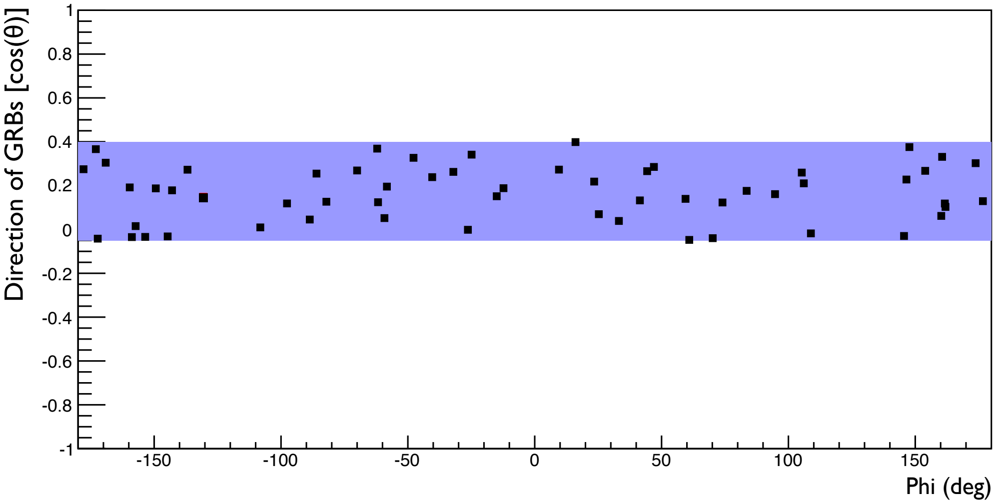

Figure 7.4: The distribution map of 57 selected GRBs in Testbed local coordinates. The blue band in the map is the field-of-view cut range defined in Fig. 7.3. Note that $\cos(\theta)$ in this map is the direction of the GRB while $\cos(\theta)$ in Fig. 7.3 is the direction of the neutrino.

57 GRBs are chosen. Fig. 7.4 shows the distribution map of 57 GRBs in Testbed local coordinates.

Fig 7.5 shows the fluences of all 57 selected GRBs with NeuCosmA software. Among 57 survived GRBs, one GRB was brighter than other GRBs. Its fluence was higher than the others by and order of magnitude above 10^{16} eV. We use this dominant GRB event as representative of the sum of the 57 GRBs and optimized our analysis cuts with a neutrino simulation set that used the fluence from dominant GRB.

For this search, we re-optimized the cuts that we used for the diffuse neutrino search [2]. A stringent timing cut surrounding the time of each GRB dramatically reduces the expected background events and thus we can loosen the analysis cuts and increase the sensitivity to GRB neutrinos. Among the set of analysis cuts described in [2], the Delay Difference cut, the Reconstruction Quality cuts, and the

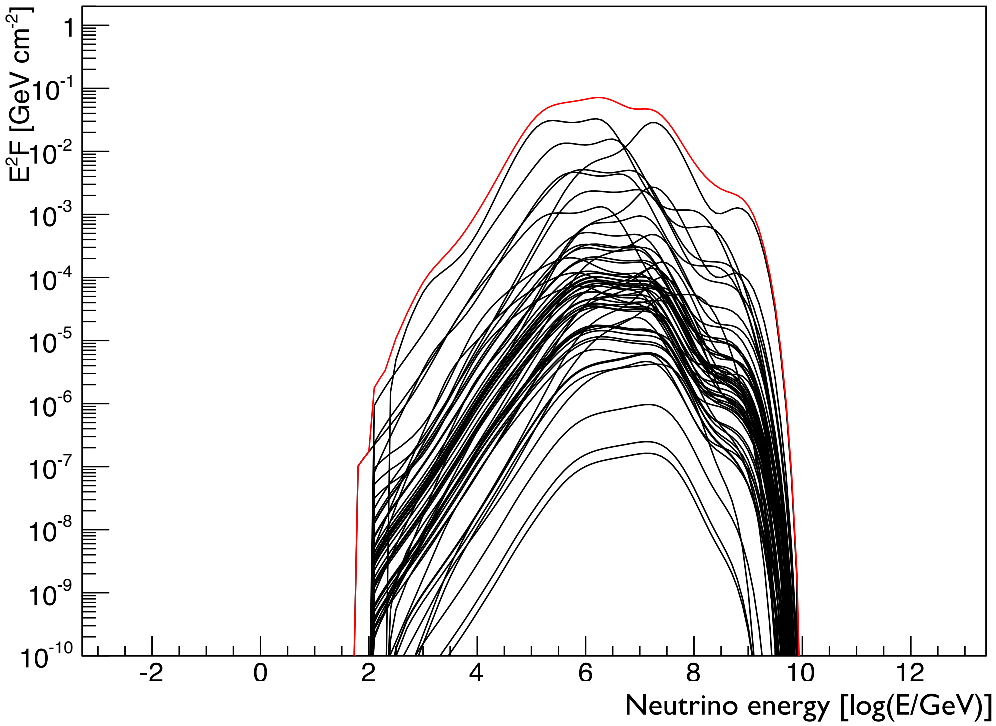

Figure 7.5: The fluences of 57 selected GRBs (black curves) and the fluence from the summation of all 57 GRBs (red curve). One GRB is brighter than other GRBs by an order of magnitude above 10^{16} eV. This dominant GRB is chosen as representative of the sum of the 57 GRBs.

Peak/Correlation cut are re-optimized for this search. Three re-optimized cuts are all based on the quality of the directional reconstruction while the rest of the cuts are designed to reject specific type of backgrounds such as CW and calibration pulser events. A total of four cut parameters from three cuts are changed in 4D space and we obtained a set of cut parameters which give us the best limit on the dominant GRB event from the NeuCosmA model. All three cuts become looser than the diffuse neutrino search [2] and the overall analysis cut efficiency for the dominant GRB fluence increased by factor of ∼2.4.

The expected number of neutrino and background events are obtained from re-optimized cuts. The number of expected neutrino events is calculated for each GRB. For each GRB, the analysis level effective area as a function of energy is obtained from corresponding geometric information of the GRB. The total expected number of neutrino events is:

$$N_{\text{total}} = \sum_{i=1}^{57} \left(\int d\log E \cdot EF^i(E) \cdot A^i_{\text{effect}}(E) \cdot \ln 10 \right) \tag{7.1}$$

where i is a index number of GRB (total 57 GRBs), $F^i(E)$ is the fluence [$\text{GeV}^{-1}\text{cm}^{-2}$] of i^{th} GRB, and $A^i_{\text{effect}}(E)$ is the effective area of the Testbed for the neutrinos from i^{th} GRB direction. The expected number of background events is obtained from an exponential function fit at the final Peak/Correlation cut, which is described in [2].

We use a blinding technique that draws from both the one used for the ARA diffuse neutrino search (Chapter 6) and the ANITA GRB neutrino analysis [105]. Our analysis consists of three stages. First, we use a 10 % subset from the full ARA Testbed data set for the preliminary background analysis. We consider a background analysis window to be the hour on either side of each GRB time, minus the closest 5 minutes. The 55 minutes on either side of a GRB (total 110 minutes) is a background analysis window and 5 minutes before and after the GRB is selected as a neutrino signal window. This is the same method used in ANITA GRB analysis [105].

With the events in the background analysis window, we optimize our analysis cuts to give us the best limit. From our optimized cuts, we expect to have 1.166 background events in the 57 GRB background windows and 0.106 background events in the neutrino signal windows from the remaining 90 % data set. Expected number of neutrino events from 57 GRBs is 1.47×10^{-5}.

After the first stage of analysis, we look at the events in the 90 % data set background analysis windows. In this stage of analysis, we make sure our background estimation from the 10 % subset is consistent with what we see in the remaining 90 % of the data. We have one survived event from 90 % data set's 57 GRB background analysis windows which is consistent with the 1.166 expected events.

In the final stage of the analysis, we search for neutrino events in the neutrino signal windows for each GRBs with the 90 % data set. With the same optimized analysis cuts defined in the first analysis stage, we search for events that pass our cuts within the 57 GRB signal windows over a total of 570 minutes.

7.6 Results

There were no events in the 90 % data set signal region which is consistent with 0.106 background events. With a 90% confidence interval from expected background and estimated GRB neutrino events, we placed a limit for the combined fluence from the 57 GRBs. Fig. 7.6 shows the fluence of each GRB, the total fluence from 57 GRBs with NeuCosmA model, and the GRB neutrino fluence limit from 10^{16} to 10^{19} eV.

In order to compare the limit from other experiments which have different set of GRBs for their analysis, we also provide the inferred quasi-diffuse neutrino flux limit with two assumptions. First, we assume that the 57 analyzed GRBs can represent the average GRB over the year. The second assumption is to let 667 GRBs as an average number of GRBs that are detected by satellites in a year [54, 110]. With these two assumptions, the quasi-diffuse neutrino flux limit is:

$$E^2\Phi = E^2F \times \frac{1}{4\pi}\frac{667}{N_{\mathrm{GRB}}}\frac{1}{365 \times 24 \times 60 \times 60} \tag{7.2}$$

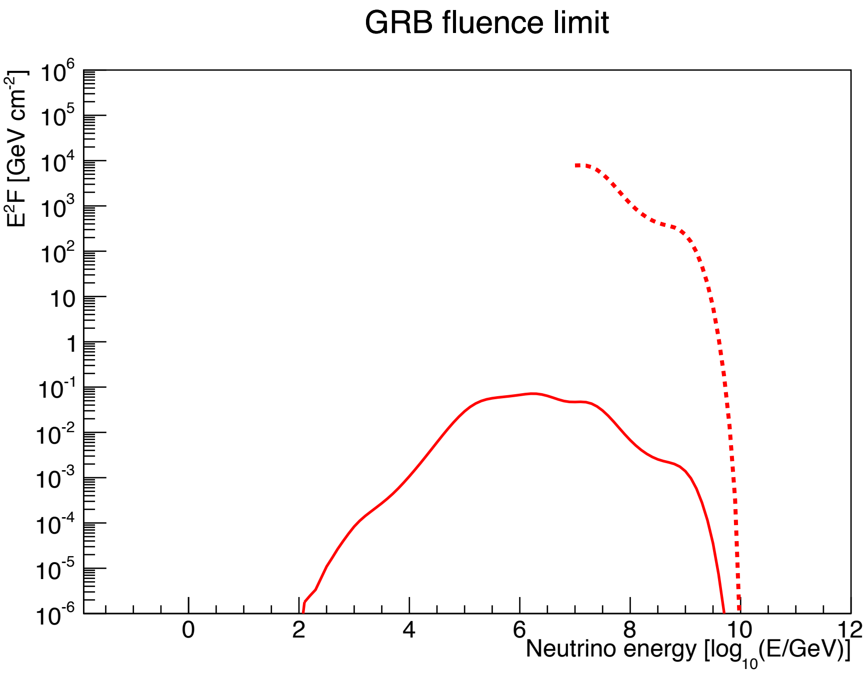

Figure 7.6: The limit on the UHE GRB neutrino fluence from 57 GRBs. Total fluence from 57 GRBs is shown with a red solid curve and the limit from the ARA Testbed above 10^{16} eV is shown with a red dashed curve.

where $E^2\Phi$ is the quasi-diffuse neutrino flux limit in units of $[\mathrm{GeVcm^{-2}sr^{-1}sec^{-1}}]$, E^2F is the fluence limit, and N_{GRB} is the number of analyzed GRBs which is 57 for this analysis. Fig. 7.7 shows the quasi-diffuse neutrino flux limit from multiple experiments. Our limit is the first UHE GRB neutrino quasi-diffuse flux limit at energies above 10^{16} eV.

From the future analyses from two ARA deep stations, we expect to have at least a factor of 6 improved sensitivity based on [2]. There is a factor of ∼3 increment from the shallow Testbed station to the 200 m deep station and another factor of ∼2 for the number of deep stations currently operating. In addition to the improvements from the number of deep stations, we expect to have improved livetime, and analysis efficiencies from the deep stations.

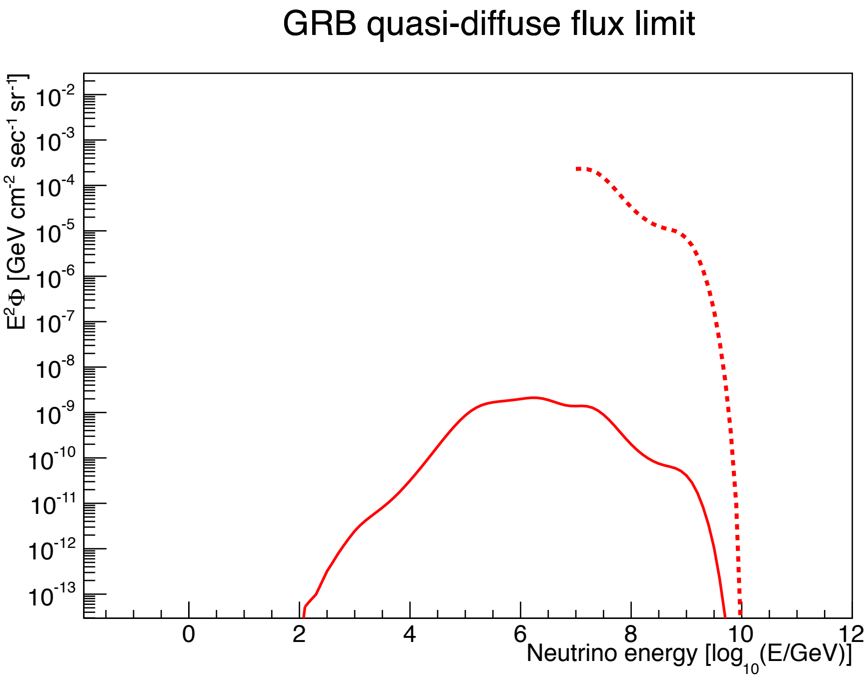

Figure 7.7: The inferred quasi-diffuse flux limit from the selected 57 GRBs. The quasi-diffuse flux limit is obtained from the fluence limit (Fig. 7.6 with the assumptions that 57 analyzed GRBs can represent the average GRB over the year and average number of GRBs in a year is 667. This is the first quasi-diffuse GRB neutrino flux limit for energies above 10^{16} eV.

7.7 Conclusions

Using ARA Testbed data from January 2011 to December 2012, we have searched UHE GRB neutrinos. Analysis cuts have been re-optimized with reduced background from the coincidence time window for the 57 selected GRBs. The GRB neutrino spectra are based on the NeuCosmA code, an advanced Monte Carlo cosmic neutrino accelerator code. We found zero neutrino candidate events from the analysis which is consistent with the expectation. We present the GRB neutrino fluence limit and the first quasi-diffuse GRB neutrino flux limit for energies above 10^{16} eV. Future analyses from ARA deep stations are expected to have at least a factor of 6 improvement. This

ARA Testbed analysis will serve as a guideline and benchmark for the future ARA deep stations' analyses.

Chapter 8

Conclusions

In this thesis, we described two different searches for UHE neutrinos using ARA Testbed data from 2011 to 2012. With the Testbed data and the simulation set produced by the simulation that we developed, we present diffuse (GZK) and point source (GRB) neutrino searches.

In Chapter 6 we present a diffuse UHE neutrino search from the Testbed. We use an interferometric map technique for our analyses. From interferometric maps, we apply geometric cuts that reject events that reconstruct to known background sources and clustering directions. We also reject events that have a low quality reconstruction based on the interferometric maps. The overall analysis efficiency for a 10^{18} eV neutrino was ~20%. We found zero neutrino candidate events on an expected $0.06\ ^{+0.52}_{-0.05}$ background events. We set limits on the neutrino flux above 10^{17} eV given the effective area of the Testbed derived from AraSim and 224 days of livetime examined from the data.

A GRB neutrino search from the Testbed is presented in Chapter 7. Among ~600 GRBs monitored by the GCN catalog from January 2011 to December 2012, 57 GRBs were selected to be analyzed by a set of cuts that rejects high anthropogenic background periods, unstable station periods, and GRBs located outside of our field-of-view. We only analyze events that occurred during the hour on either side of the time of each GRB. This timing constraint reduced the estimated number of background events and we re-optimized the analysis cuts to get the best limit on the dominant GRB event using the NeuCosmA modeling program. Three analysis cuts that are related to the quality of the directional reconstruction become looser than in the diffuse neutrino search and the overall analysis cut efficiency for the fluence of the dominant GRB increased by a factor of ∼2.4. There were no neutrino candidate events passing all cuts on 0.106 estimated background events. We set a limit on the GRB neutrino fluence and the first quasi-diffuse GRB neutrino flux limit for energies above 10^{16} eV.

Although neutrino flux and fluence constraints set by our Testbed analyses are not the best limits in the UHE regime due to the shallowly deployed antennas, analysis techniques from our analyses can provide a benchmark for future deep stations' neutrino searches which are expected to be improved. For the neutrino search in the two operational deep ARA stations, we expect to have at least a factor of 6 improved sensitivity to UHE neutrinos. This includes a factor of three for due to increased depth, and another factor of two for two operational stations instead of one.

Aside from the effect of deep station, we also expect to have improvements in analysis efficiencies due to the increased number of antennas. For each station, the number of antennas that are buried in the ice increases from 8 to 16 by using deep stations instead of the Testbed. With more antennas, we can require more trigger coincidences between antennas which reduces the noise rates and allows us to reduce the trigger threshold. Lower trigger threshold increases the sensitivity of the detector to neutrinos. Also, the quality of the directional reconstruction will be dramatically improved as the total number of pairs of antennas making an interferometric map increase from 6 to 28. This increased number of pairs of antennas will help us to identify the direction of the source more reliably and distinguish between anthropogenic background events and neutrino candidate events.

Preliminary research from two deep stations shows consistent result with our expectations that described above. The neutrino sensitivity from two deep stations is improved by factor of ∼20 from our Testbed analysis. This improvement includes a factor of 6 from two deep stations as described above and another factor of 3 from the analysis efficiency. This preliminary research is currently under preparation to be published in near future.

Seven more deep stations are proposed to be deployed in two deployment seasons (Fig. 4.1) and we are looking forward to deploying a full detector with 37 stations. The proposed ARA37 is expected to detect UHE neutrinos robustly [31] and help us to understand UHE astrophysical phenomena.

Bibliography

[1] E. Hong *et. al.*, *Improved Performance of the Preamplifier-Shaper Design for a High-Density Sensor Readout System*, *Journal of the Korean Physical Society* **54** (2009) 760. Cited on page vi.

[2] **ARA Collaboration** Collaboration, P. Allison *et. al.*, *First Constraints on the Ultra-High Energy Neutrino Flux from a Prototype Station of the Askaryan Radio Array*, `1404.5285`. Cited on pages vi, 39, 47, 90, 140, 141, 146, 147, 148, and 150.

[3] M. Ahlers, L. Anchordoqui, M. Gonzalez-Garcia, F. Halzen and S. Sarkar, *GZK Neutrinos after the Fermi-LAT Diffuse Photon Flux Measurement*, *Astropart.Phys.* **34** (2010) 106–115 [`1005.2620`]. Cited on pages xi, xiv, 11, 15, 17, 18, and 19.

[4] M. Takeda, N. Sakaki, K. Honda, M. Chikawa, M. Fukushima *et. al.*, *Energy determination in the Akeno Giant Air Shower Array experiment*, *Astropart.Phys.* **19** (2003) 447–462 [`astro-ph/0209422`]. Cited on pages xiii and 2.

[5] **Particle Data Group** Collaboration, K. Nakamura *et. al.*, *Review of particle physics*, *J.Phys.* **G37** (2010) 075021. Cited on pages xiii, 1, 2, 3, 10, 11, 12, 14, 15, 24, and 27.

[6] C. Grupen, *Astroparticle Physics*. Springer, 2005. Cited on pages xiv and 29.

[7] P. W. Gorham, C. Hebert, K. Liewer, C. Naudet, D. Saltzberg *et. al.*, *Experimental limit on the cosmic diffuse ultrahigh-energy neutrino flux*, *Phys.Rev.Lett.* **93** (2004) 041101 [`astro-ph/0310232`]. Cited on pages xv, 31, and 32.

[8] **ANITA Collaboration** Collaboration, S. Barwick *et. al.*, *Constraints on cosmic neutrino fluxes from the anita experiment*, *Phys.Rev.Lett.* **96** (2006) 171101 [`astro-ph/0512265`]. Cited on pages xv, 6, 17, 32, and 35.

[9] **ANITA Collaboration** Collaboration, P. Gorham *et. al.*, *Erratum: Observational Constraints on the Ultra-high Energy Cosmic Neutrino Flux from the Second Flight of the ANITA Experiment*, *Phys.Rev.* **D85** (2012) 049901 [1011.5004]. Cited on pages xv, 34, 36, 91, 113, and 140.

[10] F. Halzen and S. R. Klein, *IceCube: An Instrument for Neutrino Astronomy*, *Rev.Sci.Instrum.* **81** (2010) 081101 [1007.1247]. Cited on pages xv and 37.

[11] **IceCube Collaboration** Collaboration, M. Aartsen *et. al.*, *Probing the origin of cosmic-rays with extremely high energy neutrinos using the IceCube Observatory*, *Phys.Rev.* **D88** (2013) 112008 [1310.5477]. Cited on pages xv, 34, 38, and 91.

[12] J. Alvarez-Muniz, A. Romero-Wolf and E. Zas, *Practical and accurate calculations of Askaryan radiation*, *Phys.Rev.* **D84** (2011) 103003 [1106.6283]. Cited on pages xix, 62, 63, 64, 65, and 142.

[13] J. Alvarez-Muniz, A. Romero-Wolf and E. Zas, *Cherenkov radio pulses from electromagnetic showers in the time-domain*, *Phys.Rev.* **D81** (2010) 123009 [1002.3873]. Cited on pages xix, xx, 71, and 72.

[14] S. Hummer, P. Baerwald and W. Winter, *Neutrino Emission from Gamma-Ray Burst Fireballs, Revised*, *Phys.Rev.Lett.* **108** (2012) 231101 [1112.1076]. Cited on pages xxxi, 141, and 142.

[15] R. Gandhi, C. Quigg, M. H. Reno and I. Sarcevic, *Ultrahigh-energy neutrino interactions*, *Astropart.Phys.* **5** (1996) 81–110 [hep-ph/9512364]. Cited on pages 1 and 6.

[16] **HiRes Collaboration** Collaboration, D. Bird *et. al.*, *The Cosmic ray energy spectrum observed by the Fly's Eye*, *Astrophys.J.* **424** (1994) 491–502. Cited on pages 2 and 4.

[17] **HiRes Collaboration** Collaboration, R. Abbasi *et. al.*, *First observation of the Greisen-Zatsepin-Kuzmin suppression*, *Phys.Rev.Lett.* **100** (2008) 101101 [astro-ph/0703099]. Cited on pages 2 and 4.

[18] **Pierre Auger Collaboration** Collaboration, J. Abraham *et. al.*, *Observation of the suppression of the flux of cosmic rays above* $4 \times 10^{19} eV$, *Phys.Rev.Lett.* **101** (2008) 061101 [0806.4302]. Cited on pages 2, 4, 15, and 17.

[19] P. Chen and K. Hoffman, *Origin and evolution of cosmic accelerators - the unique discovery potential of an UHE neutrino telescope: Astronomy Decadal Survey (2010-2020) Science White Paper*, 0902.3288. Cited on page 4.

[20] A. Olinto, J. Adams, C. Dermer, J. Krizmanic, J. Mitchell *et. al.*, *White Paper on Ultra-High Energy Cosmic Rays*, 0903.0205. Cited on page 4.

[21] K. Greisen, *End to the cosmic ray spectrum?*, *Phys.Rev.Lett.* **16** (1966) 748–750. Cited on pages 4 and 91.

[22] G. Zatsepin and V. Kuzmin, *Upper limit of the spectrum of cosmic rays*, *JETP Lett.* **4** (1966) 78–80. Cited on pages 4 and 91.

[23] V. Berezinsky and G. Zatsepin, *Cosmic rays at ultrahigh-energies (neutrino?)*, *Phys.Lett.* **B28** (1969) 423–424. Cited on page 4.

[24] V. Berezinsky, M. Kachelriess and A. Vilenkin, *Ultrahigh-energy cosmic rays without GZK cutoff*, *Phys.Rev.Lett.* **79** (1997) 4302–4305 [`astro-ph/9708217`]. Cited on page 4.

[25] D. Guetta, D. Hooper, J. Alvarez-Muniz, F. Halzen and E. Reuveni, *Neutrinos from individual gamma-ray bursts in the BATSE catalog*, *Astropart.Phys.* **20** (2004) 429–455 [`astro-ph/0302524`]. Cited on pages 4 and 20.

[26] E. Waxman and J. N. Bahcall, *High-energy neutrinos from cosmological gamma-ray burst fireballs*, *Phys.Rev.Lett.* **78** (1997) 2292–2295 [`astro-ph/9701231`]. Cited on pages 4 and 22.

[27] **Super-Kamiokande Collaboration** Collaboration, Y. Fukuda *et. al.*, *Evidence for oscillation of atmospheric neutrinos*, *Phys.Rev.Lett.* **81** (1998) 1562–1567 [`hep-ex/9807003`]. Cited on page 6.

[28] **ANTARES Collaboration** Collaboration, A. Margiotta, *The ANTARES neutrino telescope*, *EPJ Web Conf.* **52** (2013) 09008. Cited on page 6.

[29] **IceCube Collaboration** Collaboration, J. Ahrens *et. al.*, *Icecube - the next generation neutrino telescope at the south pole*, *Nucl.Phys.Proc.Suppl.* **118** (2003) 388–395 [`astro-ph/0209556`]. Cited on pages 6 and 34.

[30] S. Barwick, E. Berg, D. Besson, E. Cheim, T. Duffin *et. al.*, *Design and Performance of the ARIANNA Hexagonal Radio Array Systems*, `1410.7369`. Cited on page 6.

[31] P. Allison, J. Auffenberg, R. Bard, J. Beatty, D. Besson *et. al.*, *Design and Initial Performance of the Askaryan Radio Array Prototype EeV Neutrino Detector at the South Pole*, *Astropart.Phys.* **35** (2012) 457–477 [`1105.2854`]. Cited on pages 6, 39, 41, 54, 91, 132, 133, 141, and 155.

[32] S. Barwick, E. Berg, D. Besson, T. Duffin, J. Hanson *et. al.*, *Radio-frequency Attenuation Length, Basal-Reflectivity, Depth, and Polarization Measurements from Moore's Bay in the Ross Ice-Shelf*, `1410.7134`. Cited on pages 6 and 29.

[33] M. Ackermann *et. al.*, *Optical properties of deep glacial ice at the South Pole*, *Journal of Geophysical Research* **111** (2006) D13203. Cited on pages 6, 28, and 29.

[34] B. C. Lacki, *The End of the Rainbow: What Can We Say About the Extragalactic Sub-Megahertz Radio Sky?*, *Mon.Not.Roy.Astron.Soc.* **406** (2010) 863 [`1004.2049`]. Cited on page 11.

[35] M. Kachelriess, E. Parizot and D. Semikoz, *The GZK horizon and constraints on the cosmic ray source spectrum from observations in the GZK regime*, *JETP Lett.* **88** (2009) 553–557 [`0711.3635`]. Cited on page 12.

[36] R. Engel, D. Seckel and T. Stanev, *Neutrinos from propagation of ultrahigh-energy protons*, *Phys.Rev.* **D64** (2001) 093010 [`astro-ph/0101216`]. Cited on page 13.

[37] V. Barger, P. Huber and D. Marfatia, *Ultra high energy neutrino-nucleon cross section from cosmic ray experiments and neutrino telescopes*, *Phys.Lett.* **B642** (2006) 333–341 [`hep-ph/0606311`]. Cited on page 13.

[38] Z. Fodor, S. Katz, A. Ringwald and H. Tu, *Bounds on the cosmogenic neutrino flux*, *JCAP* **0311** (2003) 015 [`hep-ph/0309171`]. Cited on page 13.

[39] http://www.desy.de/∼uhecr/propagation.html. Cited on page 14.

[40] Z. Fodor and S. Katz, *Ultrahigh-energy cosmic rays from compact sources*, *Phys.Rev.* **D63** (2001) 023002 [`hep-ph/0007158`]. Cited on page 14.

[41] Z. Fodor, S. Katz, A. Ringwald and H. Tu, *Electroweak instantons as a solution to the ultrahigh-energy cosmic ray puzzle*, *Phys.Lett.* **B561** (2003) 191–201 [`hep-ph/0303080`]. Cited on page 14.

[42] http://www.physics.ohio-state.edu/∼connolly/CRnu/z/z.html. Cited on page 15.

[43] **IceCube Collaboration** Collaboration, A. Achterberg *et. al.*, *Multi-year search for a diffuse flux of muon neutrinos with AMANDA-II*, *Phys.Rev.* **D76** (2007) 042008 [`0705.1315`]. Cited on page 17.

[44] **IceCube Collaboration** Collaboration, M. Ackermann *et. al.*, *Search for Ultra High-Energy Neutrinos with AMANDA-II*, *Astrophys.J.* **675** (2008) 1014–1024 [`0711.3022`]. Cited on page 17.

[45] **BAIKAL Collaboration** Collaboration, V. Aynutdinov *et. al.*, *Search for a diffuse flux of high-energy extraterrestrial neutrinos with the nt200 neutrino telescope*, *Astropart.Phys.* **25** (2006) 140–150 [`astro-ph/0508675`]. Cited on page 17.

[46] **HiRes Collaboration** Collaboration, K. Martens, *HiRes Estimates and Limits for Neutrino Fluxes at the Highest Energies*, `0707.4417`. Cited on page 17.

[47] F. Halzen and D. Hooper, *AMANDA Observations Constrain the Ultrahigh Energy Neutrino Flux*, *Phys.Rev.Lett.* **97** (2006) 099901 [`astro-ph/0605103`]. Cited on page 17.

[48] **IceCube Collaboration** Collaboration, A. Achterberg *et. al.*, *First Year Performance of The IceCube Neutrino Telescope*, *Astropart.Phys.* **26** (2006) 155–173 [`astro-ph/0604450`]. Cited on page 17.

[49] R. W. Klebesadel, I. B. Strong and R. A. Olson, *Observations of Gamma-Ray Bursts of Cosmic Origin*, *Astrophys.J.* **182** (1973) L85–L88. Cited on page 20.

[50] F. Halzen and D. Hooper, *High-energy neutrino astronomy: The Cosmic ray connection*, *Rept.Prog.Phys.* **65** (2002) 1025–1078 [`astro-ph/0204527`]. Cited on page 20.

[51] R. White, *Some requirements of a colliding comet source of gamma ray bursts*, *Astrophysics and Space Science* **208** (1993), no. 2 301–311. Cited on page 20.

[52] D. Lynden-Bell, *Galactic nuclei as collapsed old quasars*, *Nature* **223** (1969) 690. Cited on page 22.

[53] D. Kazanas, K. Fukumura, E. Behar, I. Contopoulos and C. Shrader, *Toward a Unified AGN Structure*, `1206.5022`. Cited on page 22.

[54] E. Waxman and J. N. Bahcall, *High-energy neutrinos from astrophysical sources: An Upper bound*, *Phys.Rev.* **D59** (1999) 023002 [`hep-ph/9807282`]. Cited on pages 22, 24, 140, and 149.

[55] S. Yoshida, H.-y. Dai, C. C. Jui and P. Sommers, *Extremely high-energy neutrinos and their detection*, *Astrophys.J.* **479** (1997) 547–559 [`astro-ph/9608186`]. Cited on pages 22 and 25.

[56] P. Bhattacharjee, C. T. Hill and D. N. Schramm, *Grand unified theories, topological defects and ultrahigh-energy cosmic rays*, *Phys.Rev.Lett.* **69** (1992) 567–570. Cited on pages 22 and 25.

[57] T. J. Weiler, *Relic neutrinos, Z bursts, and cosmic rays above* 10^{20} *eV*, `hep-ph/9910316`. Cited on pages 22 and 25.

[58] Z. Fodor, S. Katz and A. Ringwald, *Determination of absolute neutrino masses from Z bursts*, *Phys.Rev.Lett.* **88** (2002) 171101 [`hep-ph/0105064`]. Cited on pages 22 and 25.

[59] C. M. Urry and P. Padovani, *Unified schemes for radio-loud active galactic nuclei*, *Publ.Astron.Soc.Pac.* **107** (1995) 803 [astro-ph/9506063]. Cited on page 23.

[60] E. Waxman, *Cosmological origin for cosmic rays above* 10^{19} *eV*, *Astrophys.J.* **452** (1995) L1–L4 [astro-ph/9508037]. Cited on page 23.

[61] G. A. Askaryan *JETP* **14** (1962) 441. Cited on pages 26 and 91.

[62] G. A. Askaryan *JETP* **21** (1965) 658. Cited on pages 26 and 91.

[63] I. Kravchenko, C. Cooley, S. Hussain, D. Seckel, P. Wahrlich *et. al.*, *Rice limits on the diffuse ultrahigh energy neutrino flux*, *Phys.Rev.* **D73** (2006) 082002 [astro-ph/0601148]. Cited on page 30.

[64] P. Gorham, K. Liewer and C. Naudet, *Initial results from a search for lunar radio emission from interactions of* $>=10^{19}$ *eV neutrinos and cosmic rays*, astro-ph/9906504. Cited on page 31.

[65] **IceCube Collaboration** Collaboration, M. Aartsen *et. al.*, *Observation of High-Energy Astrophysical Neutrinos in Three Years of IceCube Data*, *Phys.Rev.Lett.* **113** (2014) 101101 [1405.5303]. Cited on page 34.

[66] I. Kravchenko *et. al.*, *Updated Neutrino Flux Limits from the RICE Experiment at the South Pole*, 1106.1164. Cited on page 39.

[67] G. S. Varner *et. al.*, *The large analog bandwidth recorder and digitizer with ordered readout (LABRADOR) ASIC*, *Nucl. Instrum. Meth.* **A583** (2007) 447–460 [physics/0509023]. Cited on page 45.

[68] A. Connolly, R. S. Thorne and D. Waters *Phys.Rev.* **D83** (2011) 113009 [1102.0691]. Cited on pages 49 and 133.

[69] D. Chirkin and W. Rhode, *Propagating leptons through matter with Muon Monte Carlo (MMC)*, 0407075. Cited on page 49.

[70] http://icecube.wisc.edu/∼mnewcomb/radio/. Cited on pages xvii, 50, and 51.

[71] I. Kravchenko, D. Besson and J. Meyers, *In situ index-of-refraction measurements of the South Polar firn with the RICE detector*, *Journal of Glaciology* **50** (2004) 522–532. Cited on pages 50 and 132.

[72] Original code from Chris Weaver. Cited on page 50.

[73] P. Price *et. al.*, *Temperature profile for glacial ice at the South Pole: Implications for life in a nearby subglacial lake*, *PNAS* **99** (2002) 7844–7847. Cited on pages 53 and 132.

[74] F. A. Matsuoda, T. and S. Mae, *Effect of temperature on dielectric properties of ice in the range 5-39 GHz*, *Journal of Applied Physics* **80** (1996) 5884. Cited on pages 53 and 132.

[75] F. Wu, *Using ANITA-I to Constrain Ultra High Energy Neutrino-Nucleon Cross Section*. PhD thesis, University of California, Irvine, 2009. Cited on pages 53 and 132.

[76] http://www.nec2.org/. Cited on page 55.

[77] http://dd6um.darc.de/QucsStudio/qucsstudio.html. Cited on page 59.

[78] *IEEE TRANSACTIONS ON EDUCATION* **39** (1996), no. 1. Cited on page 59.

[79] J. Alvarez-Muniz, A. Romero-Wolf and E. Zas, *Time-domain radio pulses from particle showers*, *Nucl.Instrum.Meth.* **A662** (2012) S32–S35. Cited on pages 62, 65, 66, and 69.

[80] J. Alvarez-Muniz, R. Vazquez and E. Zas, *Calculation methods for radio pulses from high-energy showers*, *Phys.Rev.* **D62** (2000) 063001 [`astro-ph/0003315`]. Cited on pages 62, 73, and 74.

[81] J. Alvarez-Muniz, J. Carvalho, Washington R. and E. Zas, *Monte Carlo simulations of radio pulses in atmospheric showers using ZHAireS*, *Astropart.Phys.* **35** (2012) 325–341 [`1107.1189`]. Cited on page 62.

[82] E. Zas, F. Halzen and T. Stanev, *Electromagnetic pulses from high-energy showers: Implications for neutrino detection*, *Phys.Rev.* **D45** (1992) 362–376. Cited on pages 65 and 74.

[83] K. Greisen *Prog. Cosmic Ray Phys.* **3** (1956). Cited on page 66.

[84] H. A. Gaisser, T.K. *Proceedings of the 15th International Cosmic Ray Conference, 13-26 Aug 1977* **8** 353. Cited on pages 66 and 67.

[85] p. c. Jaime Alvarez-Muniz. Cited on page 66.

[86] L. Landau and I. Pomeranchuk, *Electron cascade process at very high-energies*, *Dokl.Akad.Nauk Ser.Fiz.* **92** (1953) 735–738. Cited on page 70.

[87] A. B. Migdal, *Bremsstrahlung and pair production in condensed media at high-energies*, *Phys.Rev.* **103** (1956) 1811–1820. Cited on page 70.

[88] J. Alvarez-Muniz and E. Zas, *Cherenkov radio pulses from Eev neutrino interactions: The LPM effect*, *Phys.Lett.* **B411** (1997) 218–224 [`astro-ph/9706064`]. Cited on pages 72, 74, and 75.

[89] J. Alvarez-Muniz and E. Zas, *The LPM effect for EeV hadronic showers in ice: Implications for radio detection of neutrinos*, *Phys.Lett.* **B434** (1998) 396–406 [astro-ph/9806098]. Cited on page 75.

[90] I. R. I.S. Gradshteyn, *Table of Integrals, Series and Products, 5th edition.* Academic Press, 1994. Cited on page 89.

[91] V. S. Berezinsky and G. T. Zatsepin, *Cosmic rays at ultra high energies (neutrino?)*, *Phys. Lett.* **B28** (1969) 423–424. Cited on page 91.

[92] V. S. Berezinsky and G. T. Zatsepin, , *Sov. J. Nucl. Phys.* **11** (1970) 111. Cited on page 91.

[93] P. Gorham *et. al.*, *Radio-frequency measurements of coherent transition and Cherenkov radiation: Implications for high-energy neutrino detection*, *Phys. Rev.* **E62** (2000) 8590–8605 [hep-ex/0004007]. Cited on page 91.

[94] D. Saltzberg *et. al.*, *Observation of the Askaryan effect*, *AIP Conf. Proc.* **579** (2001) 225–233. Cited on page 91.

[95] P. W. Gorham *et. al.*, *Accelerator measurements of the Askaryan effect in rock salt: A roadmap toward Teraton underground neutrino detectors*, *Phys. Rev.* **D72** (2005) 023002 [astro-ph/0412128]. Cited on page 91.

[96] **ANITA** Collaboration, P. W. Gorham *et. al.*, *Observations of the Askaryan effect in ice*, *Phys. Rev. Lett.* **99** (2007) 171101 [hep-ex/0611008]. Cited on page 91.

[97] **IceCube** Collaboration, M. Aartsen *et. al.*, *Evidence for High-Energy Extraterrestrial Neutrinos at the IceCube Detector*, *Science* **342** (2013), no. 6161 1242856 [1311.5238]. Cited on page 91.

[98] S. Barwick, D. Besson, P. Gorham and D. Saltzberg, *South Polar in situ radio-frequency ice attenuation*, *J. Glaciol.* **51** (2005) 231–238. Cited on page 91.

[99] K. Kotera, D. Allard and A. Olinto *JCAP* **1010** (2010) 013 [1009.1382]. Cited on page 114.

[100] P. Meszaros and P. Meszaros, *Gamma-ray bursts: Accumulating afterglow implications, progenitor clues, and prospects*, *Science* **291** (2001) 79–84 [astro-ph/0102255]. Cited on page 138.

[101] P. Meszaros, *Theories of gamma-ray bursts*, *Ann.Rev.Astron.Astrophys.* **40** (2002) 137–169 [astro-ph/0111170]. Cited on page 138.

[102] P. Meszaros, *Gamma-Ray Bursts*, *Rept.Prog.Phys.* **69** (2006) 2259–2322 [astro-ph/0605208]. Cited on page 139.

[103] **IceCube Collaboration** Collaboration, R. Abbasi *et. al.*, *An absence of neutrinos associated with cosmic-ray acceleration in γ-ray bursts*, *Nature* **484** (2012) 351–353 [1204.4219]. Cited on page 139.

[104] **ANTARES Collaboration** Collaboration, S. Adrian-Martinez *et. al.*, *Search for Cosmic Neutrino Point Sources with Four Year Data of the ANTARES Telescope*, *Astrophys.J.* **760** (2012) 53 [1207.3105]. Cited on page 139.

[105] A. Vieregg, K. Palladino, P. Allison, B. Baughman, J. Beatty *et. al.*, *The First Limits on the Ultra-high Energy Neutrino Fluence from Gamma-ray Bursts*, *Astrophys.J.* **736** (2011) 50 [1102.3206]. Cited on pages 139 and 148.

[106] S. Hummer, M. Ruger, F. Spanier and W. Winter, *Simplified models for photohadronic interactions in cosmic accelerators*, *Astrophys.J.* **721** (2010) 630–652 [1002.1310]. Cited on pages 139 and 140.

[107] http://grbweb.icecube.wisc.edu. Cited on page 139.

[108] **IceCube Collaboration** Collaboration, R. Abbasi *et. al.*, *Search for muon neutrinos from Gamma-Ray Bursts with the IceCube neutrino telescope*, *Astrophys.J.* **710** (2010) 346–359 [0907.2227]. Cited on page 139.

[109] **ANTARES Collaboration** Collaboration, S. Adrian-Martinez *et. al.*, *Search for muon neutrinos from gamma-ray bursts with the ANTARES neutrino telescope using 2008 to 2011 data*, *Astron.Astrophys.* **559** (2013) A9 [1307.0304]. Cited on page 139.

[110] **IceCube Collaboration** Collaboration, R. Abbasi *et. al.*, *Limits on Neutrino Emission from Gamma-Ray Bursts with the 40 String IceCube Detector*, *Phys.Rev.Lett.* **106** (2011) 141101 [1101.1448]. Cited on page 149.